

MASTER'S THESIS

Three-dimensional finite element analysis of additional losses in large power transformer windings

Thomas Weiglhofer, BSc

Institute for Fundamentals and Theory in Electrical Engineering

Graz University of Technology

Head of Institute: Univ.-Prof. Dipl.-Ing. Dr.techn. Oszkár Bíró



In cooperation with

Siemens AG Austria, Transformers Weiz

The SIEMENS logo in a bold, blue, sans-serif font.

Supervisor: Univ.-Prof. Dipl.-Ing. Dr.techn. Oszkár Bíró

Weiz, October 2017

EIDESSTATTLICHE ERKLÄRUNG

Ich erkläre an Eides statt, dass ich die vorliegende Arbeit selbstständig verfasst, andere als die angegebenen Quellen/Hilfsmittel nicht benutzt, und die den benutzten Quellen wörtlich und inhaltlich entnommenen Stellen als solche kenntlich gemacht habe.

Datum

Unterschrift

Danksagungen

An dieser Stelle möchte ich mich bei all jenen bedanken, welche mich im Rahmen meiner Diplomarbeit unterstützt, sowie zum Gelingen dieser beigetragen haben. Ganz besonderer Dank geht dabei an Herrn Univ. Prof. Dipl.-Ing Dr. Oszkár Bíró (Institut für Grundlagen und Theorie der Elektrotechnik) für die ausgezeichnete Betreuung während meiner gesamten Diplomarbeit. Des Weiteren möchte ich mich recht herzlich bei Herrn Dipl. Ing. Bernhard Wagner (Siemens Transformers Weiz) für die firmeninterne Betreuung und die anregenden Diskussionen, welche zu einer stetigen Verbesserung meiner Arbeit geführt haben, bedanken.

Neben den fachlichen Danksagungen möchte ich mich auch ganz herzlich bei meinen Eltern bedanken, welche mir mein Studium erst ermöglicht, sowie durch ihre ständige Unterstützung maßgeblich zu dessen Erfolg beigetragen haben.

Zusammenfassung

Eine möglichst genaue Berechnung der auftretenden Verluste spielt im Designprozess von Großtransformatoren eine wesentliche Rolle. Untersuchungen, in welcher Höhe radiale und axiale Zusatzverluste in Transformatorwicklungen auftreten beschränken sich derzeit auf die Ermittlung mit Hilfe eines 2D FEM-Modells, welches einige Vereinfachungen gegenüber der Realität erfordert. Im Rahmen dieser Arbeit soll eine neue Methode evaluiert werden um Zusatzverluste in Wicklungen von Großtransformatoren mithilfe eines genaueren 3D FEM-Modells zu ermitteln. Dazu wird anschließend, an die mit der Finite Elemente Methode durchgeführte Feldberechnung, ein analytisches Modell ausgewertet. Um die Ergebnisse zu evaluieren, werden bereits gefertigte Transformatoren mit dem neuen Modell nachgebildet und die Ergebnisse analysiert. Zusätzlich wird die notwendige Genauigkeit der Implementation von Scheibenwicklungen in das 3D Modell sowie deren Auswirkungen auf Zusatzverluste in Wicklungen als auch auf Zusatzverlusten in nicht aktiven Eisenteilen ermittelt.

Abstract

A precise calculation of the losses which occur during the operation of a large power transformer plays an important role in the design process. Investigations on the extent to which radial and axial additional losses occur in transformer windings are currently limited by the use of a 2D FEM model which requires some simplifications against reality. In this thesis, a new method is to be evaluated to determine additional losses in windings of large power transformers using a more accurate 3D FEM model. For this purpose, an analytical model of local losses is evaluated for the field computation performed using the finite element method. In order to evaluate the results, transformers already manufactured are simulated with the new model and the results are analyzed. In addition, the necessary accuracy of the implementation of disk windings into the 3D FEM-model as well as its effects on additional losses in windings as well as on additional losses in non-active iron parts are determined.

Table of contents

1	Introduction	1
1.1	General design of large power transformers.....	1
1.2	Active part.....	2
1.2.1	Iron core.....	2
1.2.2	Clamping structure	3
1.2.3	Windings	3
1.2.4	Shielding of stray flux.....	4
1.3	Losses	4
1.4	Scope of work	6
2	Calculation methods and modelling.....	7
2.1	Calculation of eddy current and hysteresis-losses in non-active steel parts.....	7
2.1.1	Transformer model	7
2.1.1.1	Winding modelling.....	8
2.1.2	Mathematical model	8
2.2	Calculation of additional winding losses	11
2.2.1	2D transformer model	11
2.2.1.1	Modelling of windings.....	13
2.2.1.2	Mathematical model.....	15
2.2.2	3D transformer model.....	16
2.2.2.1	Modelling of windings.....	18
2.2.2.2	Mathematical model.....	18
3	Verification of the analytical 3D model.....	21
3.1	Technical data	21
3.2	Rotationally symmetric 3D model.....	21
3.2.1	Comparison of different winding modelling	24
3.2.2	Loss comparison	27
3.3	3D TrafoLoss-model	29
3.3.1	Loss comparison	40
3.3.2	Influence of mesh accuracy on additional losses	40
4	Additional losses of various core types.....	44
4.1	One-limb core transformer “T1”.....	44
4.1.1	Technical data	44
4.1.2	3D TrafoLoss-model	44
4.1.3	Loss comparison	44
4.1.4	Effects of eddy currents in non-active steel parts.....	45
4.1.5	Computation times	45
4.2	Two-limb core transformer “T2”	46

4.2.1	Technical data	46
4.2.2	3D TrafoLoss-model	47
4.2.3	Loss comparison	48
4.2.4	Effects of eddy currents in non-active steel parts.....	49
4.2.5	Computation times	50
4.3	Three-limb core transformer “T3”	51
4.3.1	Technical data	51
4.3.2	3D TrafoLoss-model	51
4.3.3	Loss comparison	53
4.3.4	Effects of eddy currents in non-active steel parts.....	54
4.3.5	Computation times	55
4.4	Four-limb core transformer “T4”	55
4.4.1	Technical data	55
4.4.2	3D TrafoLoss-model	55
4.4.3	Loss comparison	57
4.4.4	Effects of eddy currents in non-active steel parts.....	58
4.4.5	Computation times	58
4.5	Five-limb core transformer “T5”	59
4.5.1	Technical data	59
4.5.2	3D TrafoLoss-model	59
4.5.3	Loss comparison	60
4.5.4	Effects of eddy currents in non-active steel parts.....	62
4.5.5	Computation times	63
5	Influence of winding modelling on additional losses in non-active steel parts	64
5.1	One-limb core transformer “T1”.....	64
5.1.1	Field plots.....	65
5.1.2	Loss comparison	67
5.2	Two-limb core transformer “T2”	68
5.2.1	Field plots.....	69
5.2.2	Loss comparison	72
5.3	Three-limb core transformer “T3”	75
5.3.1	Field Plots	76
5.3.2	Loss comparison	79
5.3.2.1	Influence of radial distribution of cylindrical windings with more than one layer	80
5.4	Four-limb core transformer “T4”	82
5.4.1	Field Plots	83
5.4.2	Loss comparison	85
5.5	Five-limb core transformer “T5”	88

5.5.1	Field plots.....	89
5.5.2	Loss comparison	90
6	Results.....	93
6.1	Additional losses in windings	93
6.2	Additional losses in non-active steel parts	93

List of tables

Table 1: “T1”: Current densities of the different winding blocks.....	25
Table 2: “T1”: Loss comparison of different 2D and 3D models	28
Table 3: “T1”: Loss comparison of the 3D TrafoLoss-model	40
Table 4: “T1”: Influences of FE-distribution on the additional losses	44
Table 5: “T1”: Comparison of eddy current free model with the standard 3D TrafoLoss model	45
Table 6: “T1”: Computation time of different 3D TrafoLoss-models	46
Table 7: “T2”: Loss comparison of 2D models and 3D TrafoLoss-model.....	49
Table 8: “T2”: Comparison of eddy current free model with the standard 3D TrafoLoss model	50
Table 9: “T2”: Computation time of different 3D TrafoLoss-models	50
Table 10: “T3”: Loss comparison of 2D models and 3D TrafoLoss-model.....	53
Table 11: “T3”: Comparison of eddy current free model with the standard 3D TrafoLoss-model	54
Table 12: “T3”: Computation time of different 3D TrafoLoss-models	55
Table 13: “T4”: Loss comparison of 2D models and 3D TrafoLoss-model.....	57
Table 14: “T4”: Comparison of eddy current free model with the standard 3D TrafoLoss-model	58
Table 15: „T4“: Computation time of different 3D TrafoLoss-models	58
Table 16: “T5”: Loss comparison of the 2D models	61
Table 17: “T5”: Losses of the 3D TrafoLoss-model.....	62
Table 18: “T5”: Losses of the 3D TrafoLoss-model without eddy current region	63
Table 19: “T5”: Computation time of different 3D TrafoLoss-models	63
Table 20: “T1”, one axial winding block on HV-side, losses in non-active steel parts.....	67
Table 21: “T1”, several axial winding blocks on HV-side, losses in non-active steel parts.....	68
Table 22: “T2”: Current densities in winding segments.....	69
Table 23: “T2”, one axial winding block on HV-side, losses in non-active steel parts.....	73
Table 24: “T2”, several axial winding blocks on HV-side, losses in non-active steel parts.....	74
Table 25: “T3”: Current densities in winding segments.....	76
Table 26: “T3”, one axial winding block on HV-side, losses in non-active steel parts.....	79
Table 27: “T3”, several axial winding blocks on HV-side, losses in non-active steel parts.....	80
Table 28: “T3”, several axial winding blocks on HV-side and only one radial coil on LV-side, losses in non-active steel parts	81
Table 29: “T4”: Current densities in winding segments.....	82
Table 30: “T4”, one axial winding block on HV-side, losses in non-active steel parts.....	86
Table 31: “T4”, several axial winding blocks on HV-side, losses in non-active steel parts.....	87
Table 32: “T5”: Current densities in winding segments.....	88
Table 33: “T5”, one axial winding block on HV-side, losses in non-active steel parts.....	91
Table 34: “T5”, several axial winding blocks on HV-side, losses in non-active steel parts.....	92

List of figures

Fig. 1. Basic design of a three-phase power transformer [1]	1
Fig. 2. Layering of individual sheets [2].....	2
Fig. 3. Core types of a single limb transformer; a) two-limb core, b) one-limb core (with two back-closing limbs), c) four-limb core.....	3
Fig. 4. Core implementation of three-phase transformers; a) three-limb core, b) five-limb core	3
Fig. 5. FE-Model of a five-limb core transformer with tank, clamping structure, tank shielding and yoke shielding (without tie bars)	6
Fig. 6. FE Model of a three-limb core transformer	7
Fig. 7. Basic field model.....	8
Fig. 8. Explanation of the cross section on which the rotationally symmetric model is based using a single-phase transformer	12
Fig. 9. Geometry of the 2D model	13
Fig. 10. Coarse modelling of transformer windings	14
Fig. 11. Detailed modelling of winding conductors	14
Fig. 12. Loss calculation in the 2D model	15
Fig. 13. Top view of a transformer model for calculating eddy current losses in steel parts	17
Fig. 14. Top view (without tank) of a transformer model for calculating additional winding losses	17
Fig. 15. left: 3D FEM-model for evaluating additional winding losses; right: 3D FEM-model for computing additional losses in non-active steel parts.....	18
Fig. 16. Loss calculation in the 3D model [8].....	19
Fig. 17. "T1": left: existing 2D model, right: 3D model.....	22
Fig. 18. "T1": left: Field plot of 2D model, right: Field plot of the rotational symmetric 3D model	23
Fig. 19. "T1": Comparison of radial and axial fields between 2D model and 3D model in z-direction ($x=0, y= r_{midLV}$).....	23
Fig. 20. "T1": left: HV-disk winding modelled with one axial block, right: HV-winding modelled with six axial blocks	24
Fig. 21. "T1": Distribution of winding parts in the HV-winding.....	25
Fig. 22. "T1": Field plots of the rotational symmetric 3D models, left: one block on HV-side, right: several blocks on HV-side.....	26
Fig. 23. "T1": Comparison of radial and axial fields in LV-winding in z-direction ($x=0, y= r_{midLV}$).....	26
Fig. 24. "T1": Comparison of radial and axial fields in HV-winding in z-direction ($x=0, y= r_{midHV}$)	27
Fig. 25. "T1": 3D TrafoLoss model for calculating the additional winding losses.....	29
Fig. 26. "T1": Finite element mesh in x-z-plane (back view)	30
Fig. 27. "T1": Finite element mesh in x-y pane (top view).....	30
Fig. 28. Field comparison points.....	31
Fig. 29. "T1": Comparison of radial and axial fields in winding 1 in the rotational symmetric 3D model.....	32
Fig. 30. "T1": Comparison of radial and axial fields in winding 1 in the 3D TrafoLoss-model ..	33
Fig. 31. "T1": Comparison of radial and axial fields in winding 1, point 1 between the rotationally symmetric and the TrafoLoss-model	34
Fig. 32. "T1": Comparison of radial and axial fields in winding 1, point 2 between the rotationally symmetric and the TrafoLoss-model	34

Fig. 33. "T1": Comparison of radial and axial fields in winding 2, point 1 between the rotationally symmetric and the TrafoLoss-model	35
Fig. 34. "T1": Comparison of radial and axial fields in winding 2, point 2 between the rotational symmetric and the TrafoLoss-model	35
Fig. 35. Evaluation of the magnetic flux density in azimuthal direction	36
Fig. 36. "T1": B_{rad} as a function of φ evaluated in the centre of winding 1 at $z=1,384$ m (bottom edge of the upper winding block of winding 2)	37
Fig. 37. "T1": B_{rad} as a function of φ evaluated in the centre of winding 2 at $z=1,384$ m (bottom edge of the upper winding block of winding 2)	37
Fig. 38. "T1": B_{rad} as a function of φ and z evaluated in the centre of winding 1 in the rotationally symmetric 3D model	38
Fig. 39. "T1": B_{rad} as a function of φ and z evaluated in the centre of winding 1 in the 3D TrafoLoss-model.....	39
Fig. 40. "T1": Difference of B_{rad} from the rotationally symmetric model and B_{rad} from the TrafoLoss-model.....	39
Fig. 41. "T1": Finite element mesh in the coarse 2D model	41
Fig. 42. "T1": Finite element mesh in x-z-plane with finer axial FE-division	42
Fig. 43. "T1": Finite element mesh in x-y-plane with finer axial FE-division	42
Fig. 44. "T1": Finite element mesh in x-z-plane with finer radial and axial FE-division	43
Fig. 45. "T1": Finite element mesh in x-y-plane with finer radial and axial FE-division	43
Fig. 46. "T2": 3D TrafoLoss-model.....	47
Fig. 47. "T2": Finite element mesh in x-z-plane.....	48
Fig. 48. "T2": Finite element mesh in x-y-plane.....	48
Fig. 49. "T3": 3D TrafoLoss-model.....	51
Fig. 50. "T3": Finite element mesh in x-z-plane.....	52
Fig. 51. "T3": Finite element mesh in x-y-plane.....	52
Fig. 52. "T4": 3D TrafoLoss-model.....	56
Fig. 53. "T4": Finite element mesh in x-z-plane.....	56
Fig. 54. "T4": Finite element mesh in x-y-plane.....	57
Fig. 55. "T5": 3D TrafoLoss-model.....	59
Fig. 56. "T5": Finite element mesh in x-z-plane.....	60
Fig. 57. "T5": Finite element mesh in x-y-plane.....	60
Fig. 58. "T1": Geometry plots, left: one axial winding block on HV-side; right: several axial winding blocks on HV-side	64
Fig. 59. "T1": Max. surface flux density in tank, left: one axial winding block on HV-side; right: several axial winding blocks on HV-side.....	65
Fig. 60. "T1": Max. surface flux density in clamping structure, left: one axial winding block on HV-side; right: several axial winding blocks on HV-side	65
Fig. 61. "T1": Max. surface flux density in tank shielding, left: one axial winding block on HV-side; right: several axial winding blocks on HV-side	66
Fig. 62. "T1": Max. surface flux density in tie bars, left: one axial winding block on HV-side; right: several axial winding blocks on HV-side.....	66
Fig. 63. "T2": Geometry plots, left: one axial winding block on HV-side; right: several axial winding blocks on HV-side	69
Fig. 64. "T2": Max. surface flux density in tank, left: one axial winding block on HV-side; right: several axial winding blocks on HV-side.....	70

Fig. 65. "T2": Max. surface flux density in clamping structure, left: one axial winding block on HV-side; right: several axial winding blocks on HV-side	70
Fig. 66. "T2": Max. surface flux density in tank shielding, left: one axial winding block on HV-side; right: several axial winding blocks on HV-side	71
Fig. 67. "T2": Max. surface flux density in yoke shielding, left: one axial winding block on HV-side; right: several axial winding blocks on HV-side	71
Fig. 68. "T2": Max. surface flux density in tie bars, left: one axial winding block on HV-side; right: several axial winding blocks on HV-side	72
Fig. 69. "T3": Geometry plots, left: one axial winding block on HV-side; right: several axial winding blocks on HV-side	75
Fig. 70. "T3": Max. surface flux density in tank, left: one axial winding block on HV-side; right: several axial winding blocks on HV-side	76
Fig. 71. "T3": Max. surface flux density in clamping structure, left: one axial winding block on HV-side; right: several axial winding blocks on HV-side	77
Fig. 72. "T3": Max. surface flux density in tank shielding, left: one axial winding block on HV-side; right: several axial winding blocks on HV-side	77
Fig. 73. "T3": Max. surface flux density in yoke shielding, left: one axial winding block on HV-side; right: several axial winding blocks on HV-side	78
Fig. 74. "T3": Max. surface flux density in tie bars, left: one axial winding block on HV-side; right: several axial winding blocks on HV-side	78
Fig. 75. "T4": Geometry plots, left: one axial winding block on HV-side; right: several axial winding blocks on HV-side	82
Fig. 76. "T4": Max. surface flux density in tank, left: one axial winding block on HV-side; right: several axial winding blocks on HV-side	83
Fig. 77. "T4": Max. surface flux density in clamping structure, left: one axial winding block on HV-side; right: several axial winding blocks on HV-side	83
Fig. 78. "T4": Max. surface flux density in tank shielding, left: one axial winding block on HV-side; right: several axial winding blocks on HV-side	84
Fig. 79. "T4": Max. surface flux density in yoke shielding, left: one axial winding block on HV-side; right: several axial winding blocks on HV-side	84
Fig. 80. "T4": Max. surface flux density in tie bars, left: one axial winding block on HV-side; right: several axial winding blocks on HV-side	85
Fig. 81. "T5": Geometry plots, left: one axial winding block on HV-side; right: several axial winding blocks on HV-side	88
Fig. 82. "T5": Max. surface flux density in tank, left: one axial winding block on HV-side; right: several axial winding blocks on HV-side	89
Fig. 83. "T5": Max. surface flux density in clamping structure, left: one axial winding block on HV-side; right: several axial winding blocks on HV-side	89
Fig. 84. "T5": Max. surface flux density in tank shielding, left: one axial winding block on HV-side; right: several axial winding blocks on HV-side	90
Fig. 85. "T5": Max. surface flux density in yoke shielding, left: one axial winding block on HV-side; right: several axial winding blocks on HV-side	90

Glossary

Symbol	Name	Unit	SI-Unit
B	Magnetic flux density	T	Vs/m ²
E	Electric field strength		V/m
H	Magnetic field strength		A/m
I	Current		A
J	Current density		A/m ²
K	Surface current density		A/m ²
N_j	Edge based vector basis functions		-
N_j	Node based scalar basis functions		-
P	Power loss	W	VA
T	Current vector potential		
U	Voltage		V
b	Magnetic surface charge density		
n	Normal vector		1
Γ	Surface		m ²
Φ	Magnetic scalar potential		
Ω	Volume		m ³
μ	Permeability		Vs/Am
ρ	Electrical resistivity		Ωmm ² /m
ρ_d	Mass density of steel		kg/m ³
ω	Angular frequency		1/s

1 Introduction

Whether used to transfer power between different network levels or as generator step-up transformer, power transformers are strategically important resources for a safe network operation. Due to the high acquisition costs and the strategic importance, power transformers are developed and manufactured exactly according to their respective application. Because of their wide application range, different designs are possible.

1.1 General design of large power transformers

In principle, a power transformer consists of an active part (iron core and windings), a cooling device with a cooling medium (mineral oil, ester, etc.), a tank, bushings and of a no-load- or an on-load tap-changer with a desired control capacity [1]. The basic structure of a power transformer can be seen in Fig. 1. Additionally, tank shielding and yoke shielding may be used to safeguard against stray flux in passive iron parts.

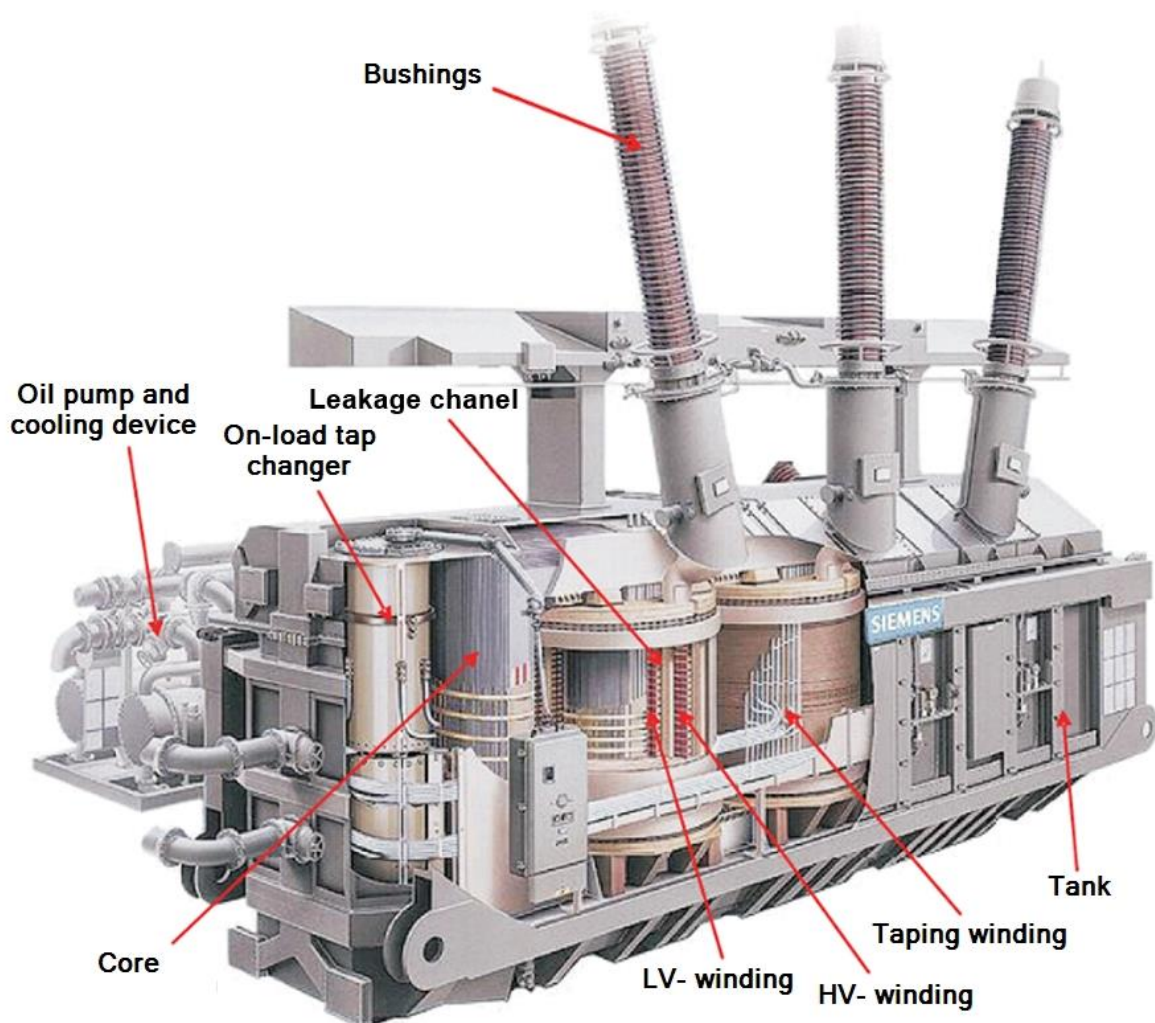


Fig. 1. Basic design of a three-phase power transformer [1]

1.2 Active part

The most important assembly of a large power transformer is the active part. In principle, it consists of an iron core, windings, a clamping structure and, optionally, of different shielding packages.

1.2.1 Iron core

The iron core serves to guide the magnetic field generated by the windings. In order to avoid eddy current losses, the core is layered predominantly of grain-oriented electrical steel sheets (0,23 mm to 0,35 mm). In order to approximate the desired circular shape of the core limbs, the sheets are combined into packages of different lengths. Due to the grain orientation, the sheets have to be cut obliquely in order to maintain the magnetic easy direction [2]. An example is shown in Fig. 2.

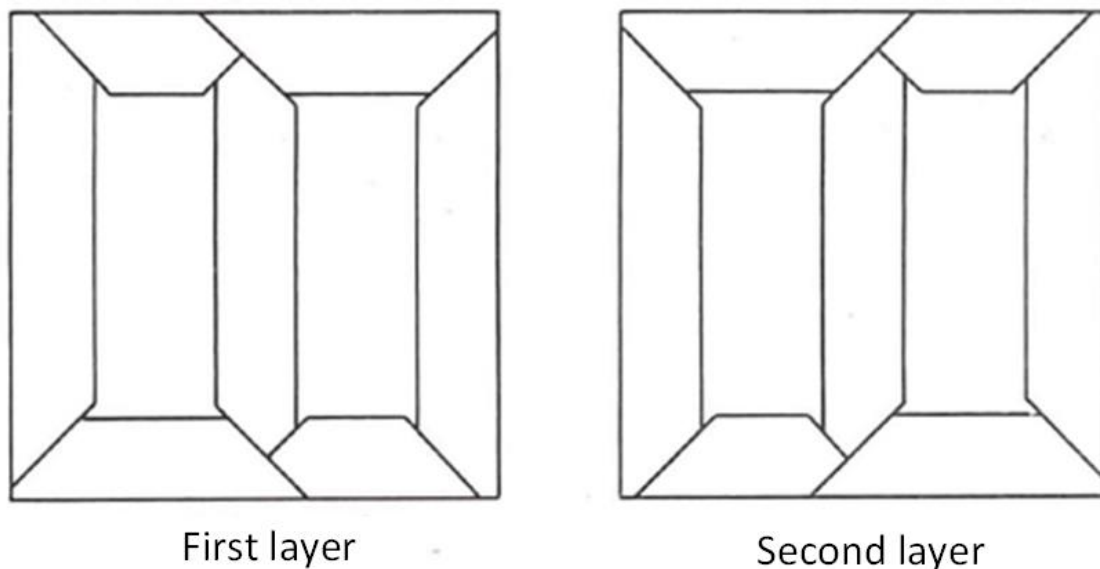


Fig. 2. Layering of individual sheets [2]

Due to the wide range of applications, different core types are used depending on the type of application. The core of a single-phase transformer will either be realized as a two-limb core (Fig. 3a), as a one-limb core (Fig. 3b) or as a four-limb core transformer (Fig. 3c).

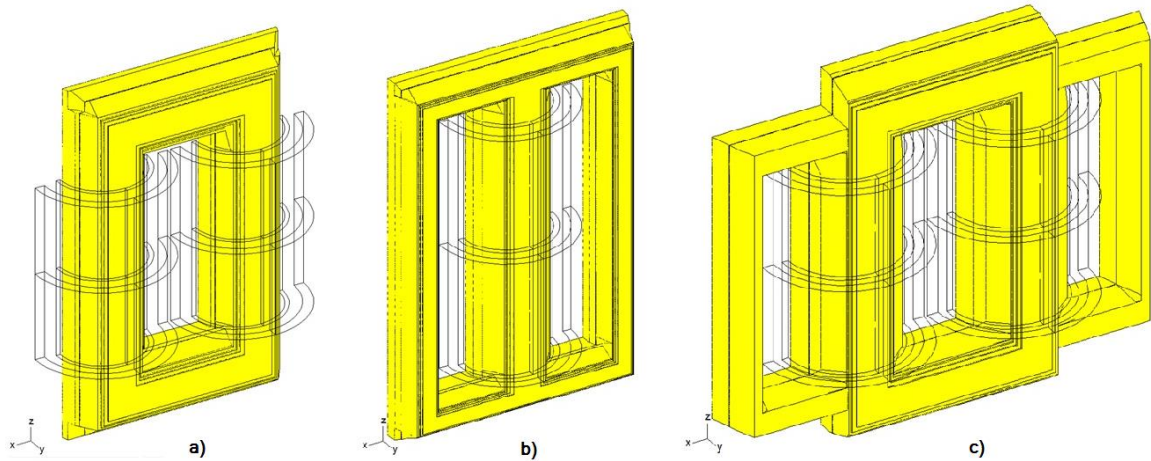


Fig. 3. Core types of a single limb transformer; a) two-limb core, b) one-limb core (with two back-closing limbs), c) four-limb core

The core types used in three-phase transformers are shown in Fig. 3.

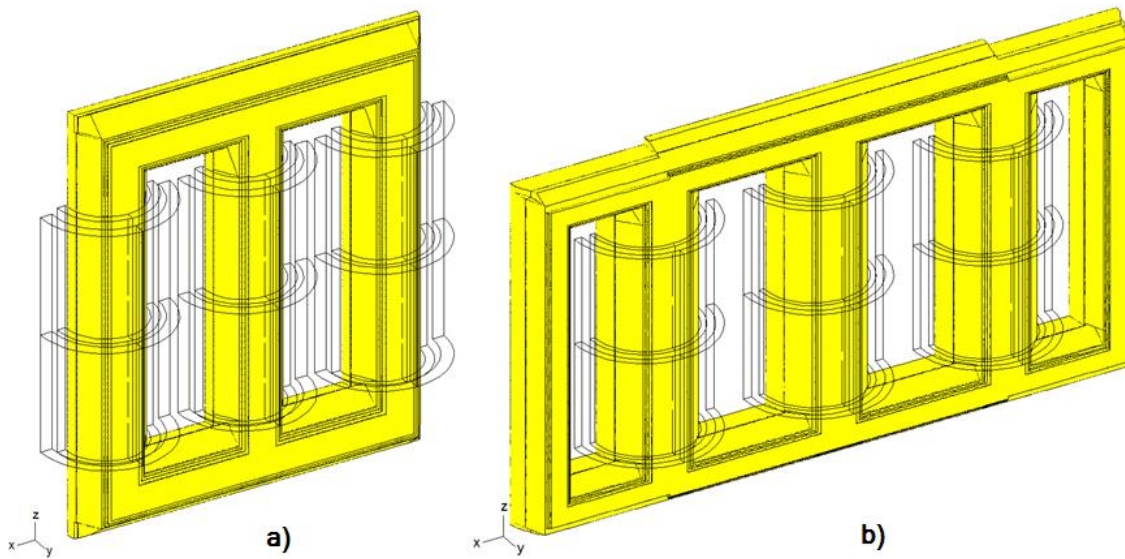


Fig. 4. Core implementation of three-phase transformers; a) three-limb core, b) five-limb core

1.2.2 Clamping structure

The core of a large power transformer is stabilized by means of a corresponding clamping structure. This structure protects the core against forces occurring [2]. The clamping structure at the upper and lower yoke can either be fabricated from wood or iron. For additional stability, optional tie bars can be attached along the main limbs between the upper and lower clampings.

1.2.3 Windings

The windings of large power transformers can be roughly classified as cylindrical windings and disk windings. Depending on the application and on the voltage level, different types of windings can be combined with one another (e.g.: cylindrical winding on low voltage side and disk winding on high voltage side)

Cylindrical windings

This type of winding is mainly used at comparatively low voltages and high currents. This is due to the lower distances between the single conductors and therefore reduced dielectric strength. The winding can be manufactured of several axial and/or radial parallel conductors. In case of large transmission capacities, drilled conductors must be installed to counteract current displacement effects and resulting in increased additional losses [2].

Disc windings

At higher voltage levels, disc windings are preferred. These consist of a plurality of axial parallel coils constructed from two or more correspondingly twisted parallel solid, drilled conductors. If a higher voltage withstand capability is required, the coils are designed to be interleaved with one another or, alternatively, the voltage distance between two conductors will be increased using blind conductors.

1.2.4 Shielding of stray flux

Since both the tank and the clamping structure (unless made of wood or non-magnetic steel) are manufactured of ferromagnetic steel, high losses and resulting high temperatures can occur in these components due to induced eddy currents. In order to reduce this, a tank shielding or/and yoke shielding components can be installed. Shielding packages on the tank walls consist of laminated electrical steel packages and can be either arranged in horizontal direction (against eddy currents resulting from vertically arranged conductors) or in the vertical direction (against eddy currents resulting from horizontally arranged conductors, e.g. winding conductors). Yoke shielding packages are manufactured of laminated steel to protect the clamping structure from too high temperatures [3].

1.3 Losses

The losses of a power transformer can be divided into two categories, the no-load losses and the load-losses or copper losses [4].

No-load loss

If a transformer is operated without load, a current for magnetizing the iron core is flowing and energy is dissipated. At a constant operating voltage, the core loss is constant in every load state [4]. The no-load losses of a transformer are proportional to the square of the magnetic flux density and to the square of the operational voltage ($P_{Fe} \sim B^2 \sim U^2$) [2].

Load loss

The load losses of a power transformer are dependent on the current flowing through the windings. Since the magnetizing current is too small to cause perceptible losses, this type of loss is only present at different load states. The load losses of a power transformer are proportional to the square of the load current ($P_{Cu} \sim I^2$) and can be divided into three categories [4].

Resistive loss

The resistive losses of transformer windings are dependent on the material used for manufacturing, its dimensions such as total length, conductor width, conductor height and the total current [5]. In order to reduce this type of losses at a given current, the cross-section of the conductor has to be increased or the number of turns has to be decreased [4].

Eddy current loss in winding conductors

Eddy current losses in transformer windings are mainly caused by radial and axial leakage flux in the windings. Due to the voltages induced thereby, currents are caused which lead to non-uniform current density in the conductors themselves. The resulting increase in losses is called additional losses. A possibility to reduce this effect is to subdivide the conductor into strands insulated from each other or to reduce the total cross section of the windings [4].

Eddy current loss in ferromagnetic steel parts

The leakage flux, which depends on the total current, can also cause eddy currents and hysteresis currents in ferromagnetic steel parts, such as the tank, the clamping structure or the tie bars [5]. Compared to the amount of resistive losses and eddy current losses in the winding conductors, the amount of eddy current loss in steel parts is rather low. A model of a five-limb core transformer with the ferromagnetic steel parts mentioned and tank shielding included is shown in Fig. 5.

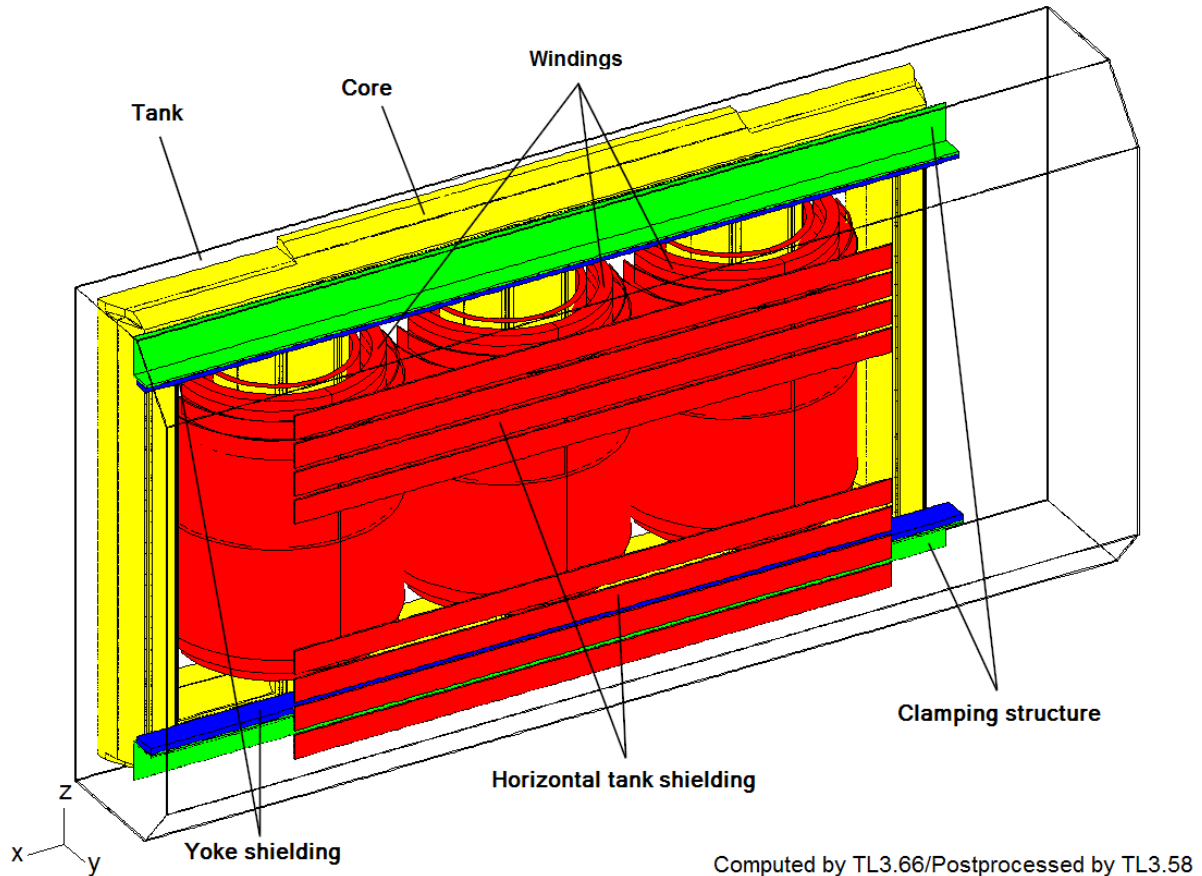


Fig. 5. FE-Model of a five-limb core transformer with tank, clamping structure, tank shielding and yoke shielding (without tie bars)

Due to customer requirements or over temperatures resulting from excessive losses, it is important to determine the losses in the design process as precisely as possible.

1.4 Scope of work

The main task of this thesis is the calculation of the additional losses in large power transformer windings using a three-dimensional finite element model. Currently, the additional losses of transformers manufactured at Siemens Transformers Weiz are determined based on a two-dimensional rotationally symmetric finite element model. To estimate the advantage of using a three-dimensional model in the design process, five transformers (one of each core type) have been investigated. The second part of this thesis examines the effect of modelling of disk windings in a 3D FEM-model on the eddy current losses in parts made of ferromagnetic steel. This investigation is also carried out for each of the five benchmark transformers.

2 Calculation methods and modelling

2.1 Calculation of eddy current and hysteresis-losses in non-active steel parts

2.1.1 Transformer model

A typical finite element model of a transformer for calculating the eddy current loss and the hysteresis loss in iron parts consists of a tank, a core, windings and a clamping structure. As shown in Fig. 6, additional tie bars for increased stability as well as tank shielding and yoke shielding can be installed. To decrease the calculation time, usually one half of a transformer (either the high voltage side or the low voltage side) is modelled [3]. A half model of a five-limb core transformer with horizontal tank shielding is shown in Fig. 5, a model of a three-limb core transformer with vertical tank shielding is shown in Fig. 6. The FEM models at Siemens Transformers Weiz are created with the tool "TrafoLoss".

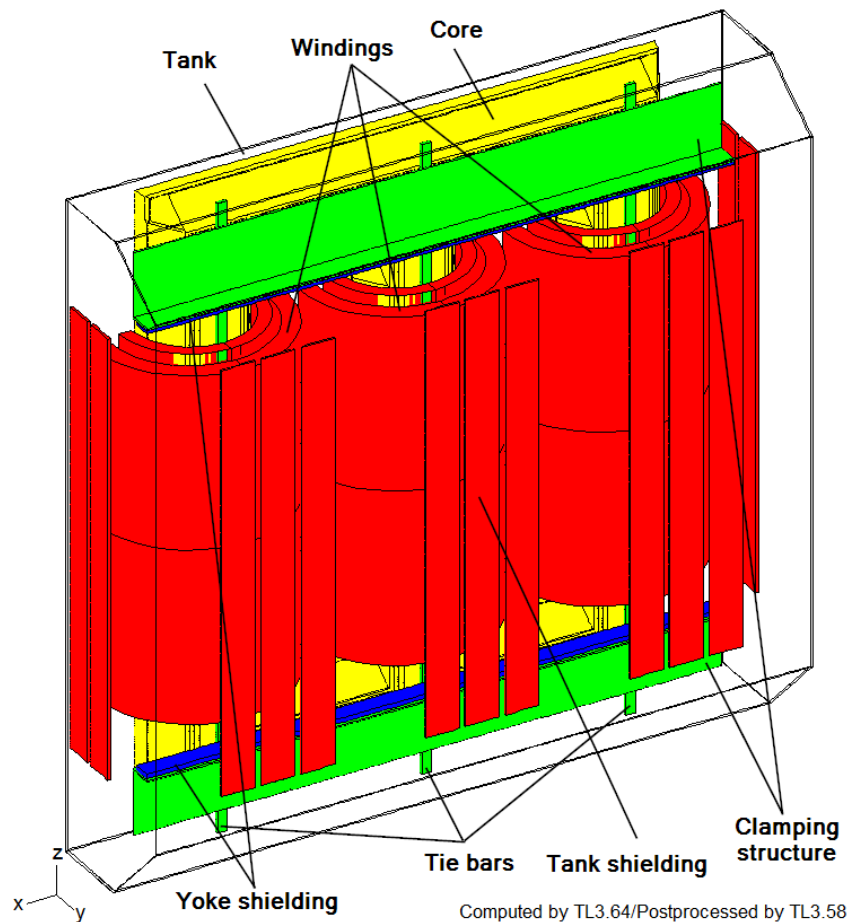


Fig. 6. FE Model of a three-limb core transformer

The laminated core is modelled as non-conducting, magnetically anisotropic and nonlinear material. The tank, the clamping structure and the tie bars are made of ferromagnetic steel. In

the FEM-model, these components are considered as conducting, isotropic and non-linear parts. Various shielding are modelled as laminated, anisotropic and non-linear steel [3].

2.1.1.1 Winding modelling

As described in subsection 1.2.3, the windings of large power transformers can basically be divided into cylindrical coils and disk windings. In the 3D FEM-model actually every type of winding is taken into account by one cylindrical coil with a mean current density, even if the real winding consists of more than one radial layer (cylindrical winding) or several axial parallel disks. An investigation if this is a good approximation, or if a more accurate division into several radial or axial parallel coils should be done, is described in section 0.

2.1.2 Mathematical model

As described in subsection 2.1.1, the transformer model consists of various conducting and non-conducting parts. The non-conducting parts, such as the core, the tank- and the yoke shielding, the air and the oil can be summarized to a non-conducting insulating region Ω_i . The tank, the clamping structure and the tie bars are made of conducting material and will further be combined to the conducting region Ω_c . A basic description of the field model and the boundaries is shown in Fig. 7, where Γ_B is a surface with a magnetic surface charge density b , Γ_{Hi} describes a magnetic wall with a given surface current density \mathbf{K} and Γ_{Hc} is a surface vertical to the magnetic field lines. The electrodes Γ_E , where $\mathbf{E} \times \mathbf{n} = 0$ and the border between conducting and non-conducting region Γ_{ci} are always symmetry planes [6]. The windings are included in Ω_i , since no eddy currents in them are taken into account when computing the electromagnetic field.

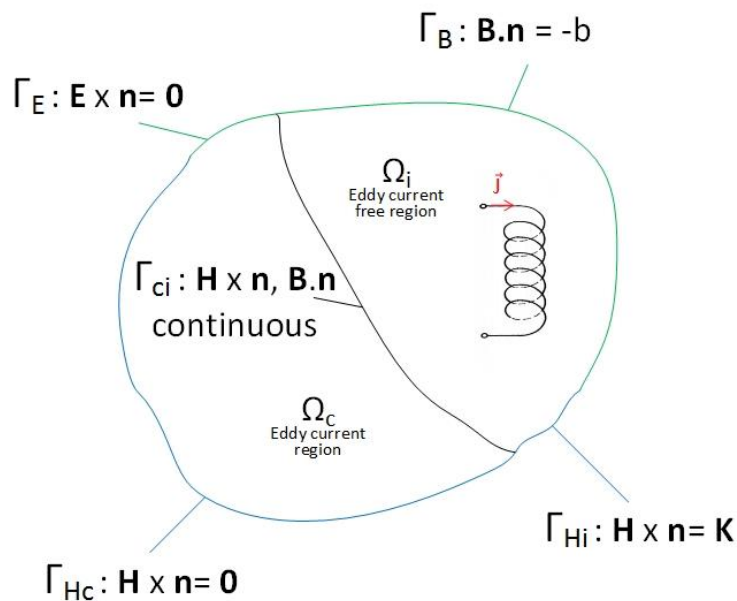


Fig. 7. Basic field model

Power transformers are usually operated with alternating currents of a frequency of 50 Hz or 60 Hz. This leads to the following four simplified Maxwell's equations in the frequency domain:

$$\text{curl}\mathbf{H} = \mathbf{J}, \quad (2.1)$$

$$\text{curl}\mathbf{E} = -j\omega\mathbf{B}, \quad (2.2)$$

$$\text{div}\mathbf{B} = 0, \quad (2.3)$$

$$\text{div}\mathbf{J} = 0. \quad (2.4)$$

\mathbf{H} describes the magnetic field intensity and \mathbf{J} is the current density of the eddy currents. \mathbf{E} is the electrical field intensity, ω is the angular frequency and \mathbf{B} the magnetic flux density.

$$\mathbf{B} = \mu\mathbf{H}, \quad (2.5)$$

$$\mathbf{E} = \rho\mathbf{J}. \quad (2.6)$$

The material relationships between the field quantities are described in (2.5) and (2.6), where μ is the nonlinear magnetic permeability and describes the relationship between \mathbf{B} and \mathbf{H} in magnetic steel. Since it is not possible, that \mathbf{B} and \mathbf{H} are both sinusoidal, a frequency domain treatment of these parameters is not strictly possible. As an approximation, both, \mathbf{B} and \mathbf{H} will be assumed to be sinusoidal and to obey a nonlinear relationship between their peak values [7]. The electrical resistivity ρ describes the relationship between \mathbf{E} and \mathbf{J} .

Because of the quasi static approximation, the eddy current density is divergence free ((2.4)). Therefore it is possible to write \mathbf{J} as the curl of the impressed current vector potential \mathbf{T}_0 , whose curl describes the impressed current density in the windings and of a reduced current vector potential \mathbf{T} .

$$\mathbf{J} = \text{curl}(\mathbf{T} + \mathbf{T}_0). \quad (2.7)$$

The introduction of potential functions is necessary for the application of the finite element method [6].

Equation (2.1) (Ampere's law) and (2.7) lead to the representation of the magnetic field in the conducting region Ω_c :

$$\mathbf{H} = \mathbf{T} + \mathbf{T}_0 - \text{grad}\Phi \text{ in } \Omega_c, \quad (2.8)$$

where Φ is a magnetic scalar potential. Because of the absence of eddy currents in the non-conducting region Ω_i the current vector potential is zero there [3]. This leads to

$$\mathbf{H} = \mathbf{T}_0 - \text{grad}\Phi \text{ in } \Omega_i, \quad (2.9)$$

for the magnetic field in the non-conducting region. Since \mathbf{T} and Φ describe the field in the conducting region and Φ describes the field in the non-conduction region, this way of introducing potential functions is called $\mathbf{T}, \Phi - \Phi$ formulation.

Applying (2.7) and (2.8) to Faraday's law of induction in (2.2) the differential equation

$$\text{curl}(\rho \text{curl} \mathbf{T}) + j\omega\mu\mathbf{T} - j\omega\mu \text{grad}\Phi = -\text{curl}(\rho \text{curl} \mathbf{T}_0) - j\omega\mathbf{T}_0 \text{ in } \Omega_c, \quad (2.10)$$

is obtained in the conducting region. Since (2.10) is a vectorial differential equation with the potentials \mathbf{T} and Φ , it is necessary to introduce a second scalar differential equation in the conducting region.

Equation (2.3), (2.5) and (2.8) lead to

$$\text{div}(\mu\mathbf{T} - \mu \text{grad}\Phi) = -\text{div}(\mu\mathbf{T}_0) \text{ in } \Omega_c, \quad (2.11)$$

a scalar differential equation in combination with (2.9) and (2.5) in the non-conducting region, Gauss' law for magnetism can also be used. This leads to the differential equation for the non-conducting region:

$$-\text{div}(\mu \text{grad}\Phi) = -\text{div}(\mu\mathbf{T}_0) \text{ in } \Omega_i. \quad (2.12)$$

The boundary conditions for this field problem with the boundaries introduced in Fig. 7 are: [6]

$$\rho \text{curl} \mathbf{T} \times \mathbf{n} = -\rho \text{curl} \mathbf{T}_0 \times \mathbf{n} = 0 \text{ at } \Gamma_E, \quad (2.13)$$

$$\mathbf{n} \cdot \mu(\mathbf{T} - \text{grad}\Phi) = -\mathbf{T}_0 \cdot \mathbf{n} = 0 \text{ at } \Gamma_E, \quad (2.14)$$

$$\mathbf{n} \times \mathbf{T} = \mathbf{n} \times \mathbf{T}_0 = 0 \text{ at } \Gamma_{Hc}, \quad (2.15)$$

$$\Phi = \Phi_0 \text{ at } \Gamma_{Hc}, \quad (2.16)$$

$$\mu \frac{\partial \Phi}{\partial n} = b + \mu\mathbf{T}_0 \cdot \mathbf{n} \text{ at } \Gamma_B, \quad (2.17)$$

$$\Phi = \Phi_0 \text{ at } \Gamma_{Hi}, \quad (2.18)$$

$$\mathbf{n} \times \mathbf{T} = 0 \text{ at } \Gamma_{ci}, \quad (2.19)$$

$$\mathbf{n}_c \cdot (\mu\mathbf{T}_0 + \mu\mathbf{T} - \mu \text{grad}\Phi) + \mathbf{n}_i \cdot (\mu\mathbf{T}_0 - \mu \text{grad}\Phi) = 0 \text{ at } \Gamma_{ci}. \quad (2.20)$$

Because of the absence of magnetic surface charges, b in (2.17) can be assumed to be zero.

The potentials \mathbf{T} and Φ are approximated as

$$\mathbf{T} \approx \mathbf{T}_n = \sum_{j=1}^{n_1} T_j \mathbf{N}_j, \quad (2.21)$$

$$\Phi \approx \Phi_n = \Phi_D + \sum_{j=1}^{n_2} \Phi_j N_j. \quad (2.22)$$

The vector potential \mathbf{T} is described by a set of edge based vector basis functions \mathbf{N}_j and the scalar potential Φ is represented by the node based scalar basis functions N_j .

To describe the impressed current vector potential, edge based vector basis functions will also be used. For computing the coefficients t_i , the integrals of \mathbf{T}_0 along the edges of the finite element mesh have to be computed [6]:

$$\mathbf{T}_0 \approx \sum_{\text{edge } i} t_i \mathbf{N}_i, \quad t_i = \int_{\text{edge } i} \mathbf{T}_0 d\mathbf{l}, \quad (2.23)$$

Applying Galerkin's method to the differential equation in (2.10) and, because of symmetry reasons, to the time derivate of (2.11) as well as to the differential equation in (2.12) leads to the algebraic equations

$$\begin{aligned} & \int_{\Omega_c} \text{curl} N_i \cdot \rho \text{curl} T_n d\Omega + \int_{\Omega_c} N_i \cdot (j\omega\mu T_n - j\omega\mu \text{grad} \Phi_n) d\Omega = \\ & = - \int_{\Omega_c} \text{rot} N_i \cdot \rho \text{rot} T_0 d\Omega - \int_{\Omega_c} N_i \cdot j\omega\mu T_0 d\Omega, \quad (i = 1, 2, \dots, n_1), \end{aligned} \quad (2.24)$$

$$\begin{aligned} & \int_{\Omega_c + \Omega_i} \text{grad} N_i \cdot j\omega\mu \text{grad} \Phi_n d\Omega - \int_{\Omega_i} \text{grad} N_i \cdot j\omega\mu T_n d\Omega = \\ & = - \int_{\Omega_c + \Omega_i} \text{grad} N_i \cdot j\omega\mu T_0 d\Omega - \int_{\Gamma_B} N_i j\omega b d\Gamma, \quad (i = 1, 2, \dots, n_2), \end{aligned} \quad (2.25)$$

where the potential is approximated as described in (2.21), (2.22) and (2.23) [6].

Because of the absence of magnetic surface charges b , the last term of equation (2.25) is zero.

To solve the resulting algebraic equations, a preconditioned conjugated gradient method is used. Due to the nonlinearity between \mathbf{B} and \mathbf{H} , the nonlinear problem is solved by updating the permeability in each iteration step [3].

After solving the equations, the eddy current losses as well as the specific losses in laminated iron parts (tank shielding, yoke shielding, etc.) can be determined by evaluating the integrals in equation (2.26) (eddy current loss) and equation (2.27) (specific loss in laminated steel), where Ω_{eddy} is the volume of conducting parts in which eddy currents are occurring and Ω_{lam} summarizes the volume of all parts made of laminated steel (core, shields, ...):

$$P_{eddy} = \frac{1}{2} \int_{\Omega_{eddy}} \rho |\mathbf{J}|^2 d\Omega, \quad (2.26)$$

$$P_{iron} = \frac{1}{2} \int_{\Omega_{lam}} \rho_d p(|\mathbf{B}|) d\Omega. \quad (2.27)$$

In equation (2.27), ρ_d describes the mass density of steel and p is a function of the absolute value of \mathbf{B} provided by the manufacturer [3].

2.2 Calculation of additional winding losses

2.2.1 2D transformer model

Currently, the additional winding losses are determined from a rotationally symmetric two-dimensional finite element model. This has the disadvantage that only one cross-section of the transformer can be considered. The fact that the geometry changes in azimuthal direction is not taken into account exactly. Fig. 8 indicates the cross-section which the 2D model is based on.

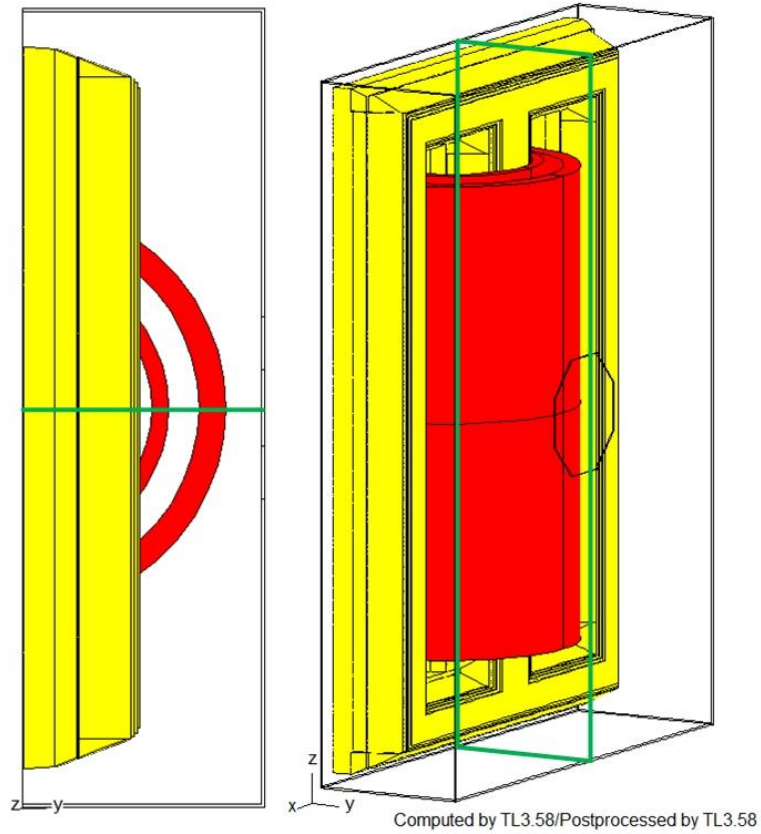


Fig. 8. Explanation of the cross section on which the rotationally symmetric model is based using a single-phase transformer

The cross-section shown in Fig. 8 leads to the geometry of the 2D model in Fig. 9, where d_2 is the distance from the outer winding to the tank wall. Since the distance from the top of the windings to the ferromagnetic material (tank, yoke) changes in azimuthal direction, d_1 is not the distance between the top edge of the higher winding and the tank cover, and also not the distance between top point of this winding to the yoke. d_1 is calculated with a formula from an internal design rule, which approximately takes into account, that d_1 is changing in azimuthal direction.

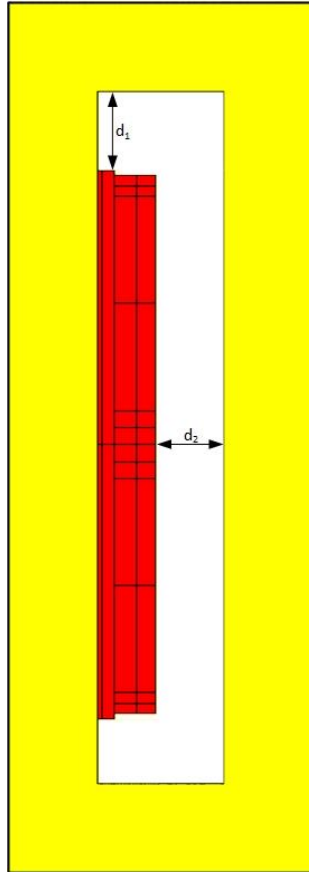


Fig. 9. Geometry of the 2D model

The resulting 2D model in Fig. 9 is a rotationally symmetric quarter model, with its axis at the left side of the model.

2.2.1.1 *Modelling of windings*

Compared to the consideration of transformer windings in the presently used 3D FEM-model for calculation of eddy current losses and specific losses in steel parts, the windings in the 2D model for calculating the additional winding losses are modelled more accurately. In fact, there are two possibilities. On the one hand, disk windings can be represented by as many axial parallel cylindrical coils, as winding parts are present (similar winding parts can be summarized). Cylindrical layer windings are thereby modelled by one cylindrical coil per layer in radial direction and each coil consists of one axial block (inner winding in Fig. 10). On the other hand, each winding conductor, no matter what type of winding is used, could be modelled as shown in Fig. 11.

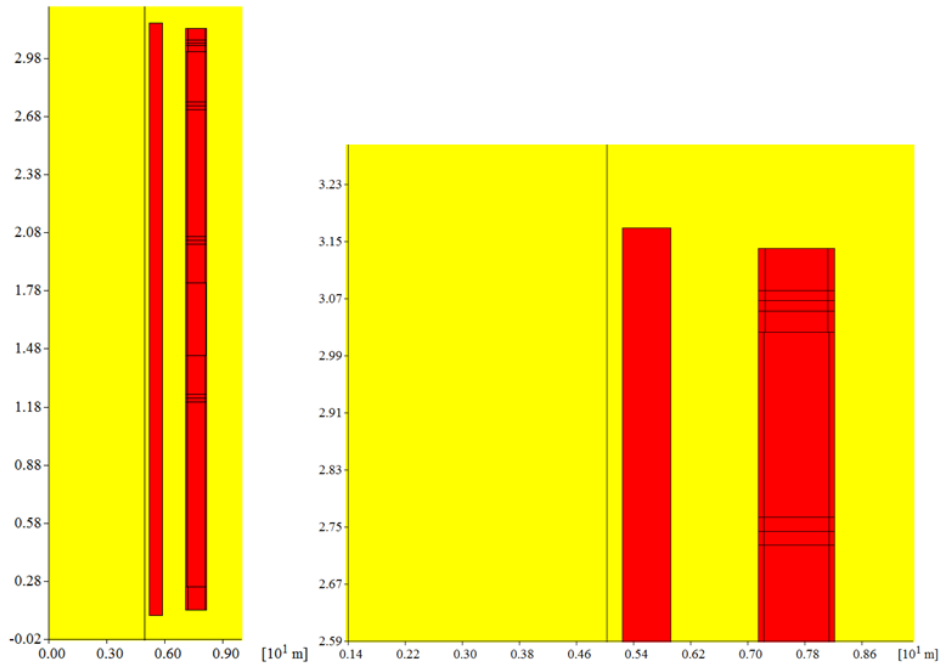


Fig. 10. Coarse modelling of transformer windings

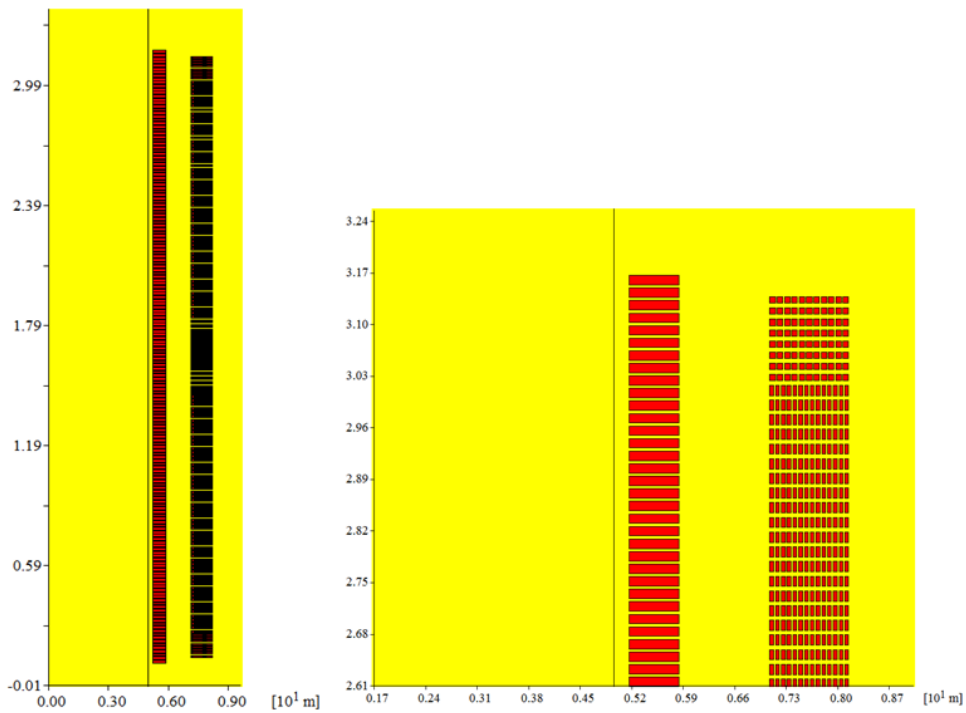


Fig. 11. Detailed modelling of winding conductors

For further investigations, the model in Fig. 10 will be called “coarse model” and the one in Fig. 11 labelled as “detailed model”.

2.2.1.2 Mathematical model

No matter which 2D model (coarse or detailed) will be used for computing the magnetic field in the transformer, the theoretical background of the additional loss calculation is the same. It is based on a magnetic field calculation with a 2D FEM-model with a subsequent analytical calculation of the radial and axial winding losses. The analytical model is based on the assumption, that the magnetic field over a single conductor with the width a , the height b and the conductivity σ (reciprocal of ρ) is constant. This is permissible because of the small cross-section of the used conductors and the relatively low operating frequency (width, height $<$ penetration depth). The magnetic field is dependent on the position of the conductor in radial and in z -direction. A sketch of the analytical model is shown in Fig. 12.

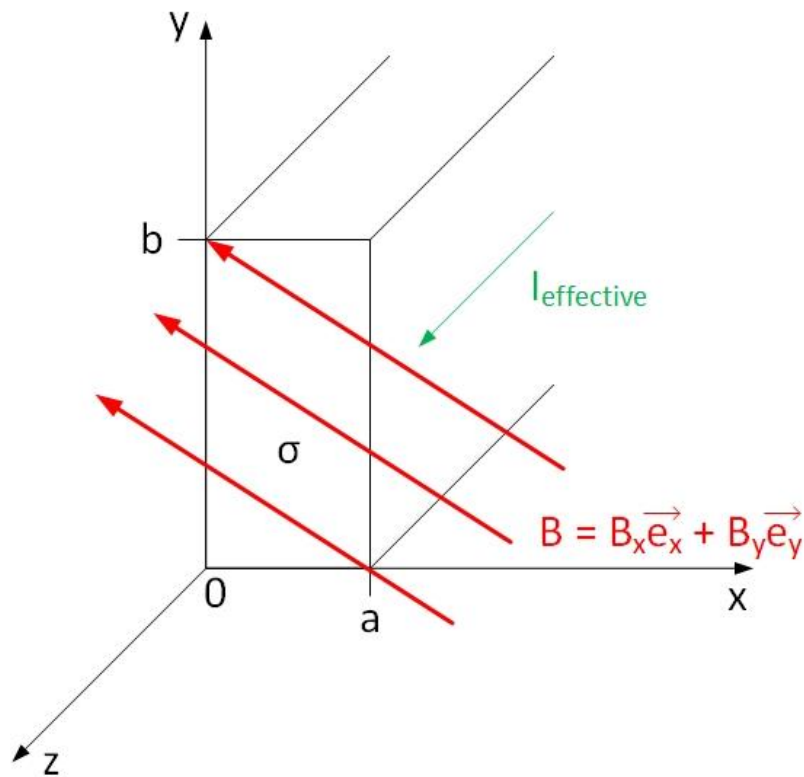


Fig. 12. Loss calculation in the 2D model

Because of a changing magnetic flux, resulting from the current in the windings, Faraday's law of induction could be applied for solving the analytical model:

$$\text{curl } \mathbf{E} = -j\omega \mathbf{B}. \quad (2.28)$$

\mathbf{E} and \mathbf{B} can be assumed as

$$\hat{\mathbf{B}} = B_x \mathbf{e}_x + B_y \mathbf{e}_y, \quad (2.29)$$

$$\mathbf{E} = E(x, y) \mathbf{e}_z. \quad (2.30)$$

Applying the curl-operator to \mathbf{E} in (2.28) leads to

$$\text{curl } \mathbf{E} = \begin{vmatrix} \mathbf{e}_x & \mathbf{e}_y & \mathbf{e}_z \\ \frac{\partial}{\partial x} & \frac{\partial}{\partial y} & \frac{\partial}{\partial z} \\ 0 & 0 & E \end{vmatrix} = \frac{\partial E}{\partial y} \mathbf{e}_x - \frac{\partial E}{\partial x} \mathbf{e}_y. \quad (2.31)$$

Replacing \mathbf{B} and \mathbf{E} in (2.28) and separating them according to the dependence on the coordinates x and y , results in:

$$\frac{\partial E}{\partial y} = -j\omega B_x, \quad (2.32)$$

$$\frac{\partial E}{\partial x} = -j\omega B_y, \quad (2.33)$$

Solving the equations in (2.32) and (2.33) by integrating, leads to

$$E(x, y) = -j\omega(yB_x - xB_y) + E_0. \quad (2.34)$$

To calculate the peak current in the conductor, the surface integral over the current density \mathbf{J} have to be evaluated:

$$\sqrt{2}I = \int_{\Gamma} \mathbf{J} \cdot \mathbf{n} d\Gamma = \sigma \int_0^a \int_0^b E(x, y) dy dx = \sigma E_0 ab - j\omega\sigma \left(\frac{ab^2}{2} B_x - \frac{a^2b}{2} B_y \right), \quad (2.35)$$

Expressing the integration constant E_0 and substituting it in (2.34) leads to the final expression for $E(x, y)$. The Joule losses, representing the radial and axial additional losses of the conductor, can be calculated as

$$P = \frac{1}{2} \int_{\Omega} \frac{|\mathbf{J}|^2}{\sigma} d\Omega. \quad (2.36)$$

Evaluating this integral leads to the formula in equation (2.37), where the first term represents the resistive loss, the second term the radial additional losses (depending on B_x) and the third term represents the axial additional losses (depending on B_y) of the winding conductor:

$$P = l \frac{|I|^2}{\sigma ab} + l \frac{\omega^2 \sigma ab}{24} \left(b^2 |B_x|^2 + a^2 |B_y|^2 \right). \quad (2.37)$$

2.2.2 3D transformer model

As described in section 1.4, the scope of this thesis is to compute additional winding losses with a 3D FEM-model for several benchmark transformers. Since the windings are not modelled in the existing 3D FEM-model for calculating the eddy current losses in non-active steel parts, the computed field in the windings cannot be used for evaluating the additional winding losses of

the transformer (Fig. 13) with the required precision. Therefore, a new model, with modelled windings has to be generated (Fig. 14). The mathematical model for this application is the same as described in subsection 2.1.2. This feature is also implemented in the FEM-tool “TrafoLoss”.

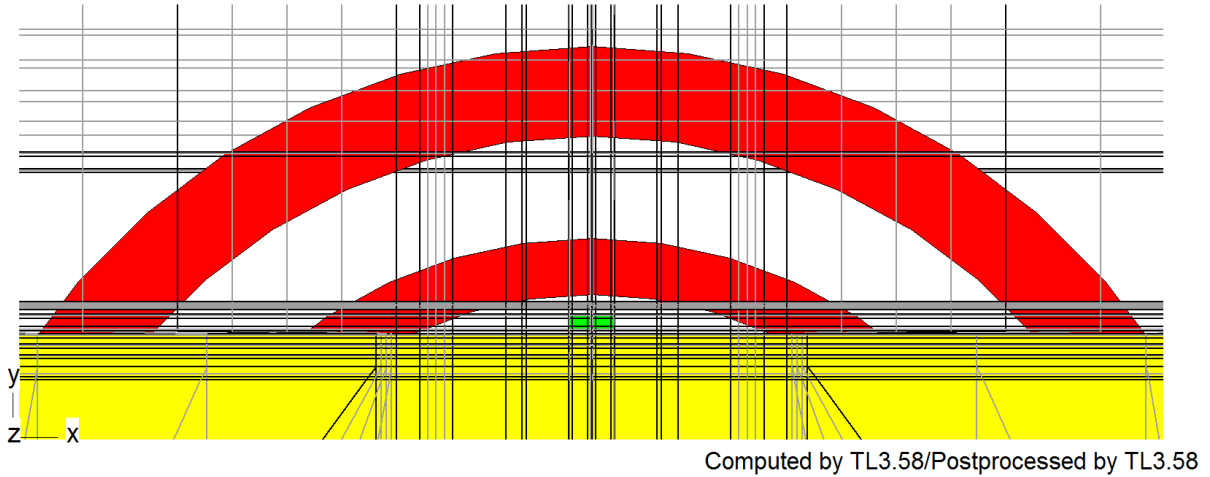


Fig. 13. Top view of a transformer model for calculating eddy current losses in steel parts

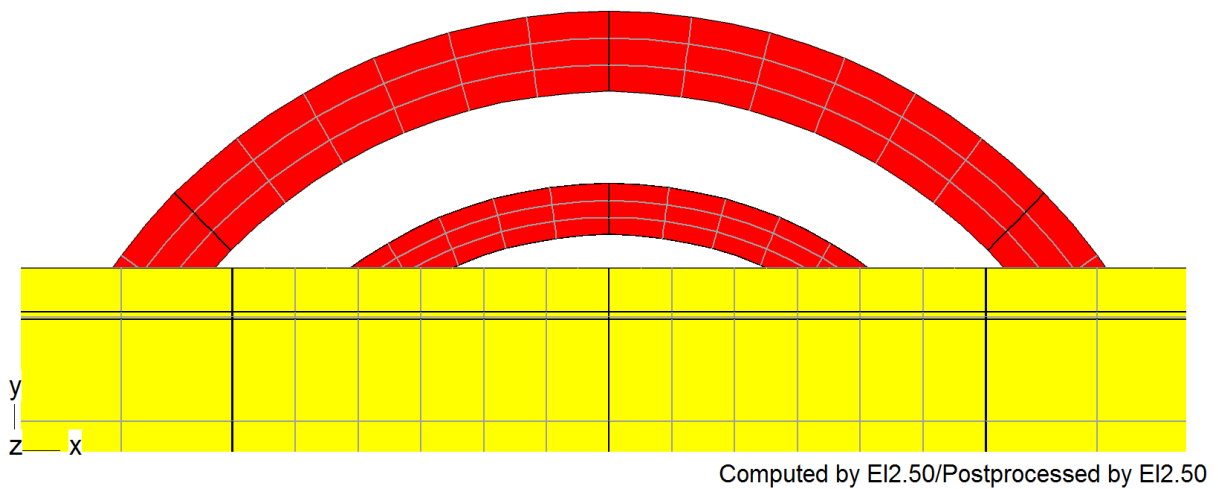


Fig. 14. Top view (without tank) of a transformer model for calculating additional winding losses

To get the necessary rounded arrangement of the finite elements in the windings, also the core has to be rounded. For computing the field in the windings, marginal parts like the tie bars will not be modelled. Also, the tank shielding will be simplified. A comparison of the two models of the same single-phase transformer is shown in Fig. 15.

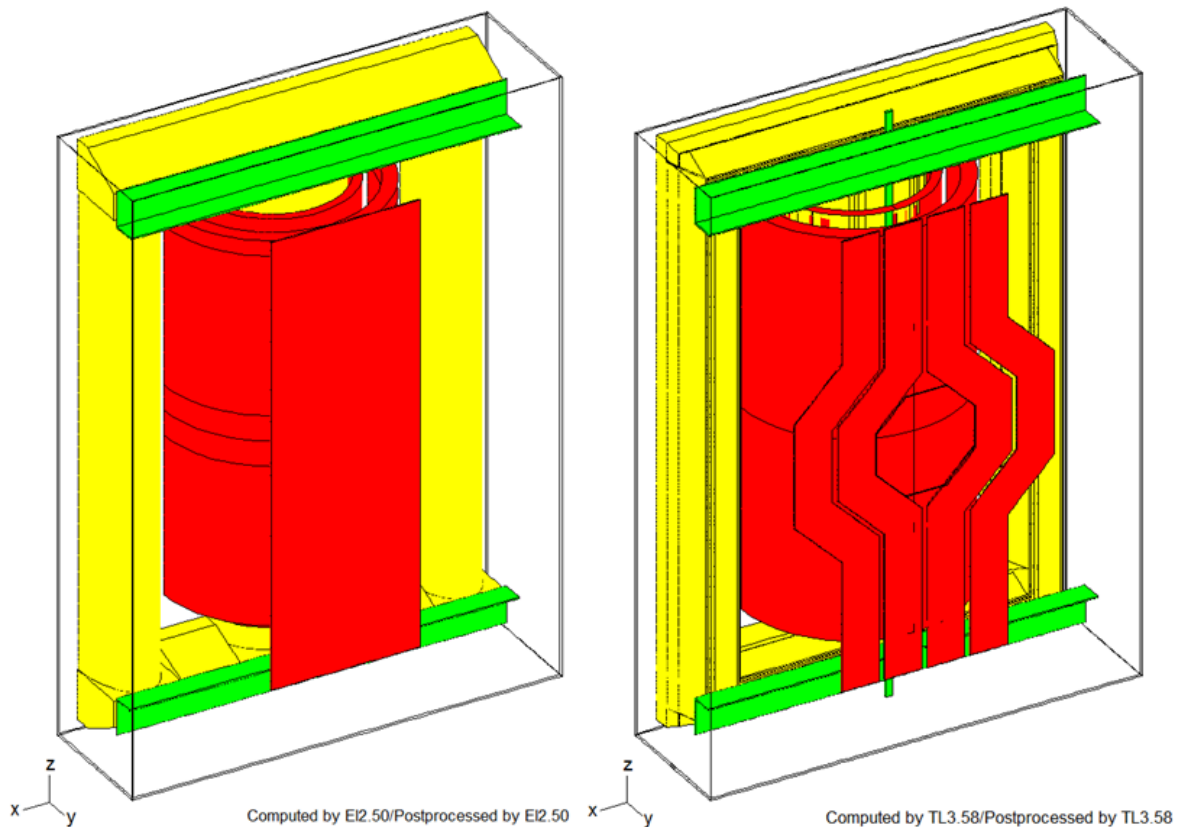


Fig. 15. left: 3D FEM-model for evaluating additional winding losses; right: 3D FEM-model for computing additional losses in non-active steel parts

2.2.2.1 Modelling of windings

In addition to generating an accurate finite element mesh in the windings, also the way of modelling by one or more radial or axial blocks should be considered. Because of the size of the 3D model, modelling every single conductor (as shown in Fig. 11) is not possible. Two cases are therefore considered in the further investigations. On the one hand, the coils will be modelled by one radial and one axial block per winding, independent of winding type being used. On the other hand, disk windings will be considered, as shown in the coarse 2D model in Fig. 10. The results of this investigation can be found in subsection 3.2.1.

2.2.2.2 Mathematical model

The calculation of additional losses in the 3D FEM-model (no matter how the windings are modelled) is like the 2D model in subsection 2.2.1.2. The main difference of using the 3D model is that the field is assumed to change in the azimuthal direction. This must be considered in the subsequent analytical model shown in Fig. 16.

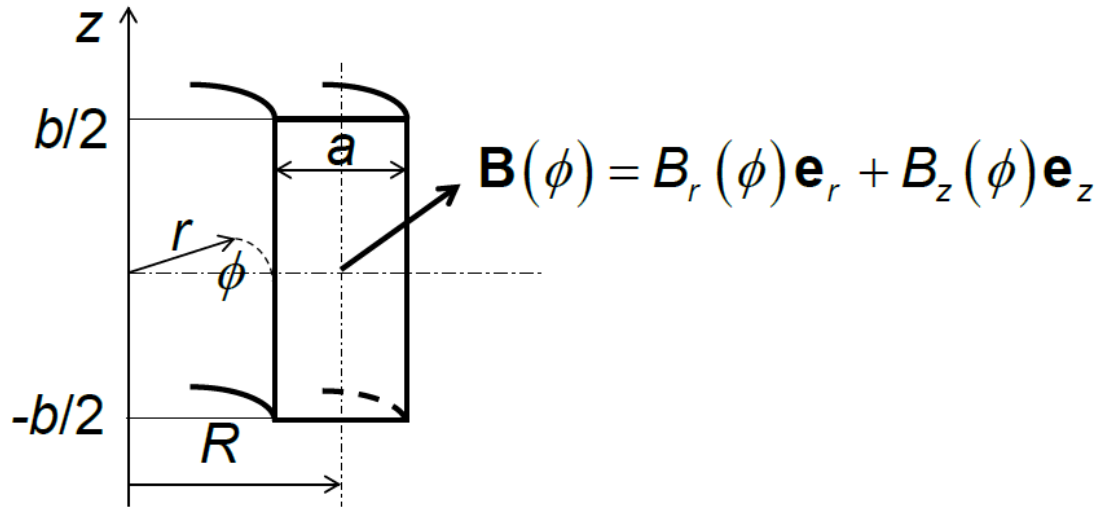


Fig. 16. Loss calculation in the 3D model [8]

The magnetic flux density \mathbf{B} is dependent on the conductor position and can be expressed by its components in radial and axial direction. This leads to:

$$\mathbf{B}(r, z, \phi) = B_r(r, z, \phi)\mathbf{e}_r + B_z(r, z, \phi)\mathbf{e}_z. \quad (2.38)$$

The Gauss's law for magnetism in cylindrical coordinates:

$$\text{div } \mathbf{B} = \frac{1}{r} \frac{\partial}{\partial r} \left(r \frac{\partial B_r}{\partial r} \right) + \frac{\partial B_z}{\partial z} = 0, \quad (2.39)$$

and the assumption that B_r is nearly constant over the conductor cross-section if the condition $R \gg a$ is fulfilled as well as that B_z is also constant over the cross-section result in:

$$B_r(r, z, \phi) = \frac{B_r(\phi)}{r} R \quad (2.40)$$

$$B_z(r, z, \phi) = B_z(\phi) \quad (2.41)$$

$$\text{curl } \mathbf{E} = -j\omega\mathbf{B} \quad (2.42)$$

$$\mathbf{E} = E\mathbf{e}_\phi \quad (2.43)$$

Applying the curl-operator in cylindrical coordinates to \mathbf{E} from Faraday's law of induction in (2.42) combined with the assumption that \mathbf{E} has only a tangential component leads to:

$$\text{curl } \mathbf{E} = \begin{vmatrix} \frac{1}{r} \mathbf{e}_r & \mathbf{e}_\phi & \frac{1}{r} \mathbf{e}_z \\ \frac{\partial}{\partial r} & \frac{\partial}{\partial \phi} & \frac{\partial}{\partial z} \\ 0 & rE & 0 \end{vmatrix} = -\frac{1}{r} \mathbf{e}_r \frac{\partial}{\partial z} (rE) + \frac{1}{r} \frac{\partial}{\partial r} (rE) \mathbf{e}_z \quad (2.44)$$

Replacing curl \mathbf{E} in equation (2.42) by (2.44), \mathbf{B} by (2.40) and (2.41) and separating the equation according to vector components, leads to

$$-\frac{1}{r} \frac{\partial}{\partial z} (rE) = -j\omega \frac{B_r(\phi)}{r} R = \frac{\partial}{\partial z} rE = j\omega B_r(\phi) R \quad (2.45)$$

$$\frac{1}{r} \frac{\partial}{\partial r} rE = -j\omega B_z(\phi) = \frac{\partial}{\partial r} rE = -j\omega B_z(\phi) r \quad (2.46)$$

Integrating these two equations leads to

$$E(r, \phi, z) = j\omega \left(B_r(\phi) R \frac{z}{r} - B_z(\phi) \frac{r}{2} \right) + \frac{U_0(\phi)}{r} \quad (2.47)$$

with the integration constant $U_0(\phi)$. Evaluating the surface integral over the cross-section of the conductor in Fig. 16 for the current density $\mathbf{J} = \sigma \mathbf{E}$ and expressing $U_0(\phi)$ from the resulting equation leads to:

$$\sqrt{2}I = \int_{\Gamma} \mathbf{J} \cdot \mathbf{n} d\Gamma = \sigma \int_{R-\frac{a}{2}}^{R+\frac{a}{2}} \int_{-\frac{b}{2}}^{\frac{b}{2}} E(r, \phi, z) dr dz, \quad (2.48)$$

$$U_0(\phi) = \frac{\sqrt{2}I}{\sigma b \ln \frac{R+\frac{a}{2}}{R-\frac{a}{2}}} + j\omega B_z(\phi) \frac{Ra}{2 \ln \frac{R+\frac{a}{2}}{R-\frac{a}{2}}} \quad (2.49)$$

The integral of the Joule' loss density in (2.50) can be now evaluated with the result for $U_0(\phi)$ used in equation (2.47). This results in equation (2.51) where the first term represents the resistive loss, the second term the axial additional losses and the third term the radial additional losses of one single conductor:

$$P = \frac{1}{2} \int_{\Omega} \frac{|\mathbf{J}|^2}{\sigma} d\Omega = \frac{1}{2} \int_0^{2\pi} \int_{-\frac{b}{2}}^{\frac{b}{2}} \int_{R-\frac{a}{2}}^{R+\frac{a}{2}} \sigma |E|^2 r dr dz d\phi \quad (2.50)$$

$$\begin{aligned}
&= |I|^2 \frac{2\pi}{\sigma b \ln \frac{R + \frac{a}{2}}{R - \frac{a}{2}}} \\
&+ \omega^2 \sigma \int_0^{2\pi} |B_z(\phi)|^2 d\phi \left[\frac{b}{2} \left[\frac{Ra \left(2 \cdot R^2 + \frac{a^2}{2} \right)}{8} - \frac{R^2 a^2}{4 \ln \frac{R + \frac{a}{2}}{R - \frac{a}{2}}} \right] \right. \\
&\left. + \omega^2 \sigma \left(\int_0^{2\pi} |B_r(\phi)|^2 d\phi \right) R^2 \frac{b^3}{2n} \ln \frac{-R + \frac{a}{2}}{R - \frac{a}{2}} \right] \quad (2.51)
\end{aligned}$$

3 Verification of the analytical 3D model

In order to verify whether the assumptions in subsection 2.2.2.2 are permissible and the method is correctly implemented in the 3D FEM software, various investigations have been carried out using a one-limb core transformer. This requires a comparison of the calculated resistive and additional winding losses from the 2D model to those from an equivalent rotationally symmetrical 3D model. Based on this model, the necessary accuracy in winding modelling has also been investigated.

3.1 Technical data

The single-phase transformer “T1” is designed for a nominal power of 116,67 MVA at a high voltage level of $500/\sqrt{3}$ kV and a low voltage level of 16,5 kV. The LV-winding consists of one layer with 60 turns and three axial parallel conductors with 79 strands (6,2x1,49 mm) per conductor. The HV-winding is constructed from six partly interleaved discs with voltage input in the middle of the winding, where three different conductors are used. The upper and the lower blocks are constructed of a drilled conductor with three strands (9x2,54 mm). The two blocks in the middle of the winding are manufactured of a drilled conductor with two strands (17,6x2,14 mm). In the other two blocks, too, a drilled conductor with three strands (13,9x1,74 mm) is used.

3.2 Rotationally symmetric 3D model

To verify the analytical 3D model for calculating the additional winding losses, the existing 2D model of the transformer “T1” should be converted into an equivalent rotationally symmetric 3D model. For this investigation, the HV-disk winding will be modelled of one axial parallel block.

The geometry of the coarse 2D model, as well as the geometry of the equivalent 3D model are shown in Fig. 17.

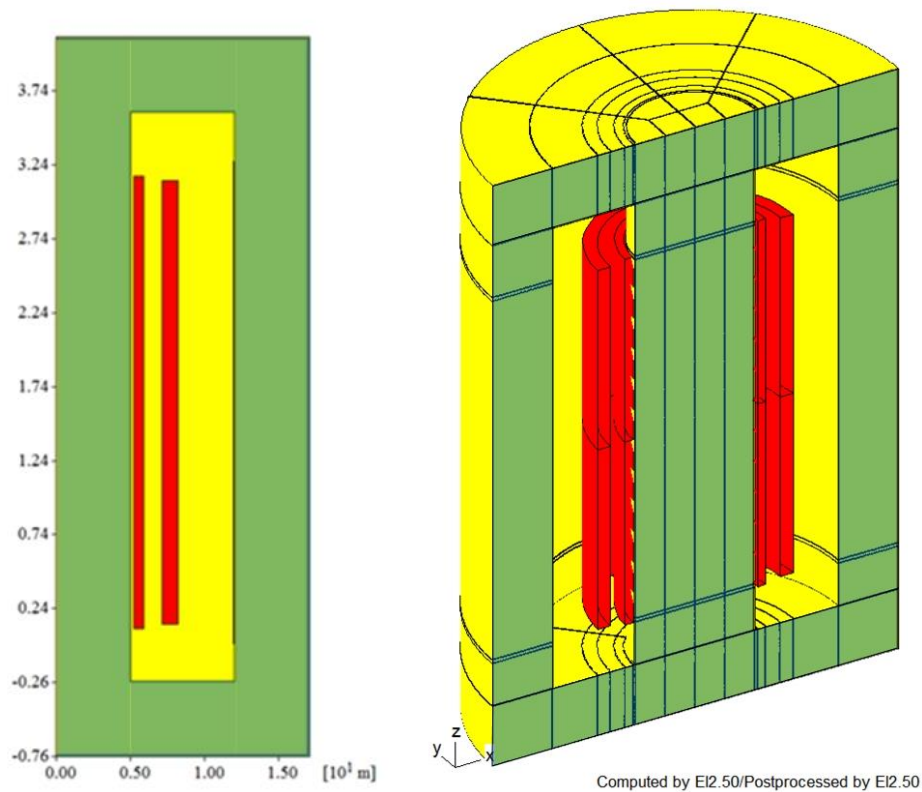


Fig. 17. "T1": left: existing 2D model, right: 3D model

To prove that the two models are equivalent for determining the additional winding losses, the radial and axial field in the low voltage winding as well as the flux density plots have been compared. The results of this comparison are shown in the Figs. 18 and 19.

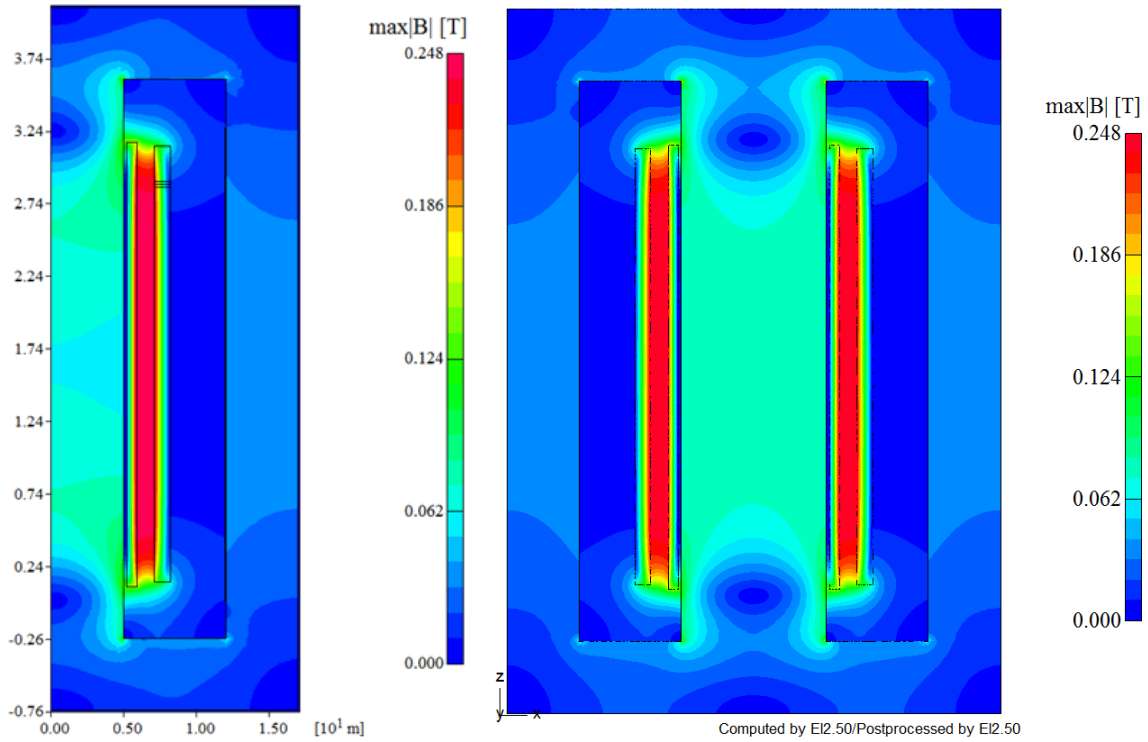


Fig. 18. "T1": left: Field plot of 2D model, right: Field plot of the rotational symmetric 3D model

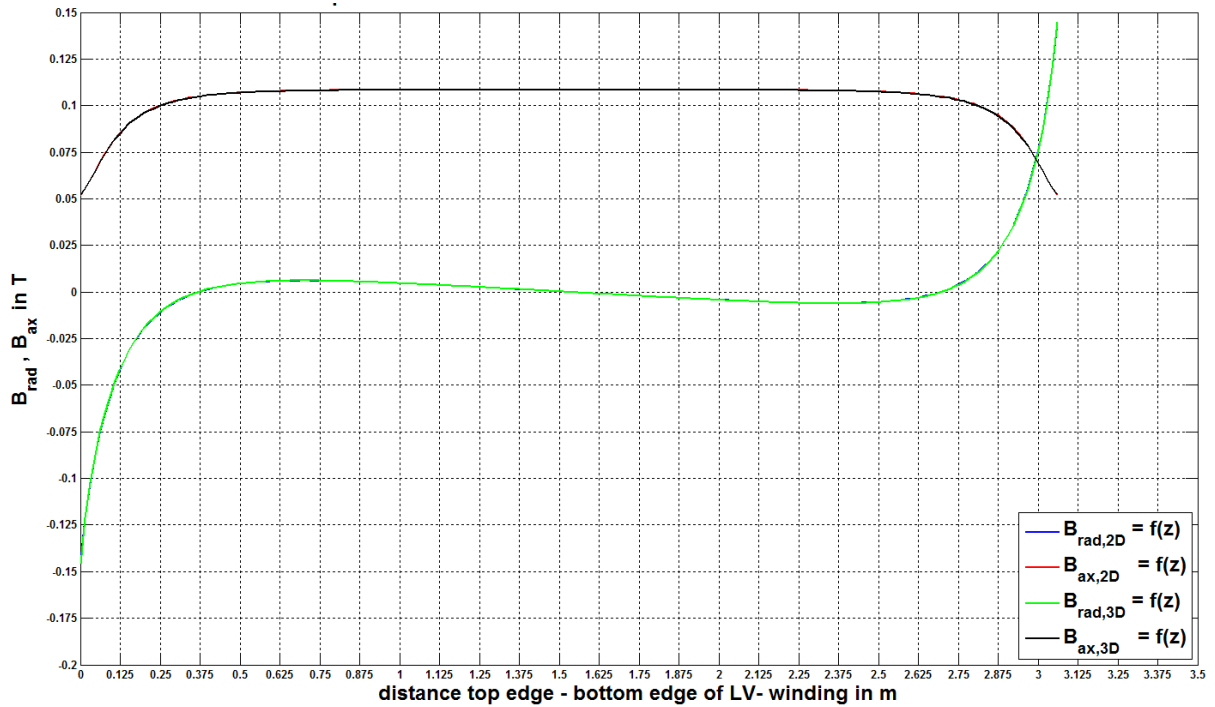


Fig. 19. "T1": Comparison of radial and axial fields between 2D model and 3D model in z-direction ($x=0$, $y=r_{midLV}$)

Beside the flux density plots in Fig. 18 and the radial and axial fields of the two models in Fig. 19 being identical, the fields are as expected. On the one hand the magnitude of the radial field, represented by the green and the black curve in Fig. 19, is high at the upper and lower winding end and low in the middle of the winding. On the other hand, the axial flux density reaches its maximum in the middle of the winding and is relatively low at the winding ends.

Because of the equivalence to the 2D model, further investigations will be done by the means of the rotationally symmetric 3D model.

3.2.1 Comparison of different winding modelling

A conclusion of the subsections 2.1.1.1, 2.2.1.1 and 2.2.2.1 is that, depending on the application, windings are implemented differently in the models. For calculating the additional losses in the windings, two possibilities are conceivable. The first method (each winding modelled by one cylindrical coil) is currently used in the 3D model for calculating the eddy current losses in non-active steel parts. To check, if this method is also permissible for calculating the additional winding losses in the 3D model, a comparison between this method and the currently used method in the 2D model is carried out.

The geometry plots of the rotationally symmetric 3D models are shown in Fig. 20.

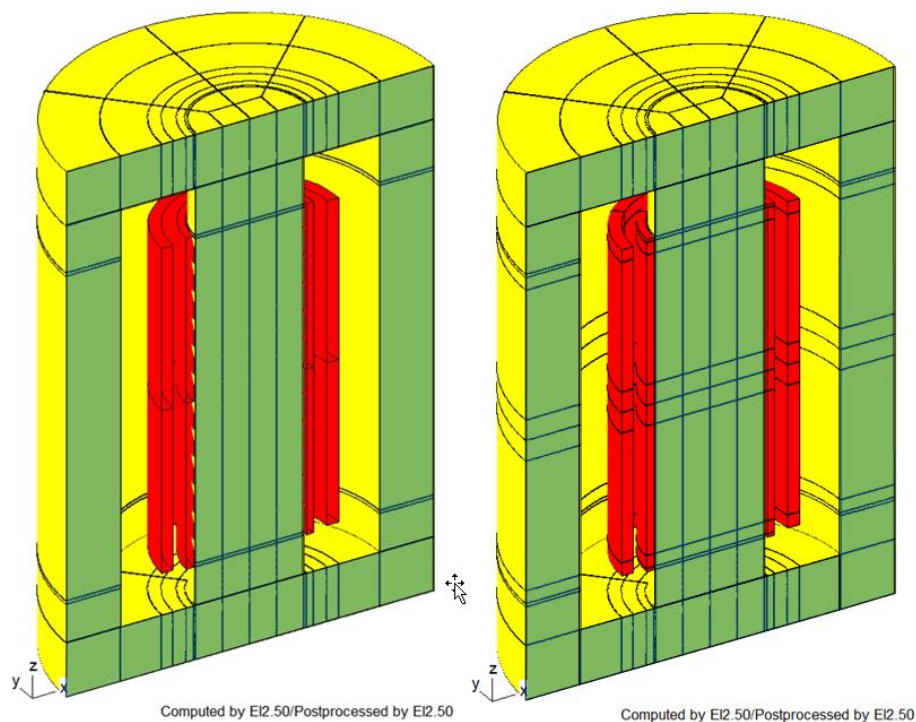


Fig. 20. "T1": left: HV-disk winding modelled with one axial block, right: HV-winding modelled with six axial blocks

Due to voltage withstand reasons the transformer's HV-winding consists of several interleaving discs with different conductors used. In the existing coarse 2D model, this is considered by the means of six axial parallel coils. Fig. 21 shows the distribution of these coils in the equivalent rotationally symmetric model.

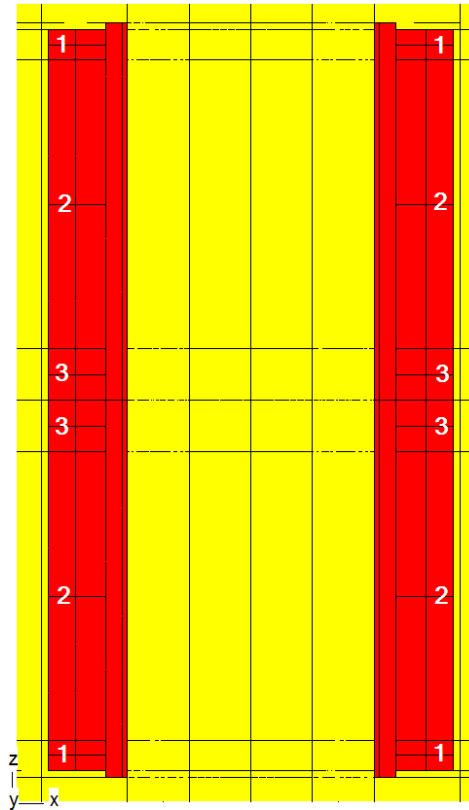


Fig. 21. "T1": Distribution of winding parts in the HV-winding

Although the current linkages are the same, the different cross sections of the individual axial winding blocks result in different current densities compared to the HV-winding with one axial block. The current densities of the different winding blocks are shown in Table 1.

Table 1: "T1": Current densities of the different winding blocks

	HV-winding with one axial block J_{peak} in A/m ²	HV-winding with six axial blocks as in Fig. 21 J_{peak} in A/m ²
Winding part 1		$-0,192 \cdot 10^6$
Winding part 2	$-0,187 \cdot 10^6$	$-0,191 \cdot 10^6$
Winding part 3		$-0,163 \cdot 10^6$

As shown in Figs. 22 to 24, the different current densities in the winding blocks on HV-side (same current linkage) result in different field distributions in the transformer, as well as in different radial fields in the centre of both windings. The axial field is nearly the same.

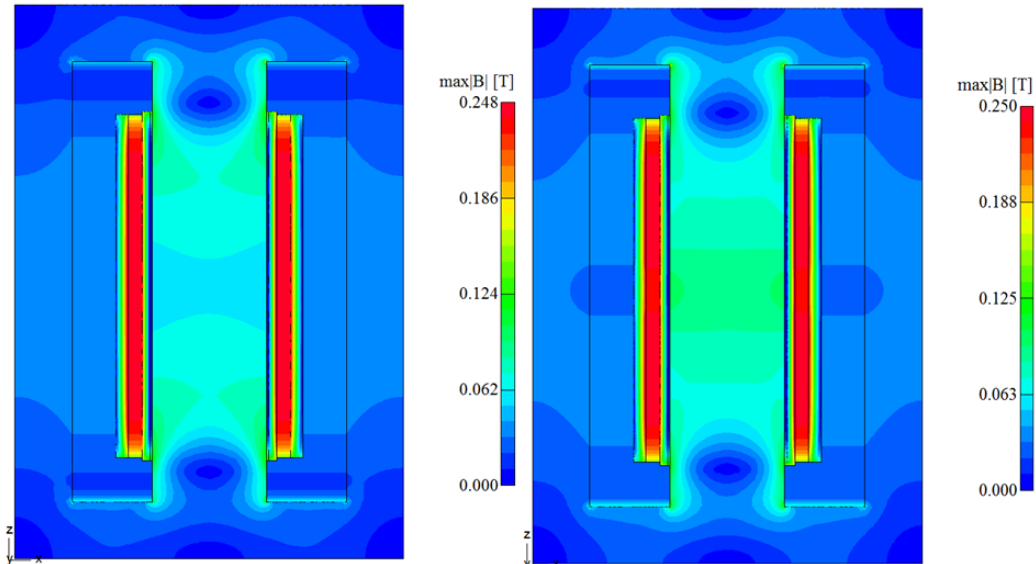


Fig. 22. “T1”: Field plots of the rotational symmetric 3D models, left: one block on HV-side, right: several blocks on HV-side

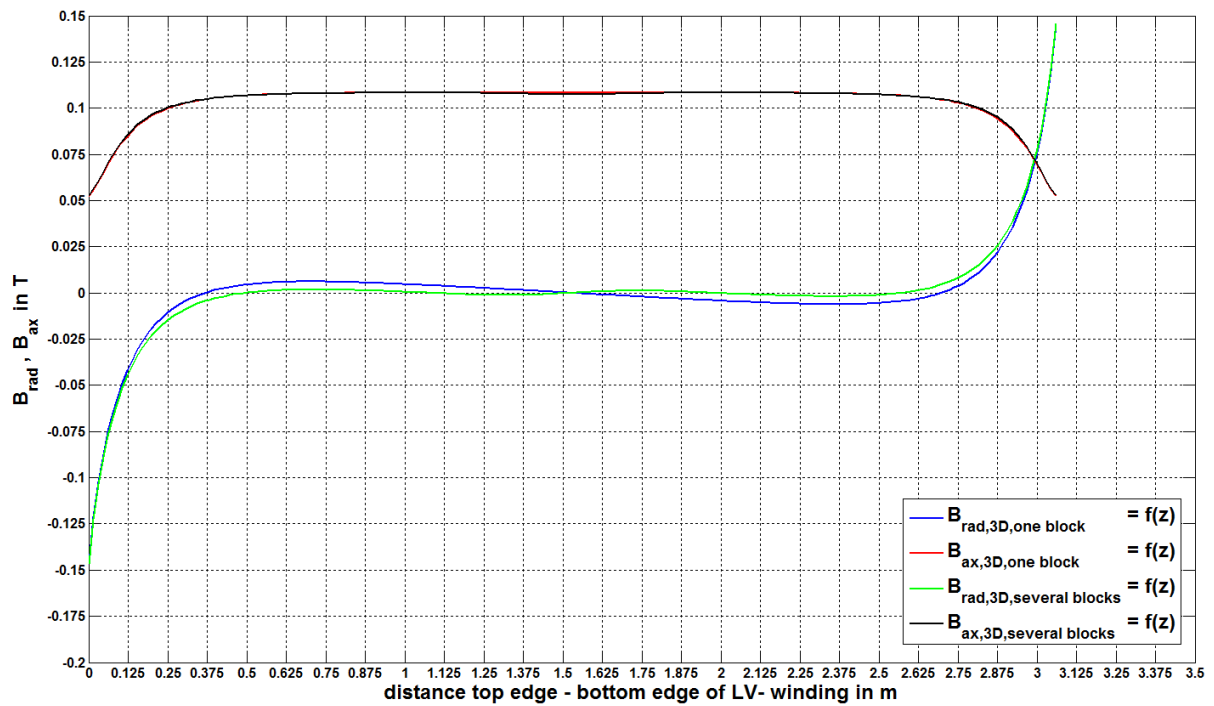


Fig. 23. “T1”: Comparison of radial and axial fields in LV-winding in z-direction ($x=0, y=r_{midLV}$)

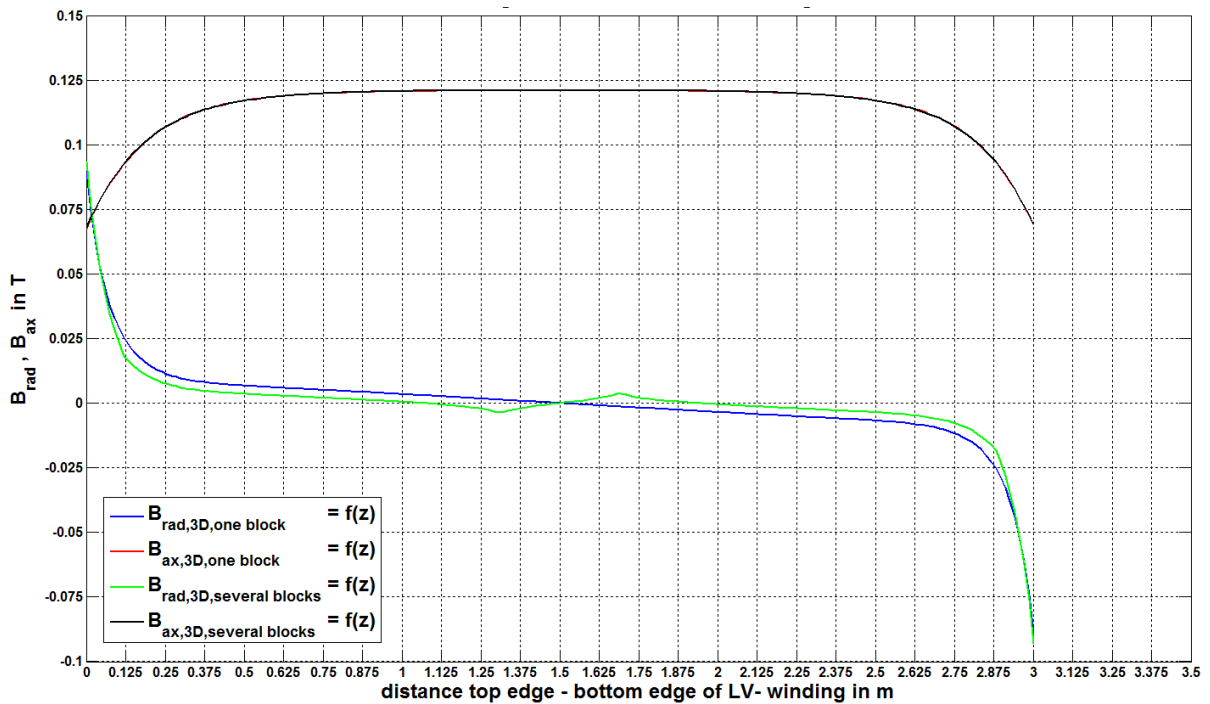


Fig. 24. “T1”: Comparison of radial and axial fields in HV-winding in z-direction ($x=0$, $y=r_{\text{midHV}}$)

3.2.2 Loss comparison

The losses due to the radial and axial fields are similar in dependence of the z-coordinate. Table 2 shows a comparison of different models to facilitate a statement if the method used in the 3D model is accurate enough, as well as to assess the different ways of implementing the windings into the model.

Ideally, the losses determined with the **second** (coarse 2D model) and the **third** model (equivalent 3D model) in Table 2 should be the same. On the basis of the calculations carried out for this purpose, just slight differences can be observed.

The differences in the I^2R losses of the HV winding (0,57 %) are due to the fact that the so called t-losses are not considered in the loss evaluation in the 3D model. These losses occur at the crossing between interleaved disks, since the turn which results in another disk is not a full turn.

The radial and axial losses of the two windings are also different in the 3D and 2D models. The first reason for this is that the evaluation methods are not the same. In the 2D model, the field is analysed in nine points per conductor, whereas in the 3D model only the midpoint of each conductor is taken into account. The second reason is that the t-losses are not considered in the 3D model.

This effect is stronger in the case of evaluating the radial losses at the top and the bottom end of each winding, than in the case of the axial losses which have their maximum in the winding centre.

Comparing the **detailed** and the **coarse** 2D models of Table 2 results in the conclusion that modelling every conductor leads in this case to slightly lower radial losses. The axial additional losses of the LV-winding are unaffected; those of the HV-winding are slightly lower.

Based on the comparison of the rotationally symmetric models with **one** as well as with **several axial winding blocks** in Table 2, a simplification of modelling disk windings by one cylindrical coil with one axial bloc should be avoided. As already expected from the field comparison results in Figs. 23 and 24, the radial additional losses are different, although the differences in the current densities at the upper and lower winding ends are small compared to the simplified winding model in Table 1.

Table 2: "T1": Loss comparison of different 2D and 3D models

Model		I^2R W	P_{rad} W	P_{ax} W	Total W
2D model – detailed modelling of windings as in Fig. 11	Winding LV	105724	2706	3716	
	Winding HV	124800	3289	11808	
	TOTAL	230524	5995	15524	252043
2D model – coarse modelling of windings as in Fig. 10	Winding LV	105724	2850	3717	
	Diff. to detailed 2D model in %	0,00	5,05	0,03	
	Winding HV	124800	3417	11966	
	Diff. to detailed 2D model in %	0,00	3,75	1,32	
TOTAL	230524	6267	15683	252474	
Rotationally symmetric 3D model – several axial winding blocks on HV-side	Winding LV	105724	3032	3707	
	Diff. to coarse 2D model in %	0,00	5,99	0,27	
	Diff. to detailed 2D model in %	0,00	10,74	0,24	
	Winding HV	125512	3613	12027	
	Diff. to coarse 2D model in %	0,57	5,41	0,50	
Diff. to detailed 2D model in %	0,57	8,96	1,82		
TOTAL	231236	6661	15734	253631	
Rotationally symmetric 3D model – One axial winding block on HV-side	Winding LV	105724	2909	3712	
	Diff. to coarse 2D model in %	0,00	5,77	0,36	
	Diff. to detailed 2D model in %	0,00	6,97	0,11	
	Winding HV	125512	4688	11955	
	Diff. to coarse 2D model in %	0,57	27,11	0,09	
Diff. to detailed 2D model in %	0,57	29,84	1,23		
TOTAL	231236	7597	7597	254499	

3.3 3D TrafoLoss-model

As described in subsection 2.2.2 (Figs. 13 and 14), the existing 3D FEM-model (created with the FEM tool TrafoLoss) for calculating the eddy current- and the specific losses in non-active steel parts cannot be used for computing the magnetic field in the windings. The 3D model of the transformer “Nanticoke” for evaluating the additional winding losses is shown in Fig. 25.

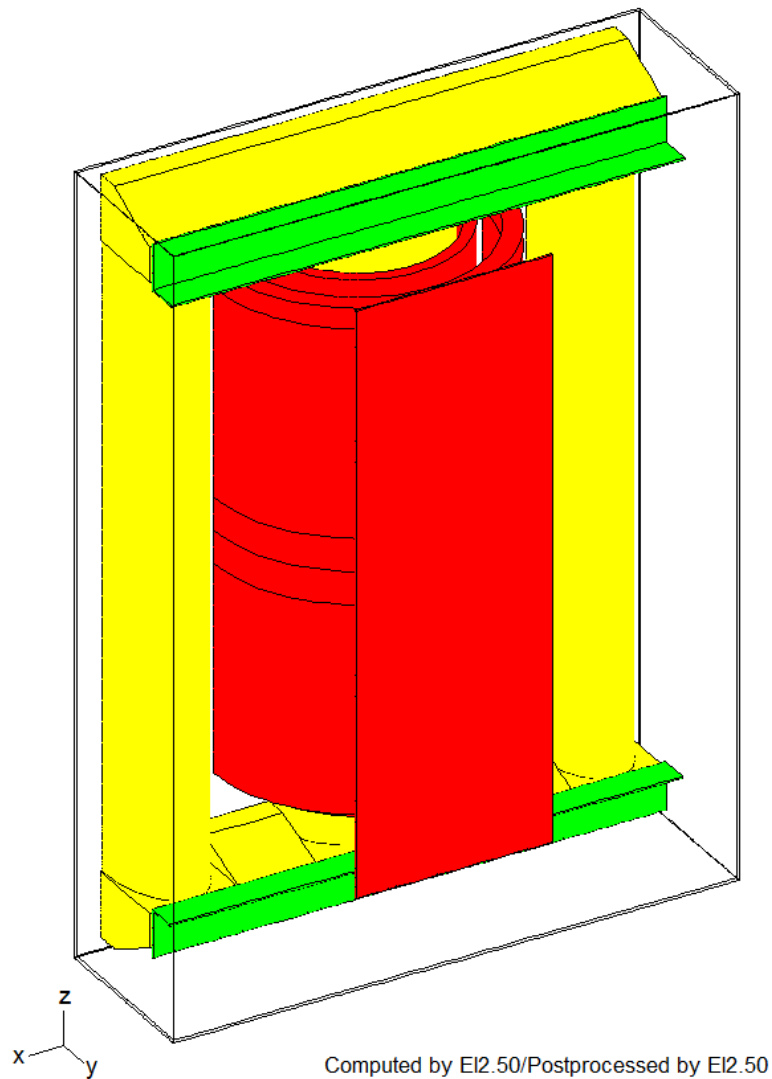


Fig. 25. “T1”: 3D TrafoLoss model for calculating the additional winding losses

As can be seen in Figs. 26 and 27, the finite element mesh at the level of the windings is not very fine. Investigations to the mesh accuracy and its effects on additional winding losses for T1 will be carried out in subsection 3.3.2.

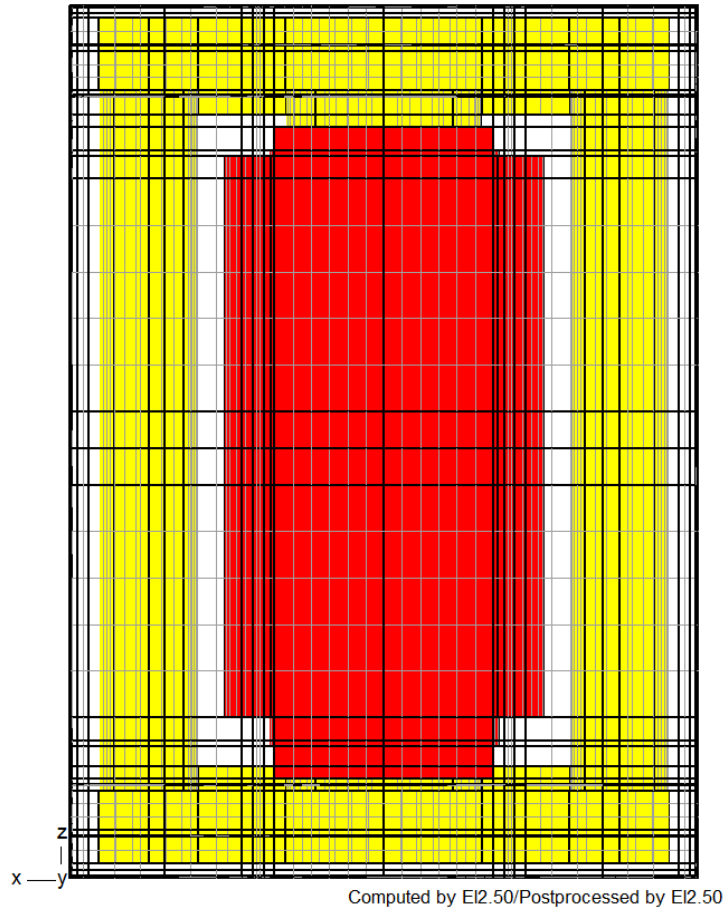


Fig. 26. "T1": Finite element mesh in x-z-plane (back view)

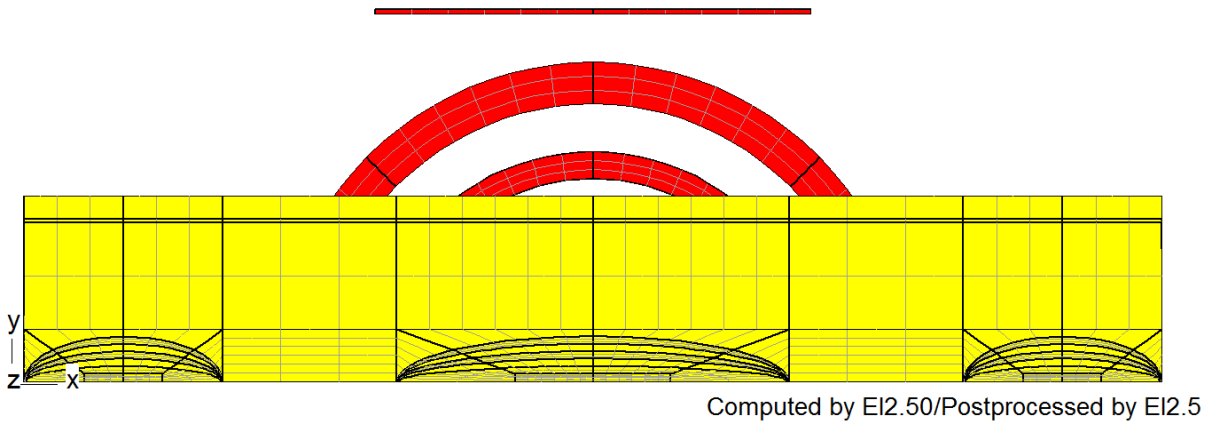


Fig. 27. "T1": Finite element mesh in x-y plane (top view)

In order to show how the magnetic flux densities differ in the two models (rotationally symmetric 3D model and true 3D model), the radial and axial magnetic fields in dependence of the z-coordinate will be compared in four points as in Fig. 28.

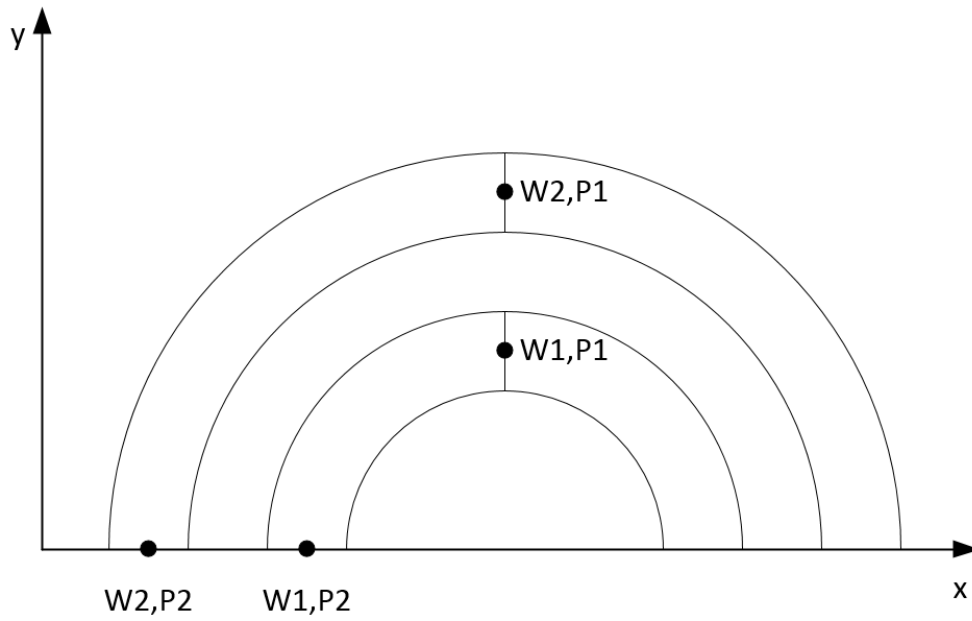


Fig. 28. Field comparison points

Comparing the radial and axial magnetic flux densities in winding 1, point 1 and winding 1, point 2 as in Fig. 29, demonstrates the azimuthal independence of the magnetic field in the rotationally symmetric 3D model. The results are similar for the comparison of winding 2, point 1 and winding 2, point 2.

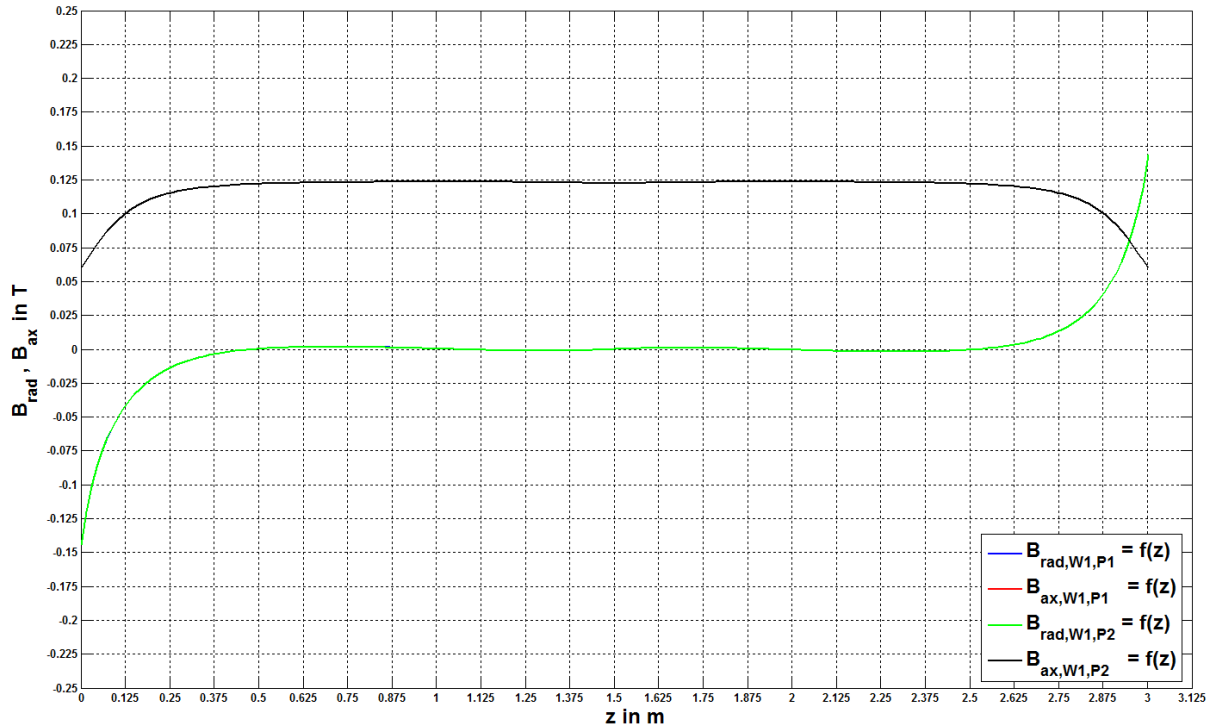


Fig. 29. "T1": Comparison of radial and axial fields in winding 1 in the rotational symmetric 3D model

Carrying out the same comparison with the 3D TrafoLoss model, leads to the results in Fig. 30. The differences in the magnetic field between point 1 and point 2 in winding 1 result from taking the three-dimensional geometry into account.

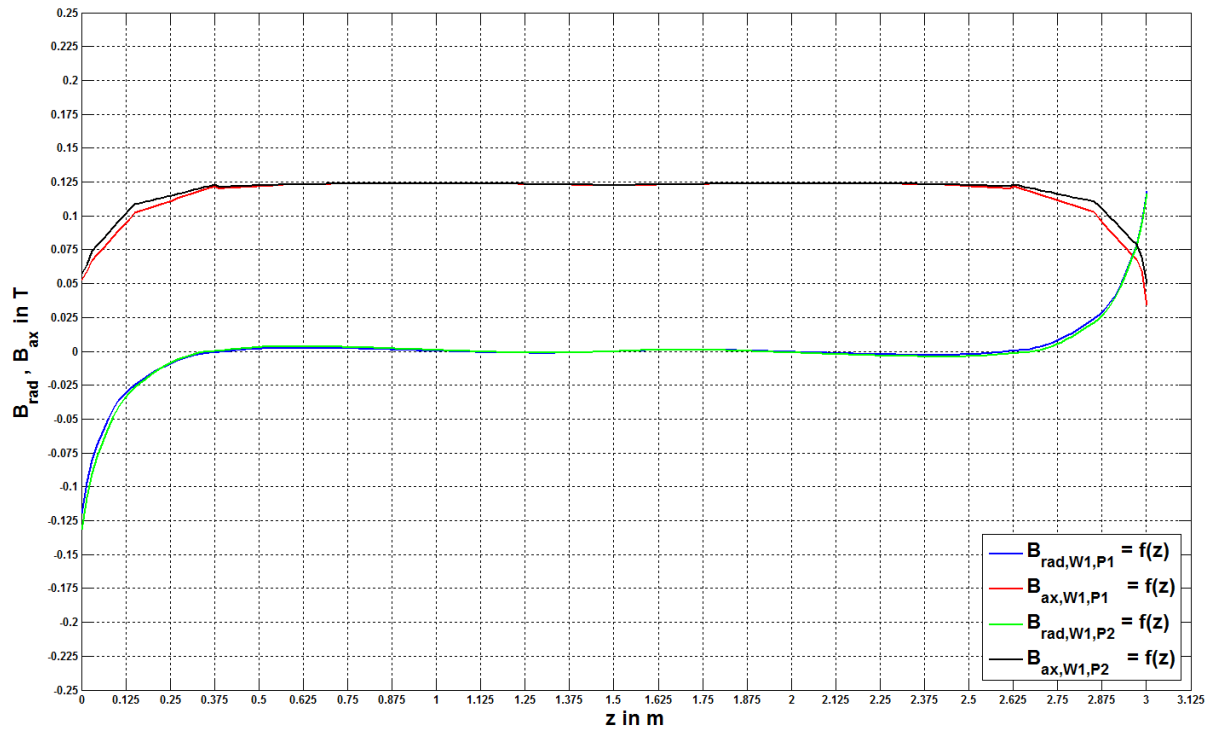


Fig. 30. "T1": Comparison of radial and axial fields in winding 1 in the 3D TrafoLoss-model

A comparison of radial and axial fields between the two models, carried out for every point defined in Fig. 28, is shown in Figs. 31 to 34. The differences between the field profiles in the 3D TrafoLoss-model and the rotationally symmetric 3D model occur mainly at the lower and upper winding ends, while the differences in the winding centre can be neglected.

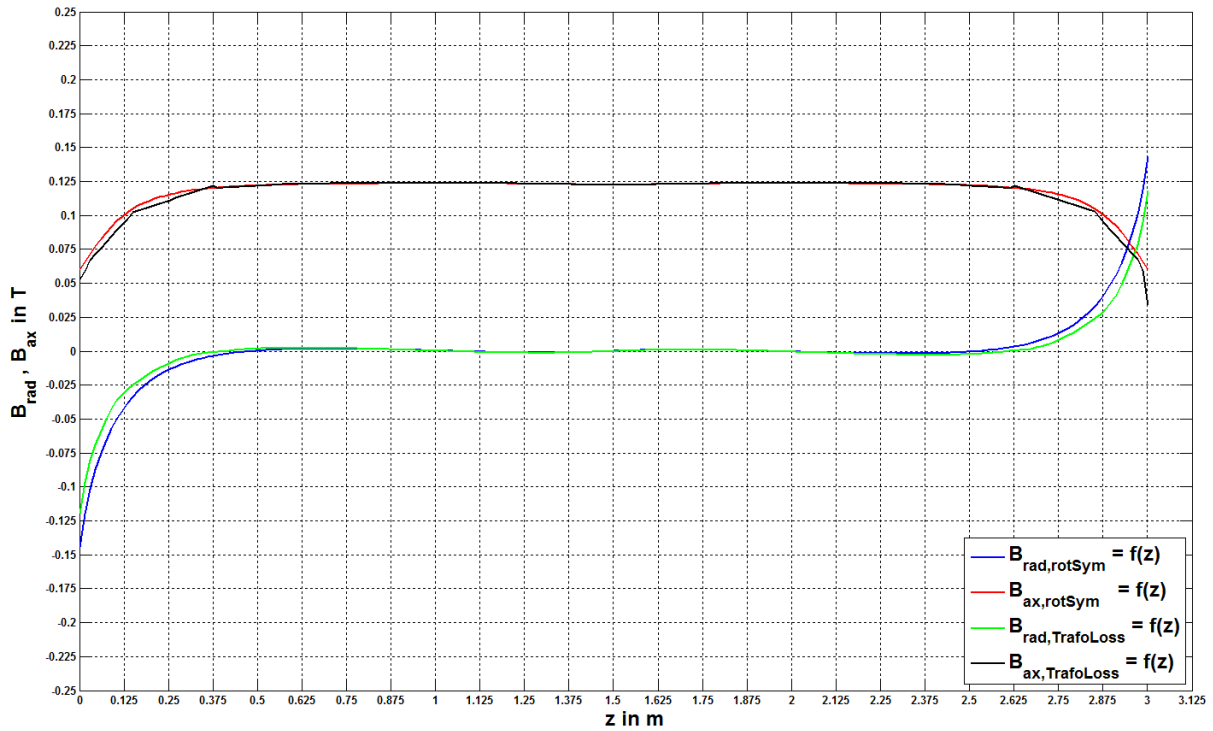


Fig. 31. "T1": Comparison of radial and axial fields in winding 1, point 1 between the rotationally symmetric and the TrafoLoss-model

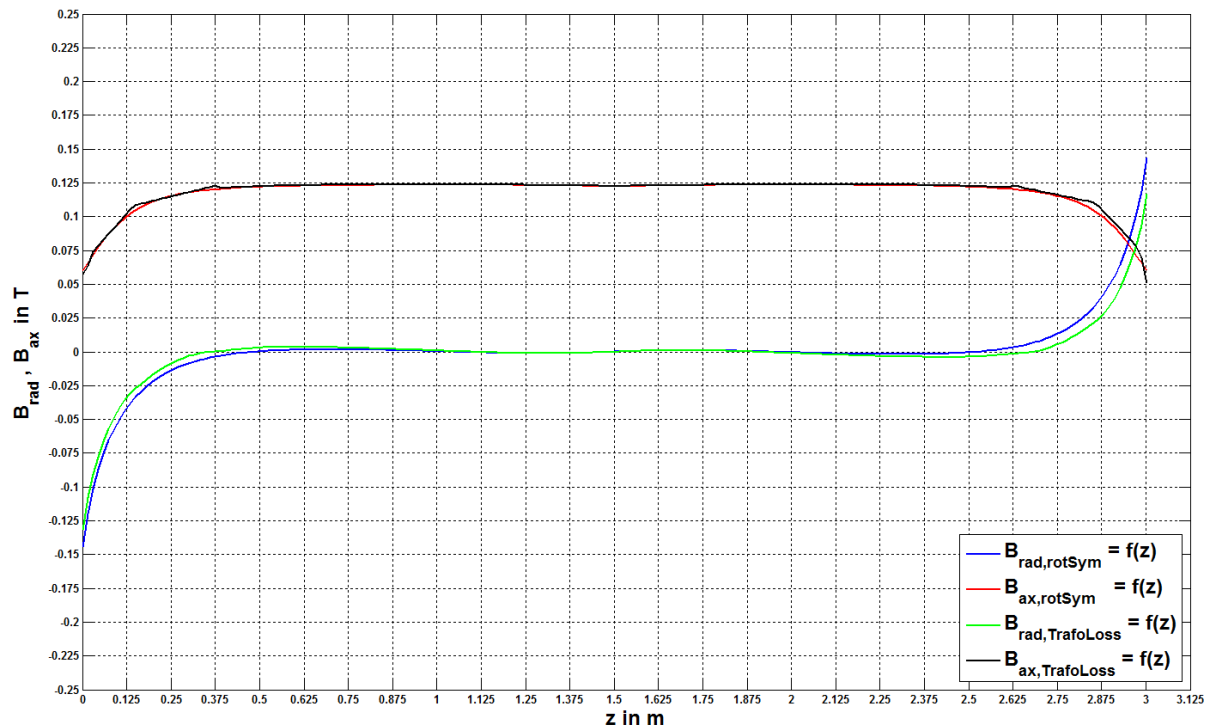


Fig. 32. "T1": Comparison of radial and axial fields in winding 1, point 2 between the rotationally symmetric and the TrafoLoss-model

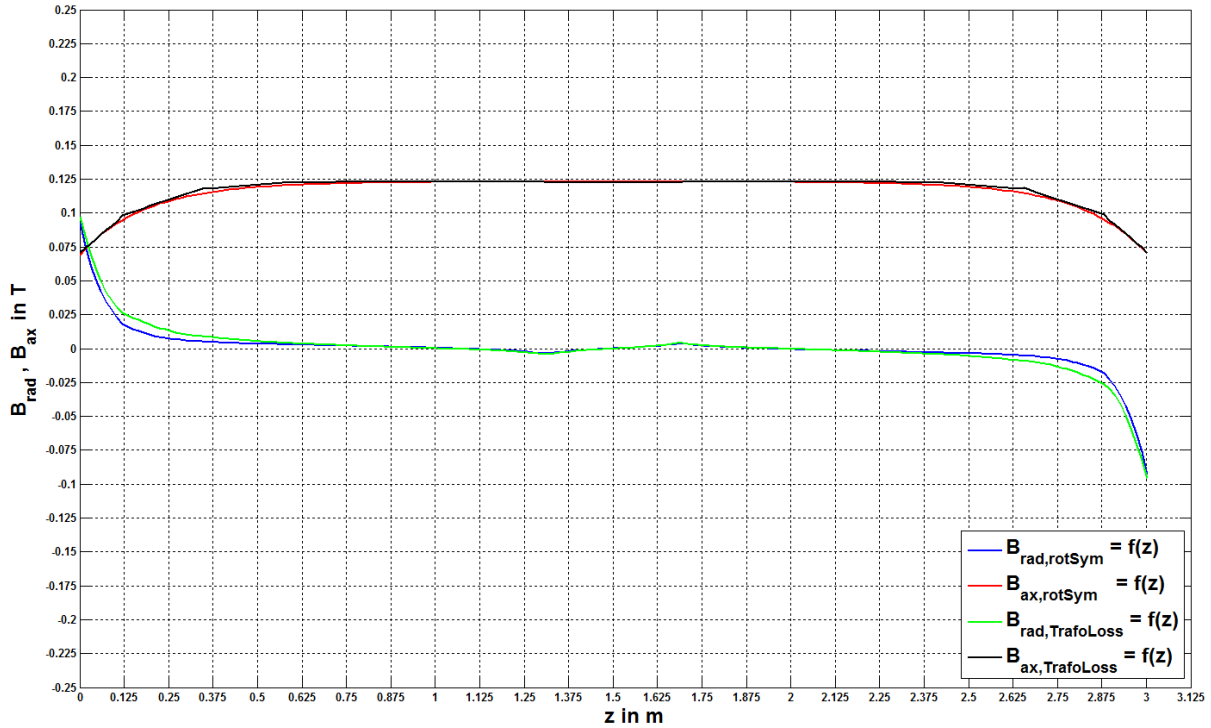


Fig. 33. "T1": Comparison of radial and axial fields in winding 2, point 1 between the rotationally symmetric and the TrafoLoss-model

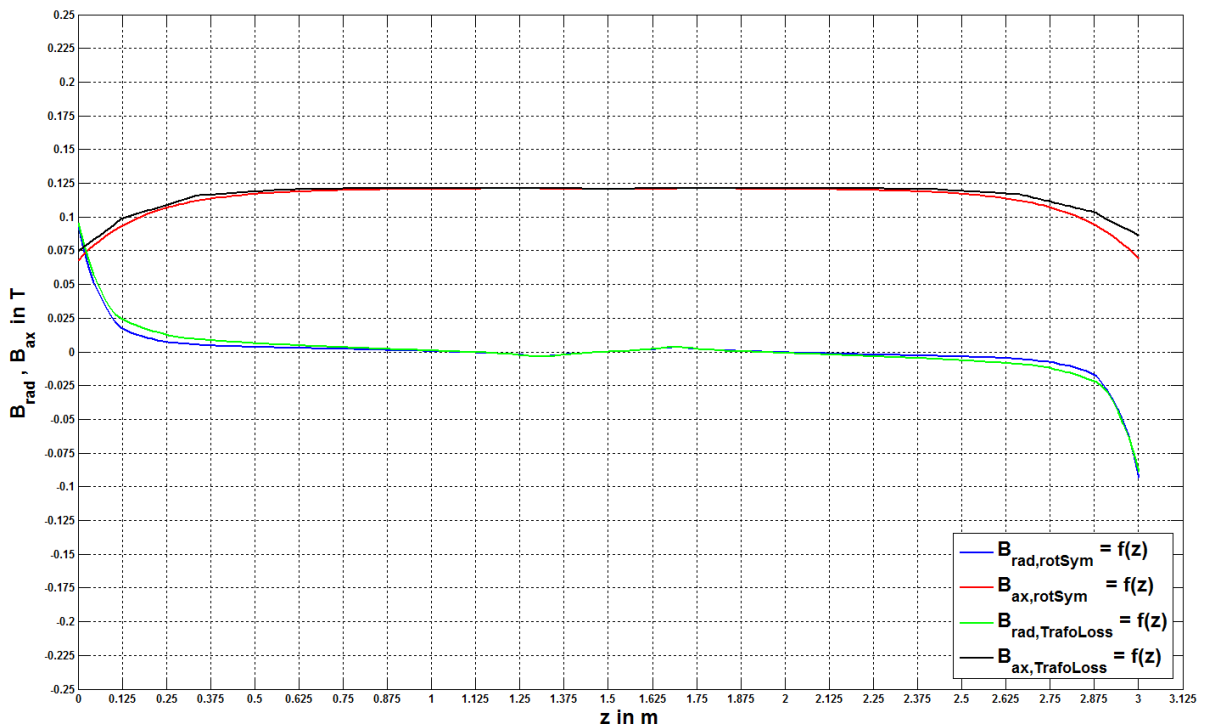


Fig. 34. "T1": Comparison of radial and axial fields in winding 2, point 2 between the rotational symmetric and the TrafoLoss-model

To show how the magnetic flux density changes in the azimuthal direction in the 3D TrafoLoss-model compared to the rotationally symmetric 3D model, the dependence of B_{rad} over the angle φ is evaluated along the lines indicated in Fig. 35. The result of analyzing B_{rad} in dependence of φ in winding 1 (LV-winding) and winding 2 (HV-winding) at $z=1.384$ m can be seen in Figs. 36 and 37.

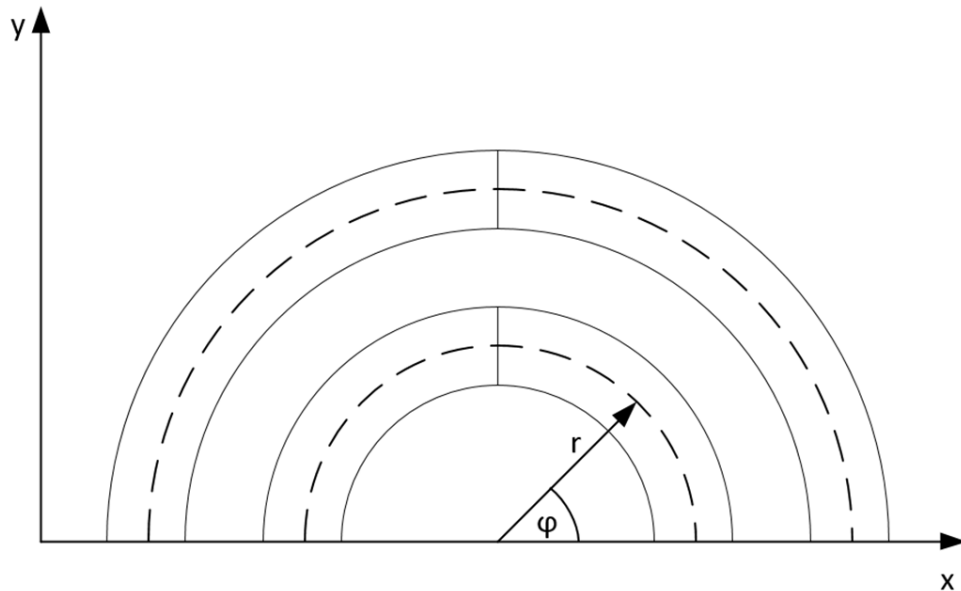


Fig. 35. Evaluation of the magnetic flux density in azimuthal direction

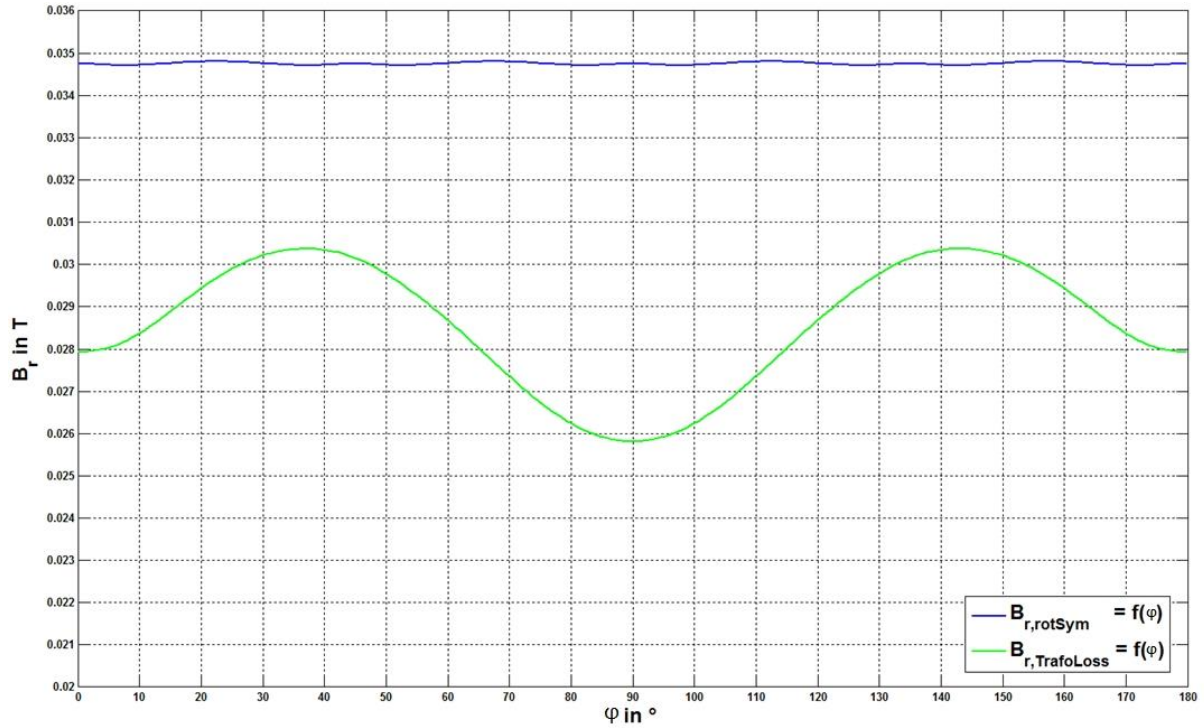


Fig. 36. "T1": B_{rad} as a function of φ evaluated in the centre of winding 1 at $z=1,384$ m (bottom edge of the upper winding block of winding 2)

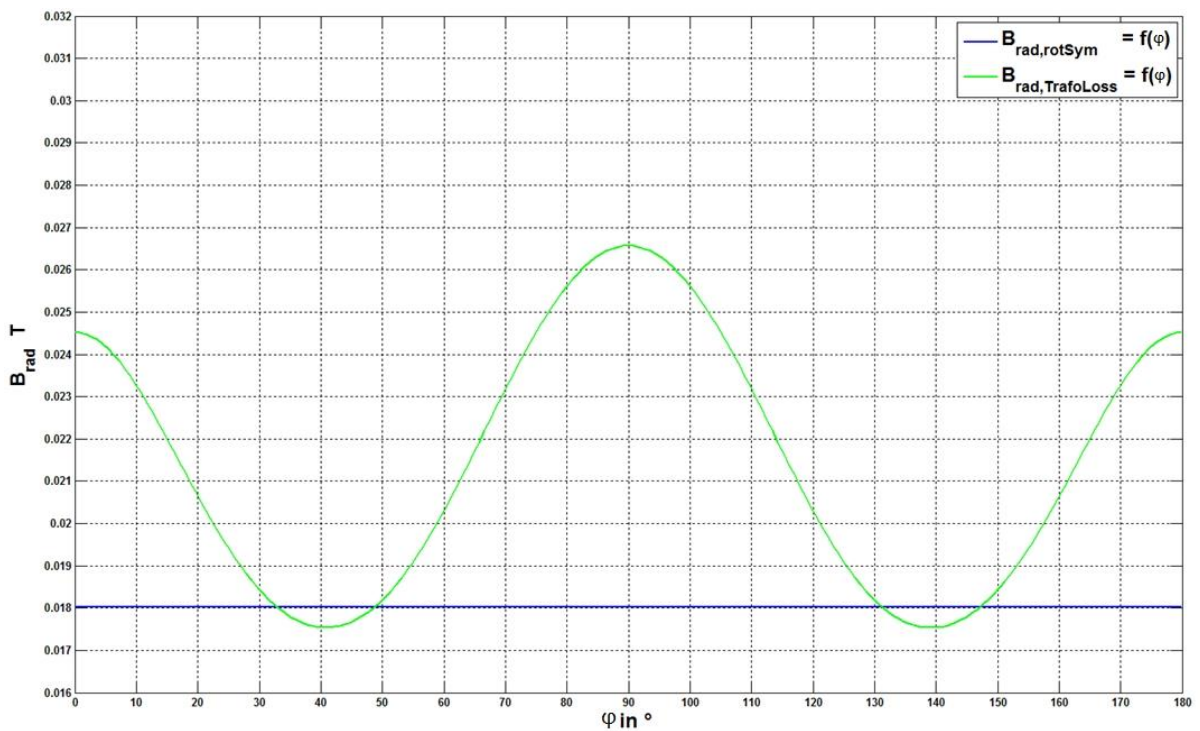


Fig. 37. "T1": B_{rad} as a function of φ evaluated in the centre of winding 2 at $z=1,384$ m (bottom edge of the upper winding block of winding 2)

The results in Figs. 36 and 37 justify the statement that B_{rad} does not change in azimuthal direction in the rotationally symmetric model (small changes are due to the approximation of the circular curves by parabolic ones). In the 3D TrafoLoss-model B_{rad} changes its value with the angle and the highest magnitude occurs at 90° .

Evaluating B_{rad} as a function of φ and as a function of z , leads to the 3D diagrams in Fig. 38 and Fig. 39. While the rotationally symmetric 3D model shows a dependence on z only, B_{rad} in the 3D TrafoLoss-model depends on the angle φ as well. Subtracting B_{rad} computed with the TrafoLoss-model from B_{rad} of the rotational symmetric model leads to Fig. 40. Since in most parts of this figure B_{rad} is positive, it can be assumed that the losses in winding 1 will show the same behaviour.

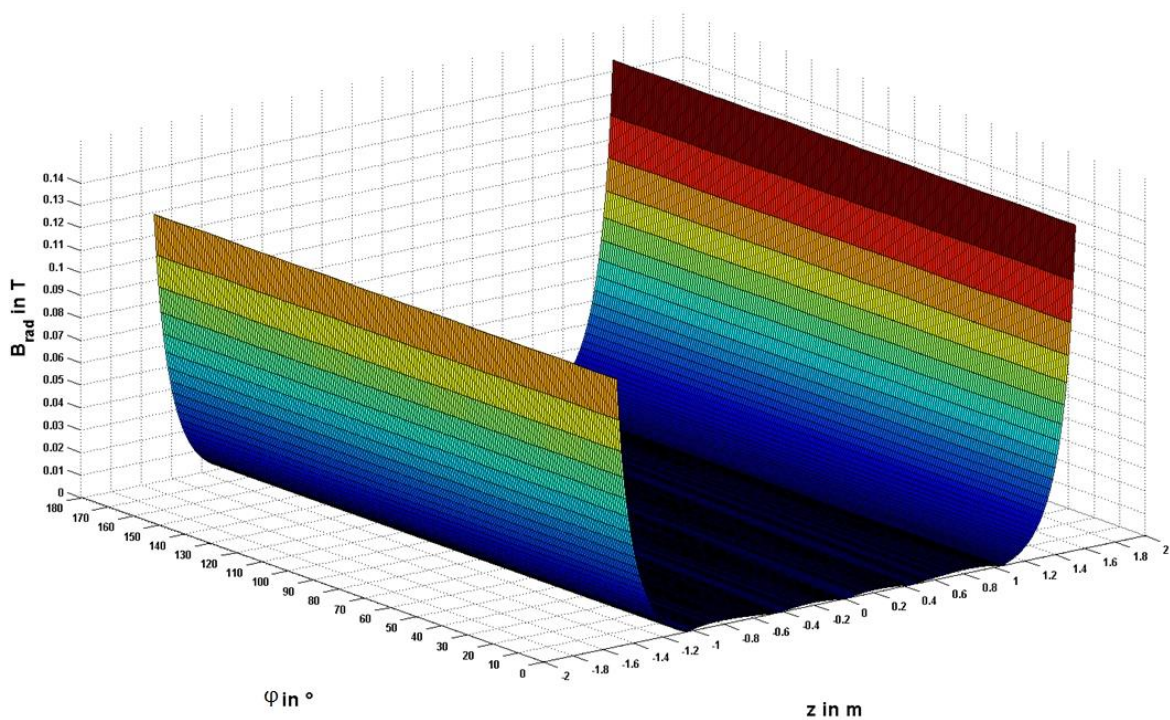


Fig. 38. "T1": B_{rad} as a function of φ and z evaluated in the centre of winding 1 in the rotationally symmetric 3D model

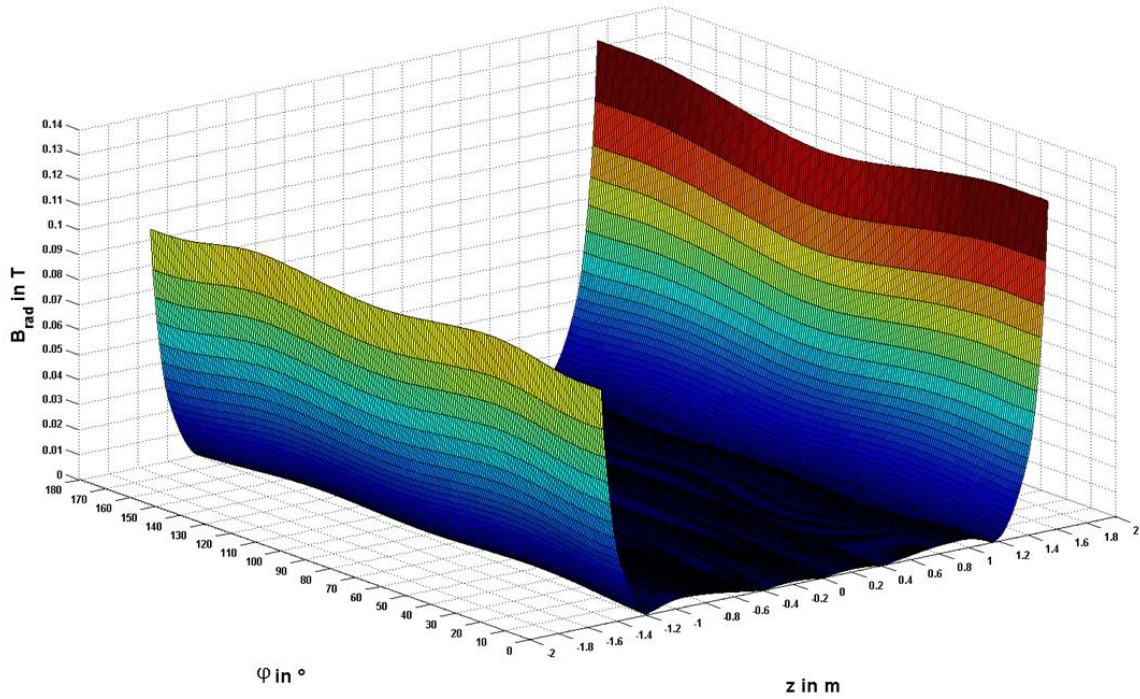


Fig. 39. "T1": B_{rad} as a function of φ and z evaluated in the centre of winding 1 in the 3D TrafoLoss-model

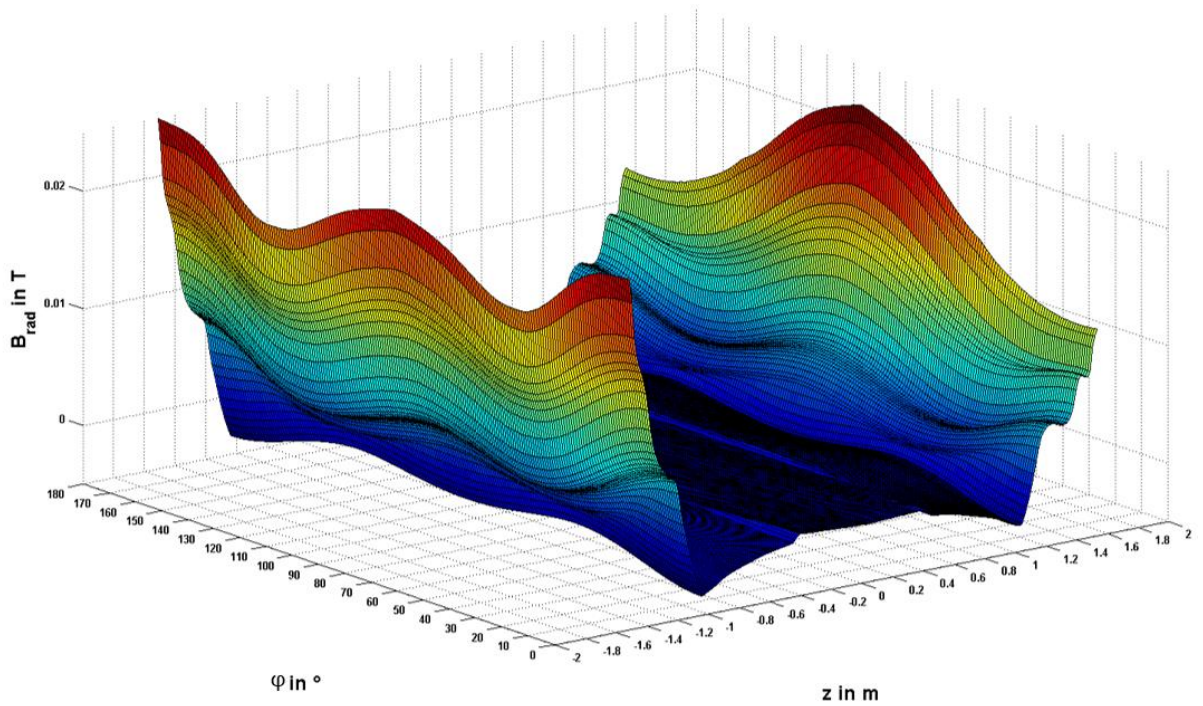


Fig. 40. "T1": Difference of B_{rad} from the rotationally symmetric model and B_{rad} from the TrafoLoss-model

3.3.1 Loss comparison

A comparison of the losses resulting from the 3D TrafoLoss-model with those from the rotationally symmetric 3D model (Table 3) shows a change in radial additional losses, while the axial additional losses are nearly the same. Whereas the radial losses in the high-voltage winding increase by approx. 14%, the losses in the low-voltage winding drop by a substantial 47.75 %. This confirms the findings in Fig. 40, that the difference between the losses of the rotationally symmetric model and the 3D TrafoLoss-model is positive.

Table 3: "T1": Loss comparison of the 3D TrafoLoss-model

Model		I ² R W	P _{rad} W	P _{ax} W	Total W
Rotational symmetric 3D model – several axial winding blocks on HV-side	Winding LV	105724	3032	3707	
	Diff. to coarse 2D model in %	0,00	5,99	0,27	
	Diff. to detailed 2D model in %	0,00	10,74	0,24	
	Winding HV	125512	3613	12027	
	Diff. to coarse 2D model in %	0,57	5,41	0,50	
	Diff. to detailed 2D model in %	0,57	8,96	1,82	
	TOTAL	231236	6661	15734	253631
3D TrafoLoss-model – several axial winding blocks on HV-side, FE mesh according Fig. 26 and Fig. 27.	Winding LV	105724	2052	3698	
	Diff. to rot. sym. 3D model in %	0,00	47,75	0,24	
	Winding HV	125512	4108	12190	
	Diff. to rot. sym. 3D model in %	0,00	13,70	1,36	
	TOTAL	231236	6231	15889	253356

3.3.2 Influence of mesh accuracy on additional losses

Compared to the number of finite elements along windings in axial direction in the 2D model in Fig. 41, the mesh in the 3D TrafoLoss-model in Figs. 26 and 27 is not that fine. In the 2D model it is usual to use at least one finite element per conductor in axial direction. In radial direction the high number finite elements results from unequal numbers of turns in the different disks of the HV-winding.

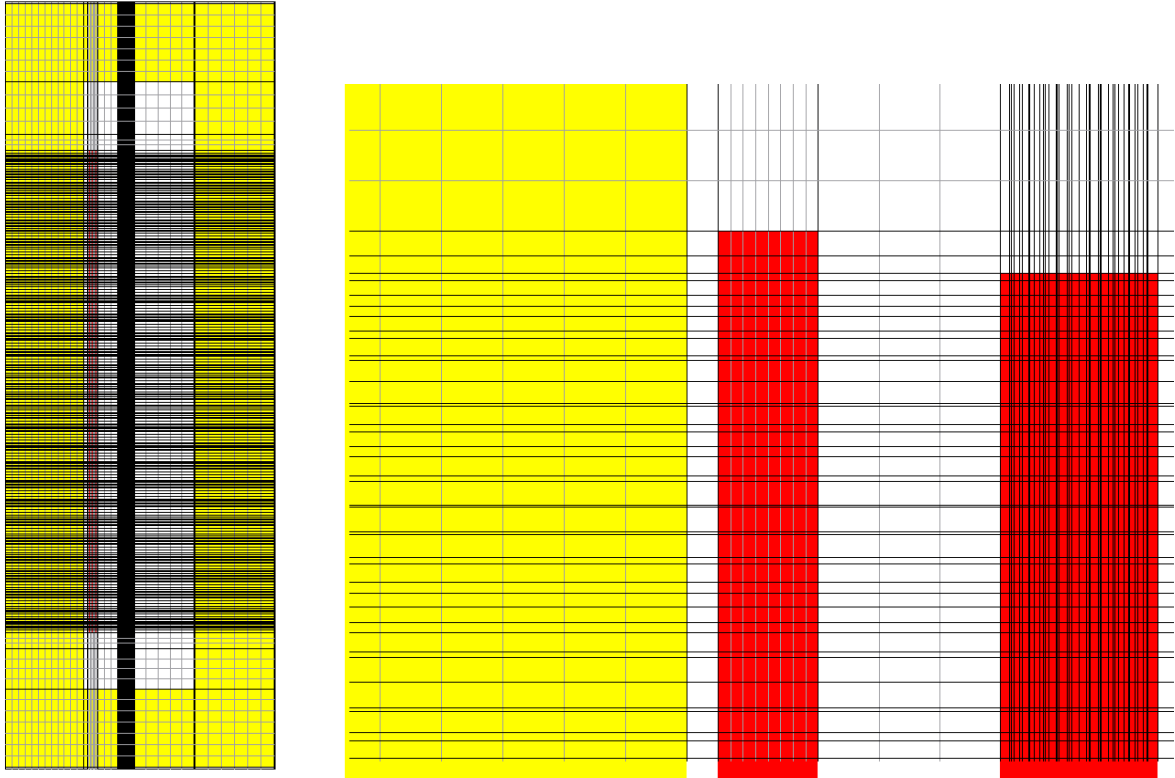


Fig. 41. "T1": Finite element mesh in the coarse 2D model

To determine the influence of a finer finite element mesh, two further models have been investigated. The Figs. 42 and 43 show a model with a finer distribution of finite elements in axial direction. The number of finite elements (180) depends thereby on the number of axial conductors in the LV-winding (more LV-conductors than axial disks in the HV-winding). The effects of a higher number of radial finite elements will be considered in another model as in Figs. 44 and 45.

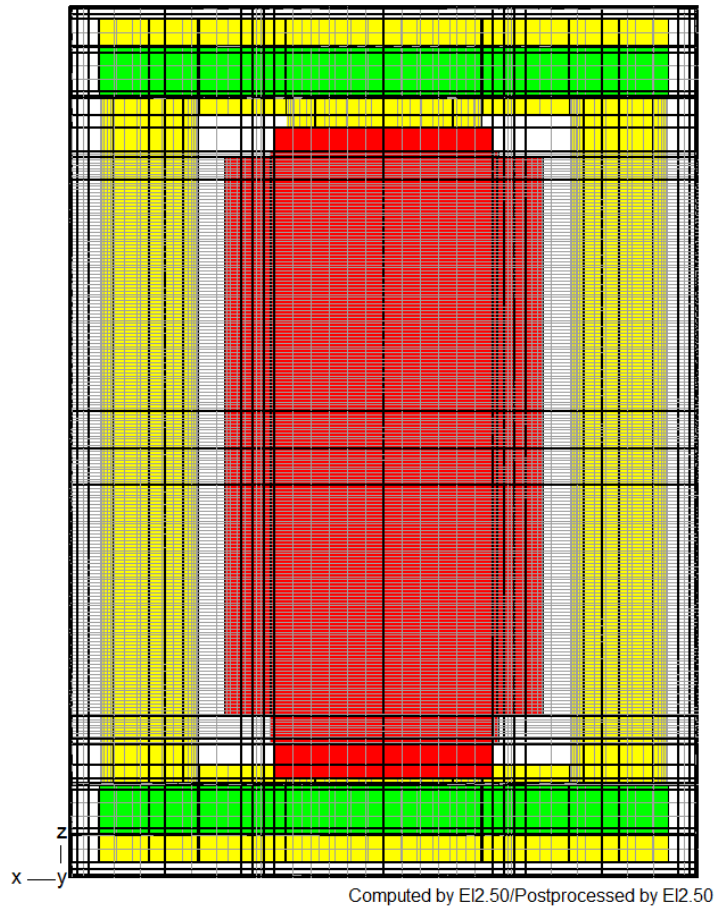


Fig. 42. "T1": Finite element mesh in x-z-plane with finer axial FE-division

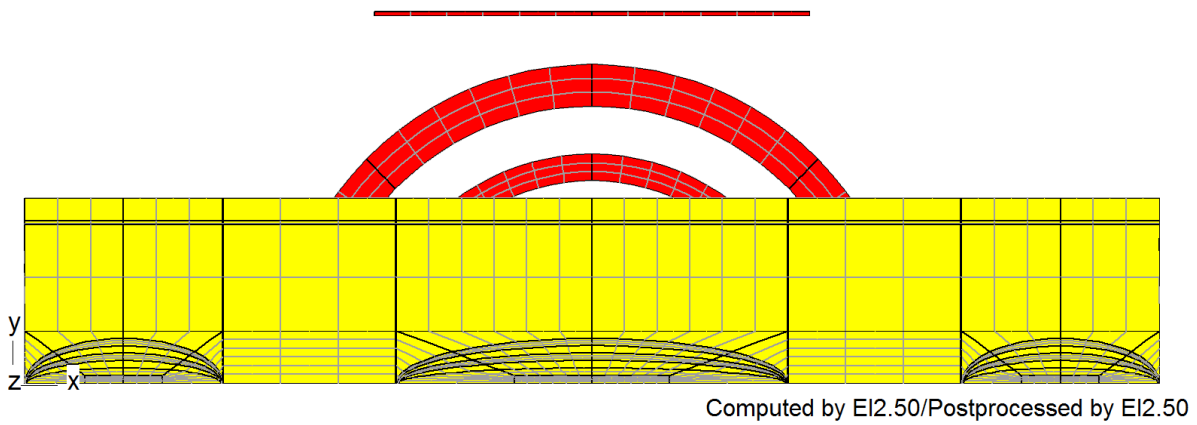


Fig. 43. "T1": Finite element mesh in x-y-plane with finer axial FE-division

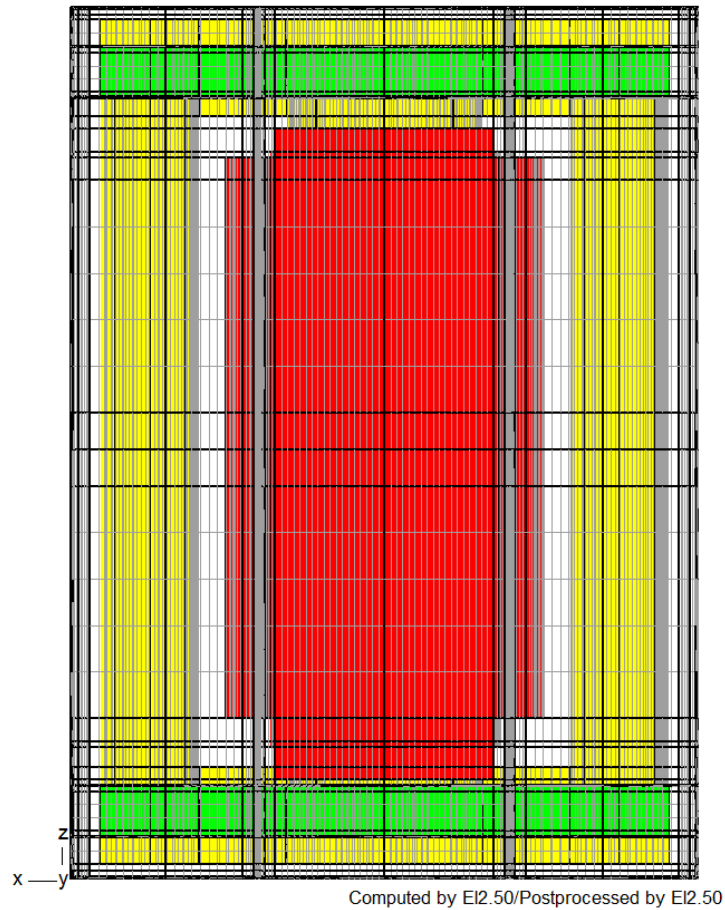


Fig. 44. "T1": Finite element mesh in x-z-plane with finer radial and axial FE-division

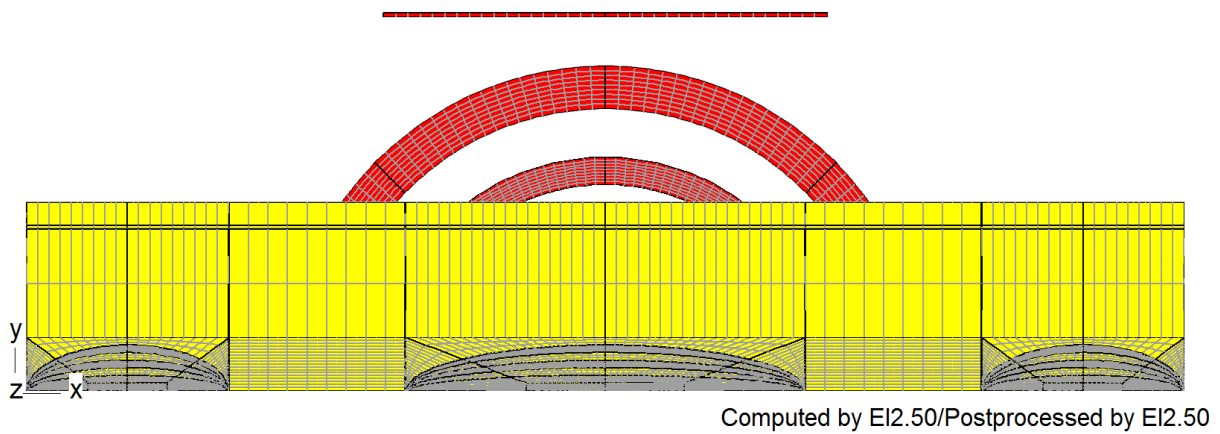


Fig. 45: "T1": Finite element mesh in x-y-plane with finer radial and axial FE-division

Comparing the losses of the different models in Table 4 shows that a finer division into finite elements has a negligibly small effect on the additional losses. Only the deviation of radial additional losses in the HV-winding of the second model in Table 4 is larger than 1 %. However, this is not significant because the deviation of the more precise model (third model in Table 4) is lower than 1 %.

Table 4: “T1”: Influences of FE-distribution on the additional losses

Model		I ² R W	P _{rad} W	P _{ax} W	Total W
3D TrafoLoss model – standard FE mesh of Fig. 26 and Fig. 27.	Winding LV	105724	2052	3698	
	-	-	-	-	
	Winding HV	125512	4108	12190	
	-	-	-	-	
	TOTAL	231236	6231	15889	253356
3D TrafoLoss model - finer axial FE- division of. Fig. 42 and Fig. 43	Winding LV	105724	2041	3698	
	Diff. to standard 3D model in %	0,00	0,54	0,00	
	Winding HV	125512	4057	12187	
	Diff. to standard 3D model in %	0,00	1,24	0,02	
	TOTAL	231236	6170	15886	253292
3D TrafoLoss model - finer radial and axial FE- division of Fig. 44 and Fig. 45	Winding LV	105724	2060	3697	
	Diff. to standard 3D model in %	0,00	0,39	0,03	
	Winding HV	125512	4144	12188	
	Diff. to standard 3D model in %	0,00	0,88	0,02	
	TOTAL	231236	6273	15886	253395

4 Additional losses of various core types

4.1 One-limb core transformer “T1”

4.1.1 Technical data

The technical data of the one-limb core transformer T1 can be found in section 3.1.

4.1.2 3D TrafoLoss-model

The 3D TrafoLoss-model has been explained in section 0.

4.1.3 Loss comparison

A detailed comparison of the additional losses of the different 2D and 3D FEM-models (rotational symmetric Model and TrafoLoss-model with the finite element mesh in Figs. 26 and 27) is shown in the Tables 2 and 3.

4.1.4 Effects of eddy currents in non-active steel parts

Beside investigations of a finer FE-division of the problem domain, the effects of eddy currents in steel parts should also be taken into account. While the 2D model is based on a magnetic field calculation with no eddy current domains, the 3D problem is described with the $\mathbf{T}, \Phi - \Phi$ method, where also eddy currents in non-active steel parts are considered.

In the 3D TrafoLoss-model for calculating the additional winding losses, eddy currents are considered in the clamping structure and in the tank. Table 5 shows a comparison of the additional losses calculated with the standard model (with eddy current regions) and a model without eddy current domains.

Table 5: “T1”: Comparison of eddy current free model with the standard 3D TrafoLoss model

Model		I^2R W	P_{rad} W	P_{ax} W	Total W
3D TrafoLoss model – standard FE mesh of. Fig. 26 and Fig. 27.	Winding LV	105724	2052	3698	
	-	-	-	-	
	Winding HV	125512	4108	12190	
	-	-	-	-	
	TOTAL	231236	6231	15889	253356
3D TrafoLoss model – standard FE mesh – without eddy current region	Winding LV	105724	2005	3701	
	Diff. to standard 3D model in %	0,00	2,29	0,08	
	Winding HV	125512	4185	12209	
	Diff. to standard 3D model in %	0,00	1,87	0,15	
	TOTAL	231236	6267	15911	253414

Taking account of the eddy currents in the clamping structure and the tank affects the radial additional losses only. The explanation is that the axial additional losses occur mainly in the winding centre, in sufficient distance to the next eddy current region. The radial additional losses, which mainly occur at the winding ends, seem to be slightly influenced by the eddy currents flowing in the clamping structure. The evaluation of which variant has to be used for the calculations should therefore be carried out on the basis of the different computation times.

4.1.5 Computation times

While the computation time of 2D FEM-models is usually small, it is significant when solving 3D FEM-models of large power transformers. Table 6 shows a summary of computation times of various 3D TrafoLoss-models.

Table 6: “T1”: Computation time of different 3D TrafoLoss-models

No.	Model	No. of equations	Computation time hh:mm:ss
1	3D TrafoLoss-model - standard FE mesh of Fig. 26 and Fig. 27.	928837	00:36:15
2	3D TrafoLoss-model - standard FE mesh – without eddy current region	661684	00:04:37
3	3D TrafoLoss-model - finer axial FE-division of. Fig. 42 and Fig. 43	2930417	02:46:54
4	3D TrafoLoss-model - finer radial and axial FE-division of Fig. 44 and Fig. 45	4821777	09:21:46

Due to the fact that increasing the number of finite elements in the 3D TrafoLoss-model has a negligible effect on the calculated additional losses (see subsection 4.1.4) the decision which model should be used for carrying out this calculation can be made using the calculation times in Table 6.

Using Model 3 or Model 4 in Table 6 has no effect on the results and the number of equations as well as the calculation time is very high. These models are not necessary for further calculations.

Comparing the standard TrafoLoss-model with the same model without computed eddy currents in non-active steel parts shows that the latter one needs more than seven times lower computation time. Hence, this model (standard finite element mesh without eddy current domains) is feasible for further calculations regarding one-limb core transformers.

4.2 Two-limb core transformer “T2”

4.2.1 Technical data

The two-limb core transformer “T2” is designed for operation with a “Static Var Compensator” (SVC) with a nominal power of 100 MVA and an operational voltage of $735/\sqrt{3}$ kV / 26 kV. In combination with the vector group YNd5, this configuration results in currents of 235,7A on the HV-side and 3846,2 A on the LV-side. The operational frequency is 60 Hz. The low voltage winding is implemented as a cylindrical winding with one layer. Constructed with a drilled conductor with 79 strands where one strand has dimensions of 7,7x1,05 mm. The high voltage winding consists of several disks with a blind conductor for increased distances between the conductors due to voltage withstand reasons. These disks are manufactured with two different conductors.

4.2.2 3D TrafoLoss-model

Generating a 3D TrafoLoss-model from the transformer described in subsection 4.2.1 leads to the FEM-model in Fig. 46, with the finite element mesh as in Figs. 47 and 48. The half model consists of a tank, a simplified two-limb core (to get the rounded structure of the finite element mesh), a clamping structure with yoke shielding and a simplified tank shielding.

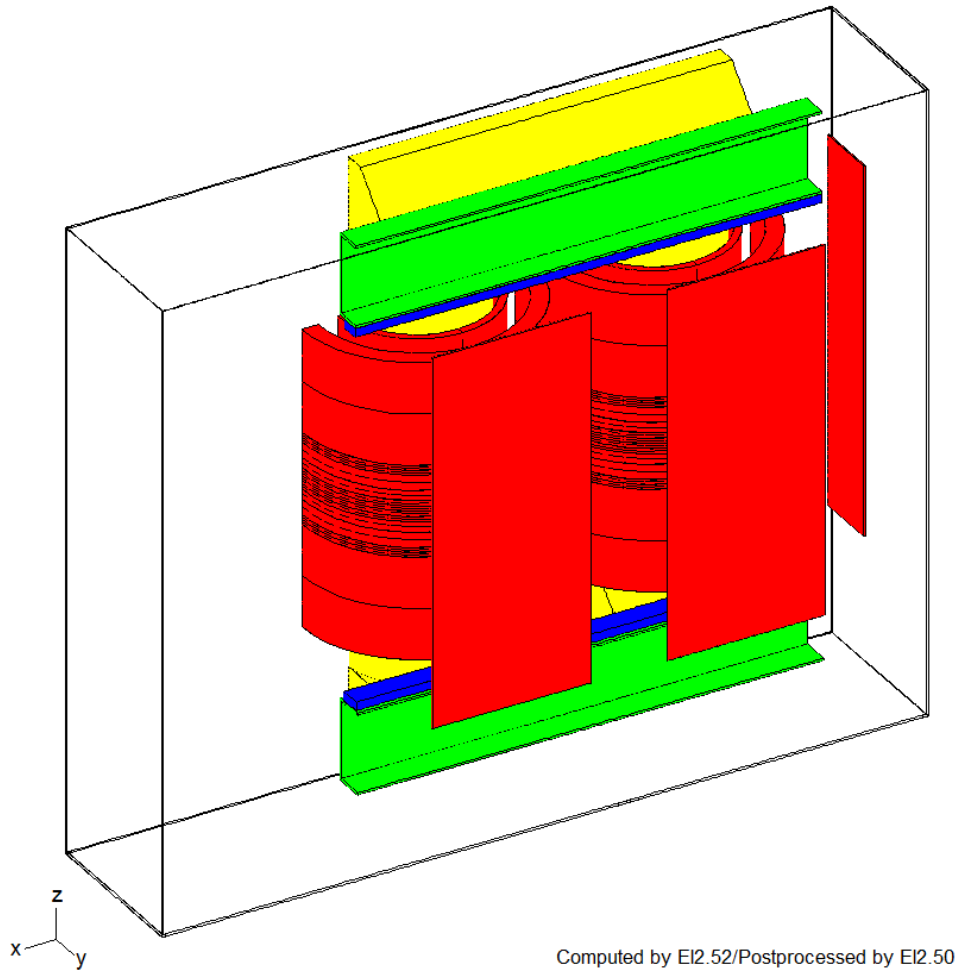


Fig. 46. "T2": 3D TrafoLoss-model

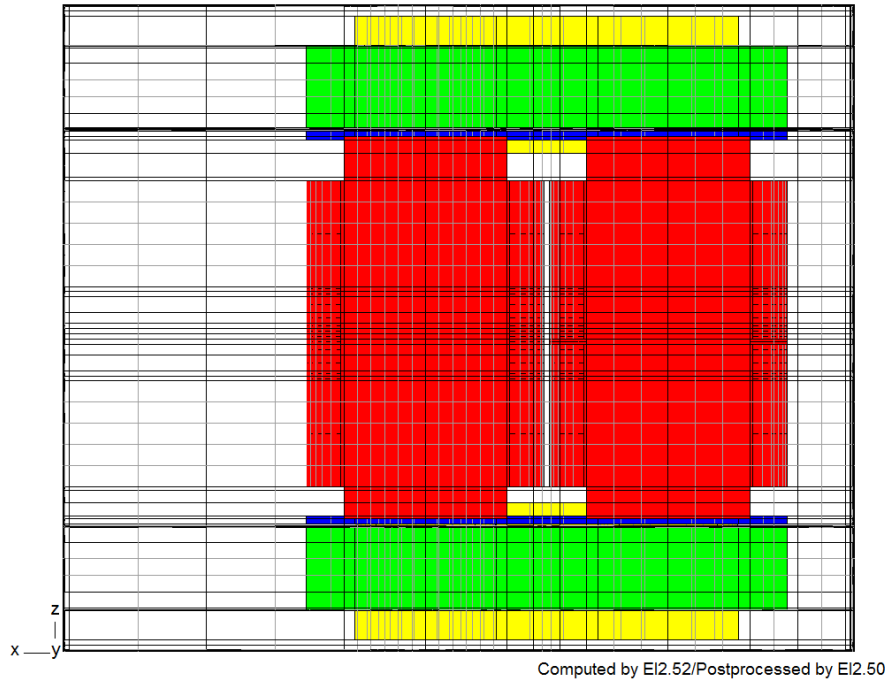


Fig. 47. "T2": Finite element mesh in x-z-plane

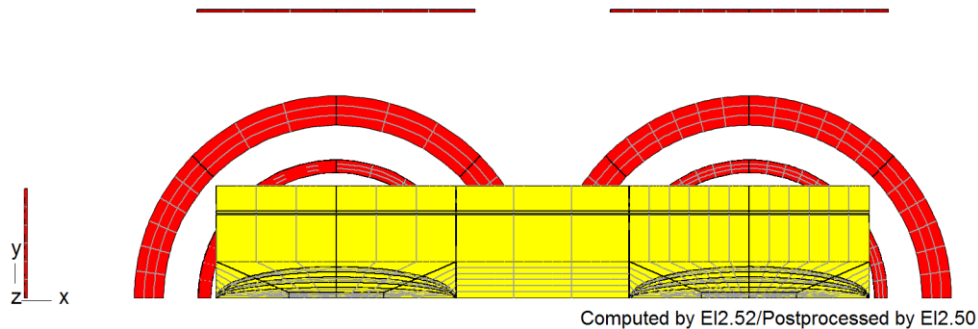


Fig. 48. "T2": Finite element mesh in x-y-plane

4.2.3 Loss comparison

A comparison of the losses of the two different 2D models with the 3D TrafoLoss-model can be found in Table 7. To assess the results from the 3D model, a comparison with the corresponding coarse 2D model shows that the radial additional losses in the LV-winding are much smaller (by 20,91 %), while the radial losses from the HV-winding are increasing. An evaluation of every limb shows that the behaviour is the same and that the increased distance to the tank wall on the left side has practically no effect. The differences in the axial additional losses are negligibly small. As already explained in subsection 3.2.2, the difference in the I^2R -losses of the HV-winding results from the t-losses in disk windings.

Table 7: "T2": Loss comparison of 2D models and 3D TrafoLoss-model

Model		I ² R W	P _{rad} W	P _{ax} W	Total W
2D model – detailed modelling of windings as in Fig. 11	Winding LV	99760	4494	911	
	Winding HV	114777	3882	11568	
	TOTAL	214537	8376	12479	235392
2D model – coarse modelling of windings as in Fig. 10	Winding LV	99760	4695	916	
	Diff. to detailed 2D model in %	0,00	4,28	0,55	
	Winding HV	114777	4183	11693	
	Diff. to detailed 2D model in %	0,00	7,20	1,07	
	TOTAL	214537	8878	12609	236024
3D TrafoLoss- model – Standard FE mesh as in Fig. 47 and Fig. 48.	Winding LV left	49880	1944	450	
	Winding LV right	49880	1939	450	
	Winding LV	99760	3883	899	
	Diff. to coarse 2D model in %	0,00	20,91	1,84	
	Diff. to detailed 2D model in %	0,00	15,73	1,28	
	Winding HV left	57491	2182	5921	
	Winding HV right	57491	2163	5924	
	Winding HV	114981	4345	11844	
	TOTAL	214741	8228	12744	235714

4.2.4 Effects of eddy currents in non-active steel parts

To evaluate the influence of eddy currents in the clamping structure and tank components, Table 8 shows the results of a model with eddy current domains and a model without these domains.

In this case again, the effects are negligible. The deviations in radial and axial losses are smaller than 1 %.

Table 8: “T2”: Comparison of eddy current free model with the standard 3D TrafoLoss model

Model		I^2R	P_{rad}	P_{ax}	Total
		W	W	W	W
3D TrafoLoss-model – Standard FE mesh as in Fig. 47 and Fig. 48.	Winding LV left	49880	1944	450	
	Winding LV right	49880	1939	450	
	Winding LV	99760	3883	899	
	-	-	-	-	
	Winding HV left	57491	2182	5921	
	Winding HV right	57491	2163	5924	
	Winding HV	114981	4345	11844	
	-	-	-	-	
	TOTAL	214741	8228	12744	235714
3D TrafoLoss-model – standard FE mesh – without eddy current region	Winding LV left	49880	1939	450	
	Winding LV right	49880	1931	450	
	Winding LV	99760	3870	900	
	Diff. to standard 3D model in %	0,00	0,33	0,11	
	Winding HV left	57491	2184	5922	
	Winding HV right	57491	2165	5926	
	Winding HV	114981	4349	11848	
	Diff. to standard 3D model in %	0,00	0,09	0,03	
	TOTAL	231236	6267	15911	253414

4.2.5 Computation times

A comparison of the two different 3D models shown in Table 9 leads to similar results as for the one-limb core transformer “T1” in subsection 4.1.5.

Table 9: “T2”: Computation time of different 3D TrafoLoss-models

No.	Model	No. of equations	Computation time hh:mm:ss
1	3D TrafoLoss model – Standard FE mesh as in Fig. 47 and Fig. 48.	945612	00:44:37
2	3D TrafoLoss model – Standard FE mesh – without eddy current region	671720	00:03:32

4.3 Three-limb core transformer “T3”

4.3.1 Technical data

The three-limb core transformer “T3” (three phases) is designed to operate at a nominal power of 250 MVA at operating voltages of $230 \pm 2 \times 4,5$ kV on the HV-side and 34,5 kV on the LV-side. A connection in the vector group Dyn1 leads to a LV-current of 4184 A. The three-stage adjustable HV-disk winding which is constructed from several disks with two different drilled conductors, is operated with 653,1 A at the tap, with 627,6 A in the middle position and with 603,9 A at the lowest tap of the tap-changer. The operating frequency is 60 Hz. The two-layer LV-winding is manufactured with a drilled conductor with 43 strands, where one strand has the dimensions 6,12x1,34 mm.

4.3.2 3D TrafoLoss-model

The simplified 3D TrafoLoss-model of the transformer “T3” consists of a three-limb core, a clamping structure, simplified tank shielding and yoke shielding. The LV-layer winding is constructed with two cylindrical coils (one coil per layer). The HV-winding consists of nine axial parallel winding blocks with different current densities. The geometry of this transformer is shown in Fig. 49.

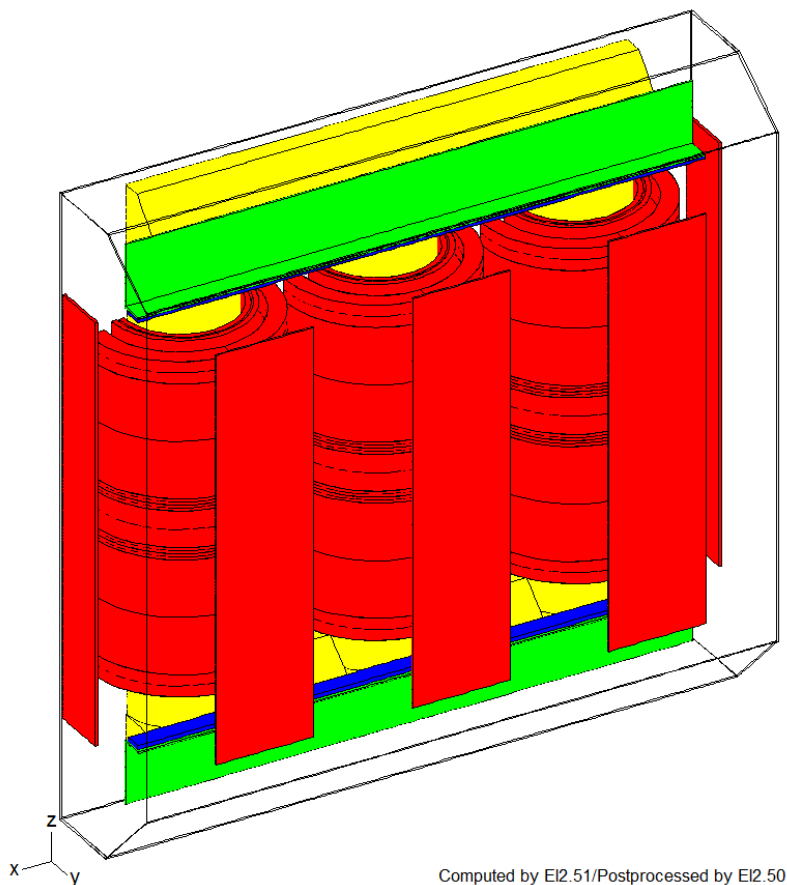


Fig. 49. “T3”: 3D TrafoLoss-model

Based on the results of the investigation of the dependence of additional losses on mesh refinement in subsection 3.3.2, the mesh for the three-limb core transformer “T3” is chosen as shown in Figs. 50 and 51.

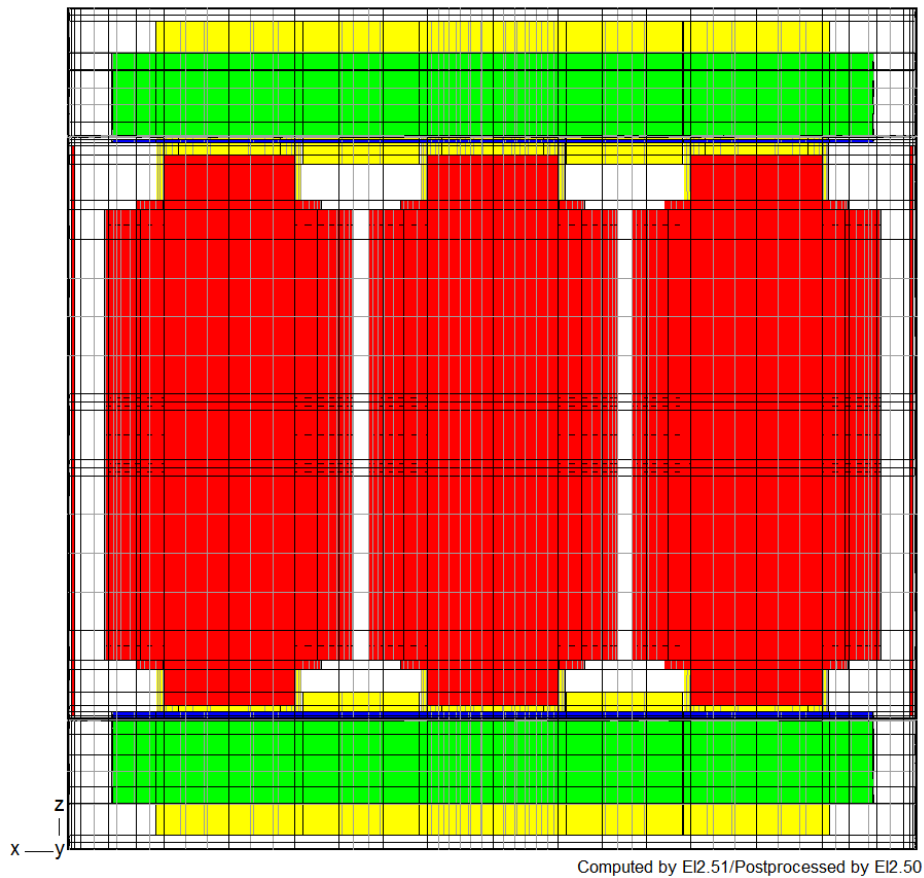


Fig. 50. “T3”: Finite element mesh in x-z-plane

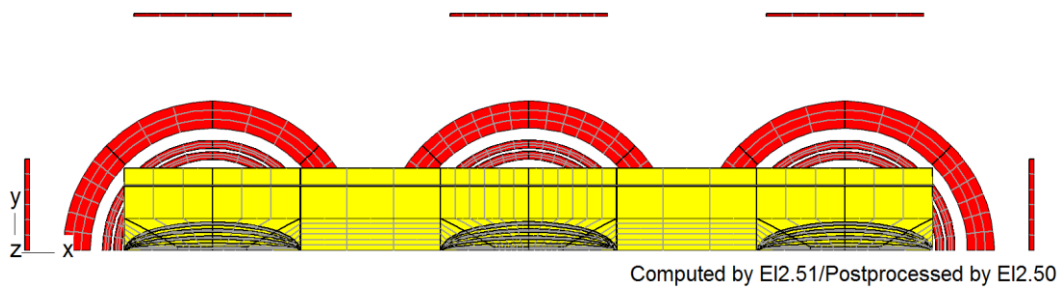


Fig. 51. “T3”: Finite element mesh in x-y-plane

4.3.3 Loss comparison

Table 10 shows a comparison of the 3D TrafoLoss-model to the 2D models.

Table 10: "T3": Loss comparison of 2D models and 3D TrafoLoss-model

Model		I ² R W	P _{rad} W	P _{ax} W	Total W
2D model – detailed modelling of windings as in Fig. 10	Winding LV layer 1	153182	4663	1195	
	Winding LV layer 2	171354	3376	12252	
	Winding HV	413559	15275	17768	
	TOTAL	738095	23314	31215	792624
2D model – coarse modelling of windings as in Fig. 10	Winding LV layer 1	153182	4672	1195	
	Diff. to standard2D model in %	0,00	0,19	0,00	
	Winding LV layer 2	171354	3350	12265	
	Diff. to detailed 2D model in %	0,00	0,78	0,11	
	Winding HV	413559	15215	18100	
	Diff. to detailed 2D model in %	0,00	0,39	1,83	
TOTAL	738095	23237	31560	792892	
3D TrafoLoss-model – Standard FE mesh as in Fig. 50 and Fig. 51	Winding LV layer 1 left	51061	1417	395	
	Winding LV layer 1 centre	51061	1505	397	
	Winding LV layer 1 right	51061	1414	395	
	Winding LV layer 1	153182	4337	1186	
	Diff. to coarse 2D model in %	0,00	7,73	0,72	
	Diff. to detailed 2D model in %	0,00	7,52	0,72	
	Winding LV layer 2 left	57118	1058	4086	
	Winding LV layer 2 centre	57118	1179	4097	
	Winding LV layer 2 right	57118	1053	4086	
	Winding LV layer 2	171354	3291	12269	
	Diff. to coarse 2D model in %	0,00	1,80	0,03	
	Diff. to detailed 2D model in %	0,00	2,59	0,14	
	Winding HV left	140564	5708	6178	
	Winding HV centre	140564	6212	6397	
	Winding HV right	140564	5682	6176	
	Winding HV	421693	17601	18751	
Diff. to coarse 2D model in %	1,93	13,56	3,47		
Diff. to detailed 2D model in %	1,93	13,22	5,24		
TOTAL	746229	25229	32207	803665	

In addition to the well-known differences between 2D and 3D models (changing geometry in the azimuthal direction), the transformer "T3" is manufactured as a three-phase transformer. This results in different radial additional losses on the three limbs, which can be taken into account in the 3D TrafoLoss-model. It can be observed, that the radial losses of the LV-windings are less than in the coarse 2D model, whereas they are higher in the high voltage winding. The axial additional losses only differ in the high voltage winding.

4.3.4 Effects of eddy currents in non-active steel parts

A comparison of the standard model with computed eddy currents in clamping structure and tank to the eddy current free model is shown in Table 11.

Table 11: “T3”: Comparison of eddy current free model with the standard 3D TrafoLoss-model

Model		I^2R W	P_{rad} W	P_{ax} W	Total W
3D TrafoLoss-model – Standard FE mesh as in Fig. 50 and Fig. 51	Winding LV layer 1 left	51061	1417	395	
	Winding LV layer 1 centre	51061	1505	397	
	Winding LV layer 1 right	51061	1414	395	
	Winding LV layer 1	153182	4337	1186	
	Winding LV layer 2 left	57118	1058	4086	
	Winding LV layer 2 centre	57118	1179	4097	
	Winding LV layer 2 right	57118	1053	4086	
	Winding LV layer 2	171354	3291	12269	
	Winding HV left	140564	5708	6178	
	Winding HV centre	140564	6212	6397	
	Winding HV right	140564	5682	6176	
	Winding HV	421693	17601	18751	
	TOTAL	746229	25229	32207	803665
	3D TrafoLoss-model – standard FE mesh – without eddy current region	Winding LV layer 1 left	51061	1454	396
Winding LV layer 1 centre		51061	1507	397	
Winding LV layer 1 right		51061	1451	396	
Winding LV layer 1		153182	4412	1189	
Diff. to standard 3D model in %		0,00	1,70	0,25	
Winding LV layer 2 left		57118	1111	4092	
Winding LV layer 2 centre		57118	1185	4097	
Winding LV layer 2 right		57118	1106	4091	
Winding LV layer 2		171354	3402	12280	
Diff. to standard 3D model in %		0,00	3,37	0,09	
Winding HV left		140564	6055	6195	
Winding HV centre		140564	6449	6216	
Winding HV right		140564	6023	6194	
Winding HV		421693	18527	18605	
Diff. to standard 3D model in %	0,00	5,26	0,77		
TOTAL	746229	26341	32073	804643	

An analysis of the results shown in Table 11 indicates significant differences to the one-limb core transformer “T1” in subsection 4.1.4 or the two-limb core transformer “T2” in subsection 4.2.4. While the results of the single-phase models practically do not differ for eddy current and eddy current free models, there are differences for the three-phase transformer “T3”. A comparison of the radial additional losses in Table 11 justifies the statement that, in this case, the eddy currents should be considered in the calculation.

4.3.5 Computation times

An important issue arising when computing large 3D models with eddy currents is the computation time. Such models result in a nearly 95 % higher number of equations in the equation system to be solved and hence a much more time consuming calculation process. A comparison of the number of equations and computation times can be seen in Table 12.

Table 12: "T3": Computation time of different 3D TrafoLoss-models

No.	Model	No. of equations	Computation time hh:mm:ss
1	3D TrafoLoss model – Standard FE mesh as in Fig. 50 and Fig. 51	1307158	05:40:51
2	3D TrafoLoss model – Standard FE mesh – without eddy current region	671720	00:12:18

4.4 Four-limb core transformer "T4"

4.4.1 Technical data

The four-limb core single-phase transformer "T4" is designed for a nominal power of 400 MVA. The voltage on the generator side is specified with 22 kV, which leads to a current of 18182 A. The high voltage side with the attached five step tap changer can be operated with a system voltage of $52/\sqrt{3}$ kV $\pm 2 \times 1,25\%$. This results in currents from 1289 A ($537,5/\sqrt{3}$ kV) to 1351,9 A ($512,5/\sqrt{3}$ kV), whereas the current in the middle position of the tap changer will be 1319,7 A. The operating frequency is 60 Hz. The LV-winding of the transformer "T4" is manufactured as a one layer cylindrical winding with a drilled conductor (79x(5,89x1,74mm)). The tapped HV-winding is constructed from several disks with three different conductors. The voltage input is thereby located in the winding centre.

4.4.2 3D TrafoLoss-model

Transferring the technical data into a FEM 3D model with modelled windings leads to the transformer shown in Fig. 52. The finite element mesh in x-z-plane as well as in x-y-plane is shown in Figs. 53 and 54.

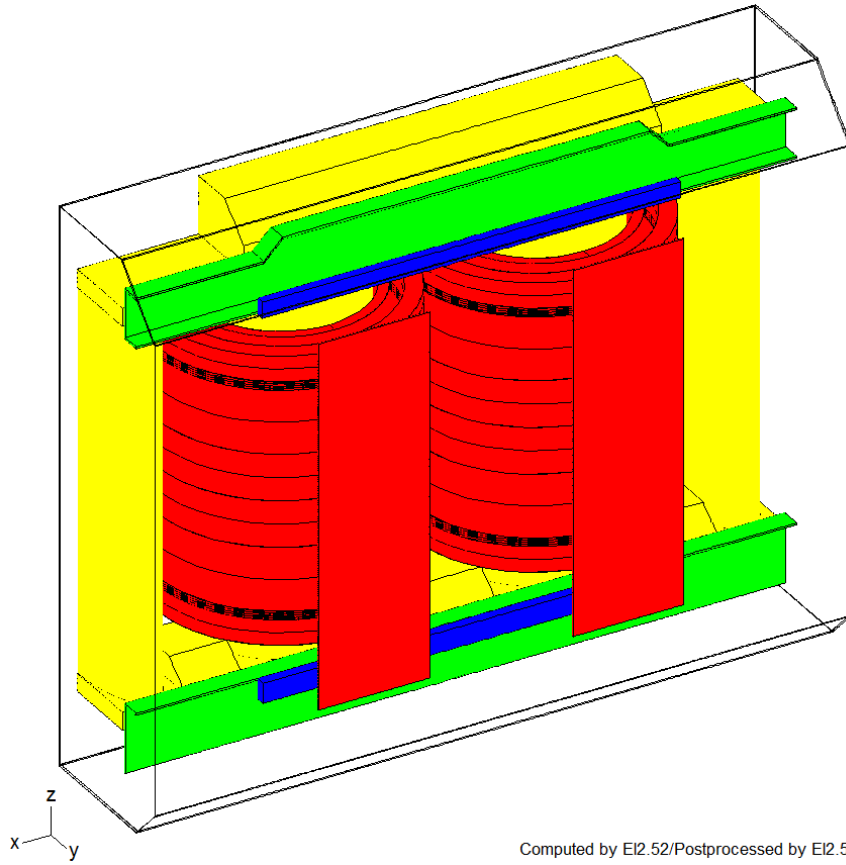


Fig. 52. "T4": 3D TrafoLoss-model

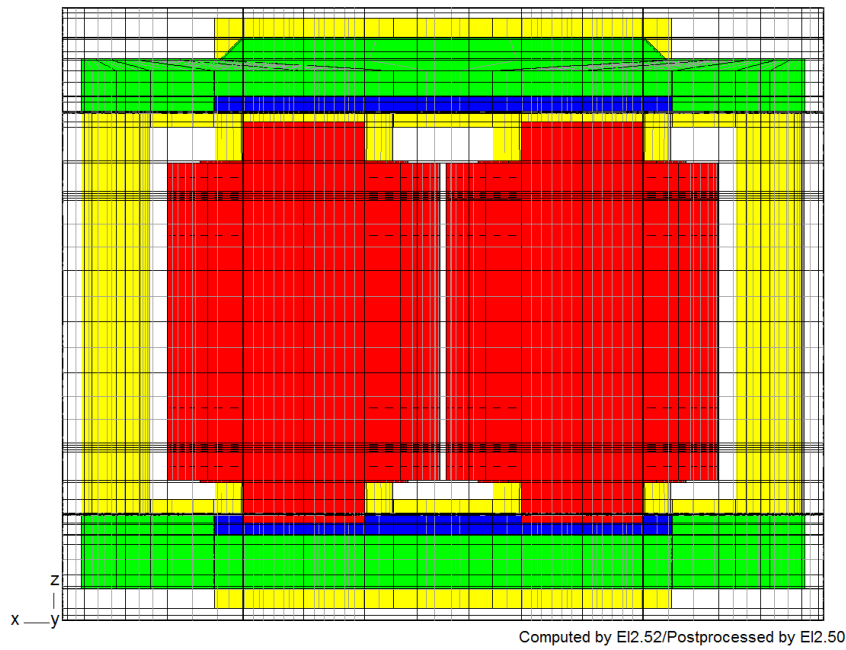


Fig. 53. "T4": Finite element mesh in x-z-plane

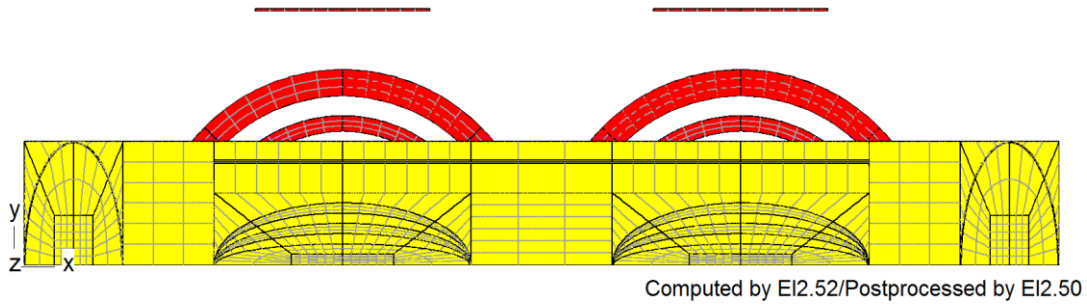


Fig. 54. "T4": Finite element mesh in x-y-plane

4.4.3 Loss comparison

A loss comparison of coarse 2D model and 3D TrafoLoss-model (Table 13) shows a similarity to the other single-phase transformers "T1" and "T2". The axial additional losses are nearly the same, while the radial additional losses in the LV-winding are smaller than in the 2D model and in the HV-winding they are increasing. In general, this leads to a difference in radial additional losses of about 4 %.

Table 13: "T4": Loss comparison of 2D models and 3D TrafoLoss-model

Model		I ² R W	P _{rad} W	P _{ax} W	Total W
2D model – detailed modelling of windings as in Fig. 10	Winding LV	210126	10183	16541	
	Winding HV	263516	11622	29512	
	TOTAL	473642	21805	46053	541500
2D model – coarse modelling of windings in Fig. 10	Winding LV	210126	10296	16558	
	Diff. to detailed 2D model in %	0,00	1,10	0,10	
	Winding HV	263516	12177	29946	
	Diff. to detailed 2D model in %	0,00	4,56	1,45	
TOTAL	473642	22473	46504	542619	
3D TrafoLoss-model – Standard FE mesh as in Fig. 47 and Fig. 48.	Winding LV left	105253	4037	8242	
	Winding LV right	105253	4034	8242	
	Winding LV	210506	8072	16484	
	Diff. to coarse 2D model in %	0,18	27,56	0,45	
	Diff. to detailed 2D model in %	0,18	26,16	0,34	
	Winding HV left	132951	6770	15234	
	Winding HV right	132951	6754	15234	
	Winding HV	265901	13524	30468	
	Diff. to coarse 2D model in %	0,90	9,96	1,71	
Diff. to detailed 2D model in %	0,90	14,06	3,14		
TOTAL	476407	21595	46953	544955	

4.4.4 Effects of eddy currents in non-active steel parts

Comparing the 3D TrafoLoss-model with computed eddy currents to that without eddy current domains in Table 14 shows nearly the same result.

Table 14: „T4“: Comparison of eddy current free model with the standard 3D TrafoLoss-model

Model		I ² R W	P _{rad} W	P _{ax} W	Total W
3D TrafoLoss-model – Standard FE mesh as in Fig. 53 and Fig. 54.	Winding LV left	105253	4037	8242	
	Winding LV right	105253	4034	8242	
	Winding LV	210506	8072	16484	
	-				
	Winding HV left	132951	6770	15234	
	Winding HV right	132951	6754	15234	
	Winding HV	265901	13524	30468	
	-				
	TOTAL	476407	21595	46953	544955
3D TrafoLoss-model – standard FE mesh – without eddy current region	Winding LV left	105253	4006	8246	
	Winding LV right	105253	4005	8246	
	Winding LV	210506	8011	16493	
	Diff. to standard 3D model in %	0,00	0,75	0,05	
	Winding HV left	132951	6825	15250	
	Winding HV right	132951	6799	15247	
	Winding HV	265901	13624	30497	
	Diff. to standard 3D model in %	0,00	0,73	0,10	
	TOTAL	476407	21636	46990	545032

4.4.5 Computation times

The comparison of the number of equations and computation time of eddy current model and magnetic model in Table 15 shows differences. Combined with the results from Table 14, the use of simplified models (without eddy current domains) for calculating the additional winding losses is recommended for further calculations of four-limb core transformers.

Table 15: „T4“: Computation time of different 3D TrafoLoss-models

No.	Model	No. of equations	Computation time hh:mm:ss
1	3D TrafoLoss model – Standard FE mesh Fig. 53 and Fig. 54.	1519907	00:04:53
2	3D TrafoLoss model – Standard FE mesh – without eddy current region	1105064	13:12:58

4.5 Five-limb core transformer “T5”

4.5.1 Technical data

The five-limb core transformer “T5” is designed for a high voltage of 400 kV which can be regulated with an on-load tap changer in 19 steps ($400 \pm 9 \times 1,25 \%$). The operation voltage on the LV-side is 20 kV. The vector group YNd11 leads to currents from 665,6 A up to 834,3 A at lowest tap. The current on the low voltage side is 14809 A. To get this functionality, four windings are necessary. The HV-winding is thereby realized by several disks with three different conductors used. The LV-winding is implemented as a one layer cylindrical winding with a drilled conductor with 55 strands (5,4x1,92mm). To realize the controllability, a coarse regulation winding (implemented as a one layer cylindrical winding) and a fine regulation winding are also necessary.

4.5.2 3D TrafoLoss-model

The 3D TrafoLoss-model of the three-phase-transformer “T5” can be seen in Fig. 55. The corresponding finite element mesh is shown in Fig. 56 (x-z-plane) and in Fig. 57 (x-y-plane without tank, clamping structure and yoke shielding).

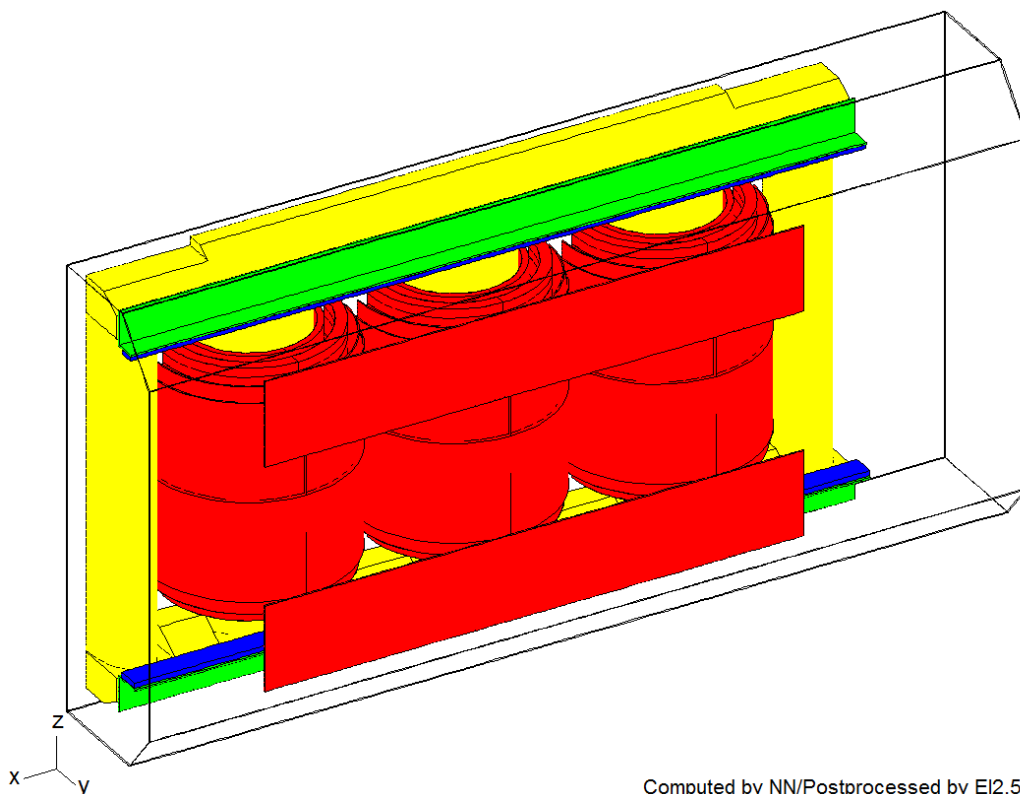


Fig. 55. “T5”: 3D TrafoLoss-model

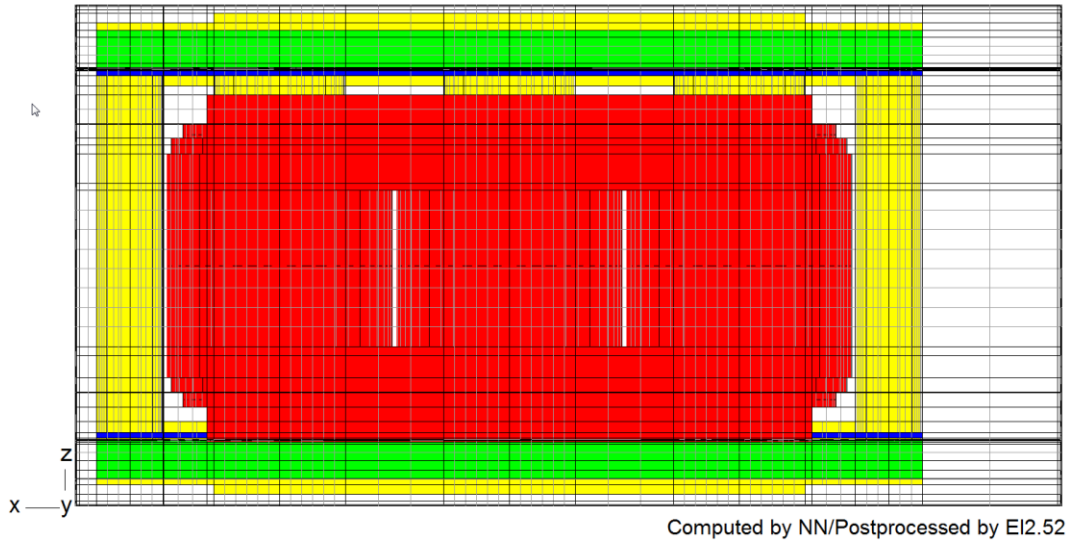


Fig. 56. "T5": Finite element mesh in x-z-plane

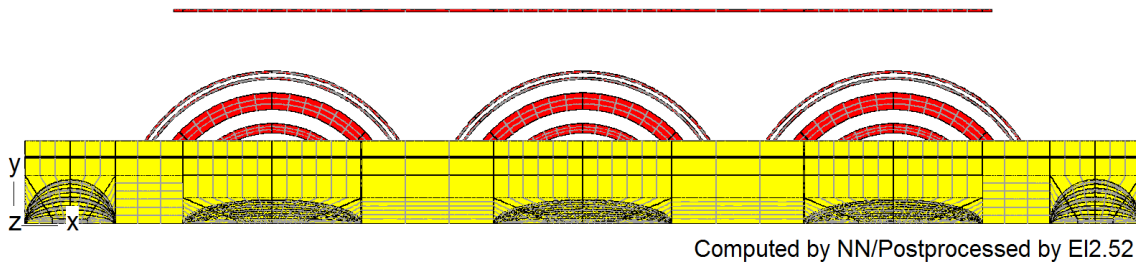


Fig. 57. "T5": Finite element mesh in x-y-plane

4.5.3 Loss comparison

A comparison of the losses, computed with the coarse 2D model in Table 16 to those of the 3D model in Table 17 shows strong similarities to the transformers already examined. On the one hand there is a known difference in the so called t-losses of disk windings and just a small change in axial additional losses while, on the other hand, the radial additional losses are different. As already seen at the other transformers, the radial additional losses of the inner coil are smaller in the 3D model while the losses from the outer coils are larger. This leads to a total deviation in radial additional losses of just about 9,5 %.

Table 16: "T5": Loss comparison of the 2D models

Model		I^2R W	P_{rad} W	P_{ax} W	Total W
2D model – detailed modelling of windings as in Fig. 11	Winding LV	658987	13006	25824	
	Winding HV	508684	20266	35259	
	Winding GST	99400	2128	33	
	FST	0	1601	270	
	TOTAL	1267071	37001	61386	1365458
2D model – coarse modelling of windings as in Fig. 10	Winding LV	658987	13285	25834	
	Diff. to standard2D model in %	0,00	2,10	0,04	
	Winding HV	508684	20532	35859	
	Diff. to detailed 2D model in %	0,00	1,30	1,67	
	Winding GST	99400	2145	33	
	Diff. to detailed 2D model in %	0,00	0,79	0,00	
	FST	0	1586	268	
Diff. to detailed 2D model in %	0	0,95	0,75		
TOTAL	1267071	37548	61994	1366613	

Table 17: "T5": Losses of the 3D TrafoLoss-model

Model		I ² R	P _{rad}	P _{ax}	Total
		W	W	W	W
3D TrafoLoss-model – Standard FE mesh as in Fig. 56 and Fig. 57	Winding LV left	219662	3547	8486	
	Winding LV centre	219662	3550	8487	
	Winding LV right	219662	3533	8485	
	Winding LV	658987	10629	25457	
	Diff. to coarse 2D model in %	0,00	24,98	1,48	
	Diff. to detailed 2D model in %	0,00	22,36	1,44	
	Winding HV left	175041	8772	12306	
	Winding HV centre	175041	8804	12312	
	Winding HV right	175041	8608	12303	
	Winding HV	525124	26184	36920	
	Diff. to coarse 2D model in %	3,13	21,59	2,87	
	Diff. to detailed 2D model in %	3,13	22,60	4,50	
	Winding GST left	33133	818	12	
	Winding GST centre	33133	817	12	
	Winding GST right	33133	805	12	
	Winding GST	99400	2440	36	
	Diff. to coarse 2D model in %	0,00	12,08	6,06	
	Diff. to detailed 2D model in %	0,00	12,78	6,06	
	Winding FST left	0	620	89	
	Winding FST centre	0	616	95	
	Winding FST right	0	606	91	
	Winding FST	0	1843	276	
	Diff. to coarse 2D model in %	0	13,94	2,75	
Diff. to detailed 2D model in %	0	13,12	2,02		
TOTAL		1283511	41096	62688	1387295

4.5.4 Effects of eddy currents in non-active steel parts

Analysing the losses of the 3D model without computed eddy currents in Table 18 and comparing them to the losses of the model with considered eddy currents in non-active steel parts in Table 17 leads to the conclusion that just the radial additional losses of the outer windings (HV, GST and FST) are slightly different. Therefore also the model without computed eddy currents is acceptable for computing the additional losses.

Table 18: "T5": Losses of the 3D TrafoLoss-model without eddy current region

Model		I^2R	P_{rad}	P_{ax}	Total
		W	W	W	W
3D TrafoLoss-model – standard FE mesh – without eddy current region	Winding LV left	219662	3566	8489	
	Winding LV centre	219662	3571	8489	
	Winding LV right	219662	3563	8489	
	Winding LV	658987	10700	25467	
	Diff. to standard 3D model in %	0,00	0,67	0,04	
	Winding HV left	175041	9088	12309	
	Winding HV centre	175041	9050	12313	
	Winding HV right	175041	9082	12308	
	Winding HV	525124	27220	36930	
	Diff. to standard 3D model in %	0,00	3,96	0,03	
	Winding GST left	33133	846	12	
	Winding GST centre	33133	839	12	
	Winding GST right	33133	845	12	
	Winding GST	99400	2530	36	
	Diff. to standard 3D model in %	0,00	3,69	0,00	
	Winding FST left	0	648	84	
	Winding FST centre	0	640	91	
	Winding FST right	0	641	85	
	Winding FST	0	1929	260	
	Diff. to standard 3D model in %	0,00	4,67	5,79	
TOTAL		1283511	42378	62692	1388580

4.5.5 Computation times

Considering the computation times of the two models (shown in Table 19) and the fact that just the radial additional losses are slightly different, leads to the conclusion that the model without computed eddy currents in non-active steel parts have to be preferred for future calculations on five-limb core transformers.

Table 19: "T5": Computation time of different 3D TrafoLoss-models

No.	Model	No. of equations	Computation time hh:mm:ss
1	3D TrafoLoss model – Standard FE mesh Fig. 56 and Fig. 57	2090775	44:44:58
2	3D TrafoLoss model – Standard FE mesh – without eddy current region	1572748	01:32:27

5 Influence of winding modelling on additional losses in non-active steel parts

As described in section 1.4, the second part of this thesis is an investigation of the influence of winding modelling on additional losses in non-active steel parts. Currently the windings in the 3D FEM-model are modelled by one cylindrical coil per winding. In the following chapter a comparison by the means of the five benchmark transformers between this way of winding modelling and the way, described in subsection 2.2.1.1 will be done.

5.1 One-limb core transformer “T1”

Implementing the windings is leading to the current densities shown in Table 1. Fig. 58 shows a comparison of the geometry plots of “T1”, on the one hand built up with one axial winding block on HV-side and on the other hand modelled with several axial winding blocks with the current densities according Table 1. The voltage input of the HV-winding is located in the winding centre. Therefore Table 1 contains only the winding blocks of the upper half of the HV-winding. To get the current densities of the lower half, the table entries have to be mirrored.

All other transformers with voltage input in the winding centre will be treated the same way.

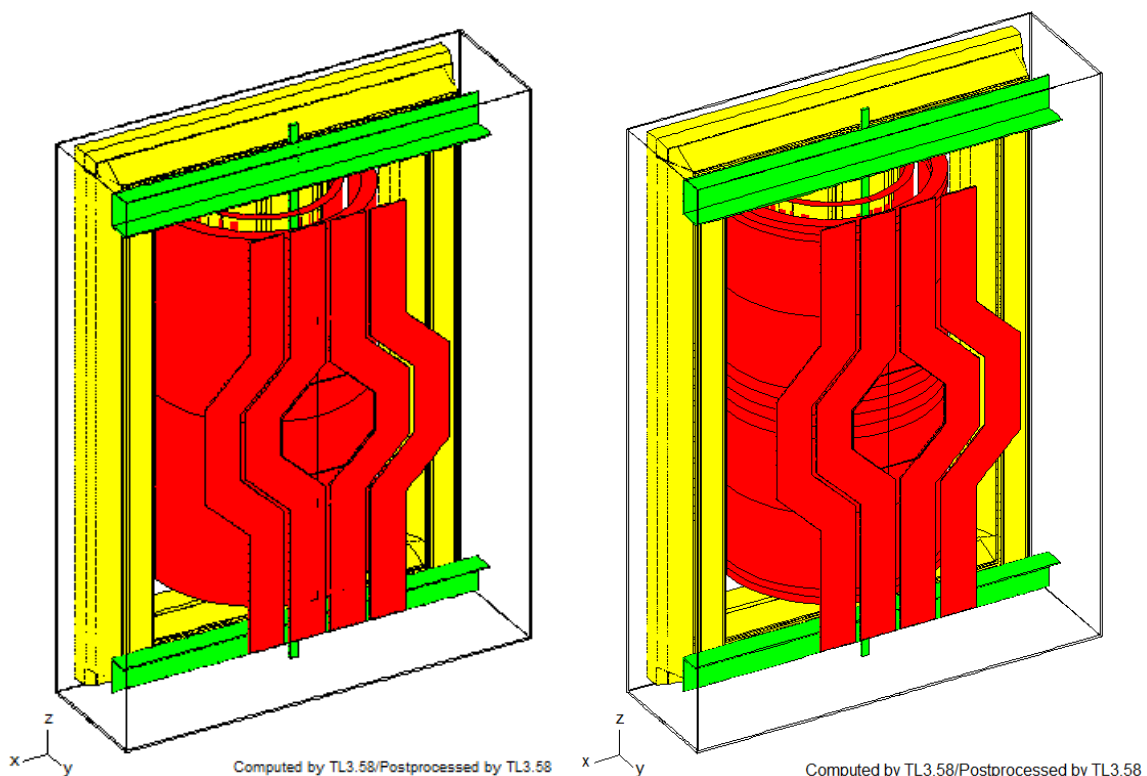


Fig. 58. “T1”: Geometry plots, left: one axial winding block on HV-side; right: several axial winding blocks on HV-side

5.1.1 Field plots

A comparison of the maximum surface flux density plots in Figs. 59 to 61 shows a decreasing maximum value for $\max|B|$ in the case of detailed winding modelling. This quantity shows the maximum modulus of B in all points of time. Also the field trends in the specified figures show a decrease of field intensity. The magnetic surface flux density in the tie bars is nearly the same for both ways of winding modelling.

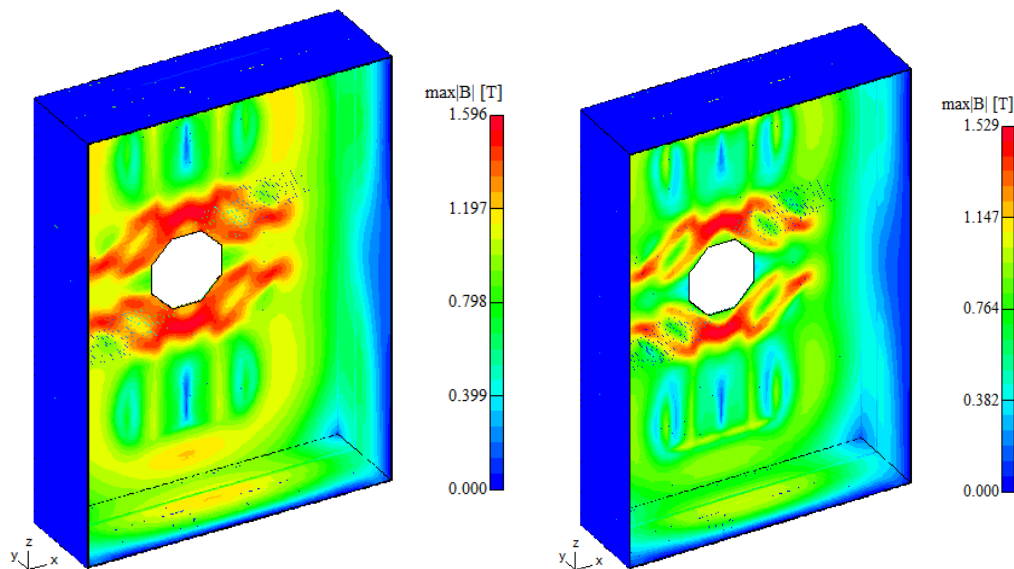


Fig. 59. "T1": Max. surface flux density in tank, left: one axial winding block on HV-side; right: several axial winding blocks on HV-side

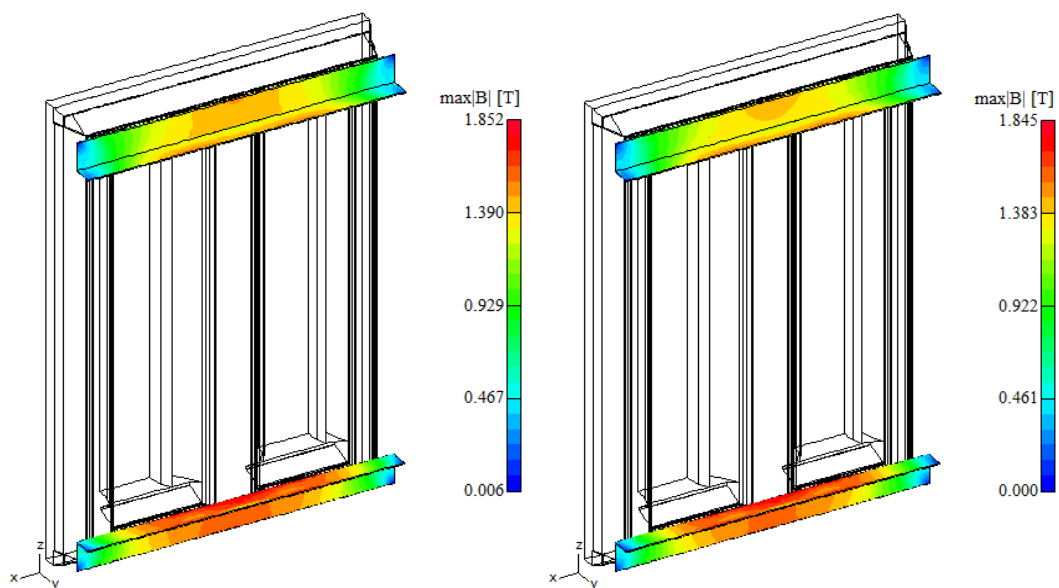


Fig. 60. "T1": Max. surface flux density in clamping structure, left: one axial winding block on HV-side; right: several axial winding blocks on HV-side

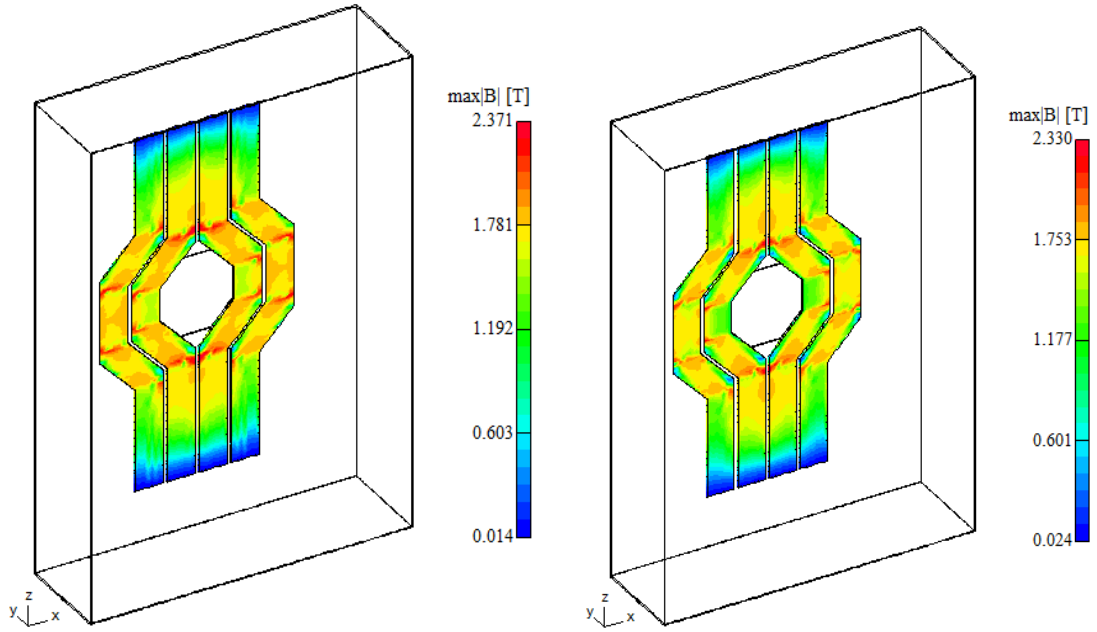


Fig. 61. "T1": Max. surface flux density in tank shielding, left: one axial winding block on HV-side; right: several axial winding blocks on HV-side

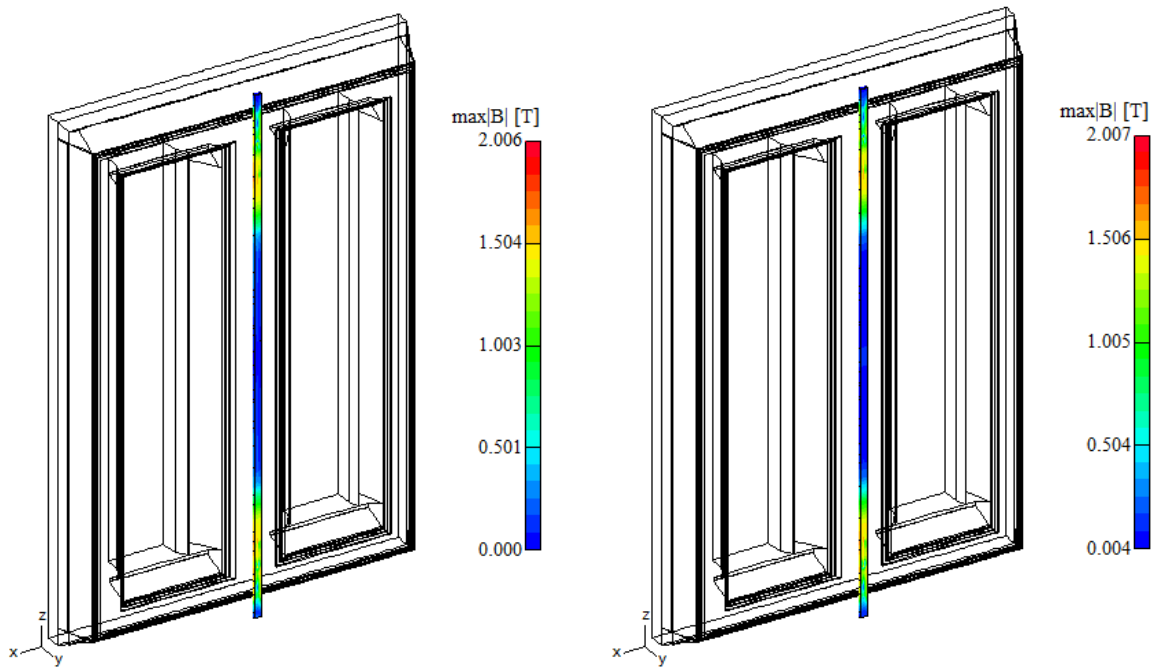


Fig. 62. "T1": Max. surface flux density in tie bars, left: one axial winding block on HV-side; right: several axial winding blocks on HV-side

5.1.2 Loss comparison

Comparing the results in Table 20 and Table 21 confirm the trend which could be seen in the field plots. The losses of the model with several axial winding blocks are slightly smaller than the losses of the model with one axial winding block. Especially the tank losses are much smaller in the second model where the other losses are similar to them from the first model.

Table 20: "T1", one axial winding block on HV-side, losses in non-active steel parts

Component Name	Eddy current Losses W	Specific Losses W	Hysteresis Losses W	Total Losses W
Tank 1/2	1496	0	755	2250
Tank Wall behind	1187	0	564	1751
Tank Cover (1/2)	115	0	65	180
Tank Bottom (1/2)	111	0	64	175
Tank Wall left (1/2)	42	0	31	74
Tank Wall right (1/2)	41	0	30	72
Core (1/2)	236	2036	0	2272
Clampings	2003	0	506	2509
Vertical Plate, bottom	880	0	160	1040
Horizontal Plate, bottom	542	0	141	683
Vertical Plate, top	407	0	104	511
Horizontal Plate, top	174	0	102	275
Tie Bars	71	0	23	94
Tank Shielding, total	0	581	0	581
Tank Shielding vertical, behind	0	581	0	581
Total Losses	3805	2618	1284	7707

Table 21: “T1”, several axial winding blocks on HV-side, losses in non-active steel parts

Component Name	Eddy current	Specific	Hysteresi	Total
	Losses	Losses	s Losses	Losses
	W	W	W	W
Tank 1/2	715	0	410	1125
Tank Wall behind	560	0	301	861
Tank Cover (1/2)	60	0	39	99
Tank Bottom (1/2)	59	0	38	97
Tank Wall left (1/2)	19	0	16	35
Tank Wall right (1/2)	18	0	16	34
Core (1/2)	227	1969	0	2196
Clampings	1817	0	467	2284
Vertical Plate, bottom	802	0	147	949
Horizontal Plate, bottom	502	0	134	636
Vertical Plate, top	362	0	94	456
Horizontal Plate, top	151	0	92	242
Tie Bars	70	0	23	93
Tank Shielding, total	0	488	0	488
Tank Shielding vertical, behind	0	488	0	488
Total Losses	2829	2458	899	6186

5.2 Two-limb core transformer “T2”

The HV-winding of the two-limb core (single-phase) transformer “T2” consists of 14 axial parallel winding blocks. The voltage input is located in the winding centre. Fig. 63 shows a comparison of the two models (left: one winding block on HV-side, right: several winding blocks on HV-side).

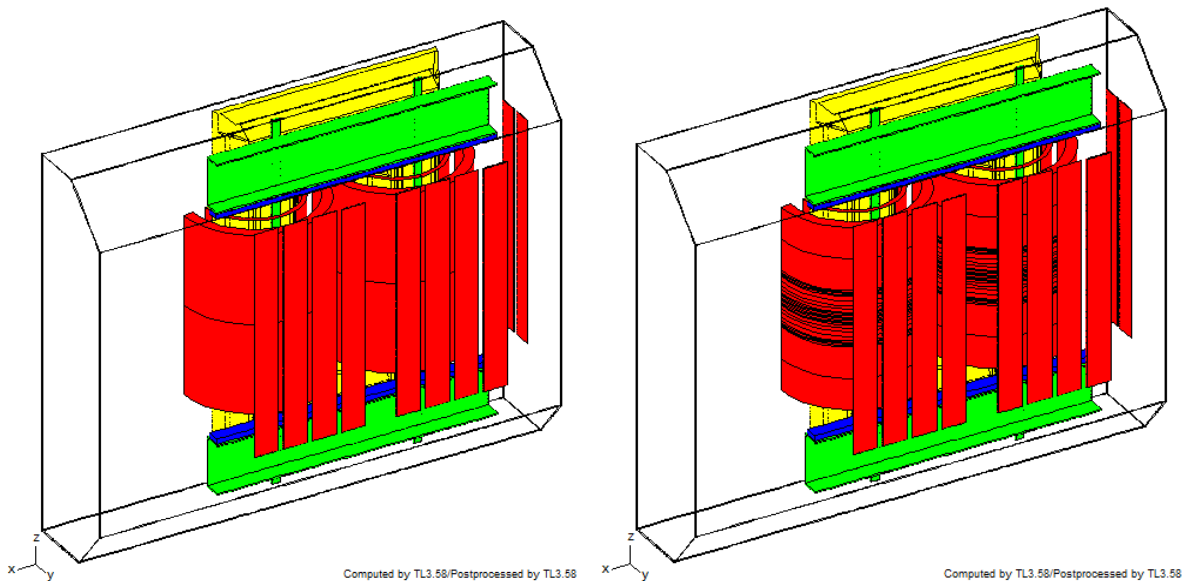


Fig. 63. "T2": Geometry plots, left: one axial winding block on HV-side; right: several axial winding blocks on HV-side

Table 22 shows the differences in current densities in the HV-windings of the two models. Larger differences to the mean current density in the model with one axial winding block can only be found in the winding centre, where the voltage input is located. Because of symmetrical reasons only the upper half of axial winding blocks is shown in Table 22.

Table 22: "T2": Current densities in winding segments

Winding parts	HV-winding with one axial block J_{peak} in A/m ²	HV-winding with several axial blocks J_{peak} in A/m ²
Winding part 1	0,123*10 ⁷	0,130*10 ⁷
Winding part 2		0,121*10 ⁷
Winding part 3		0,117*10 ⁷
Winding part 4		0,105*10 ⁷
Winding part 5		0,989*10 ⁶
Winding part 6		0,948*10 ⁶
Winding part 7		0,906*10 ⁶

5.2.1 Field plots

The results which can be seen in the different field plots are similar to the results for the one-limb core transformer "T1" in section 5.1. A more detailed way of winding modelling leads to a decrease of the maximum modulus of the magnetic flux density B at transformers with a HV-disk winding with voltage input in the winding centre.

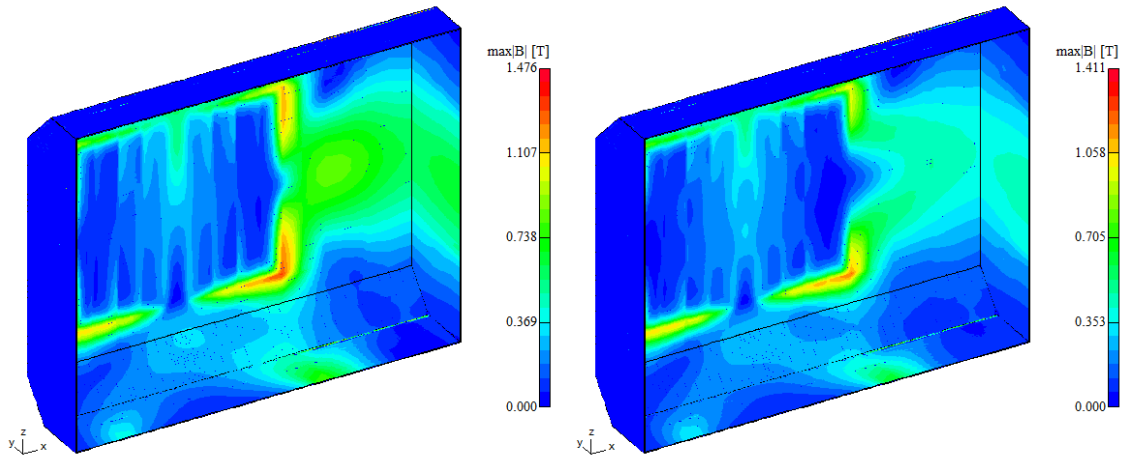


Fig. 64. "T2": Max. surface flux density in tank, left: one axial winding block on HV-side; right: several axial winding blocks on HV-side

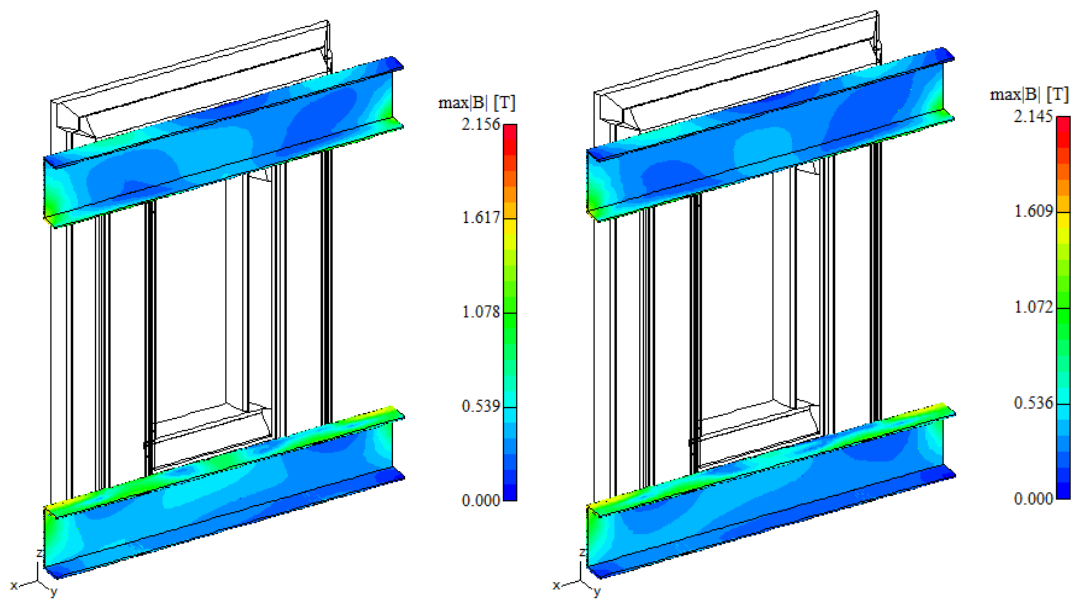


Fig. 65. "T2": Max. surface flux density in clamping structure, left: one axial winding block on HV-side; right: several axial winding blocks on HV-side

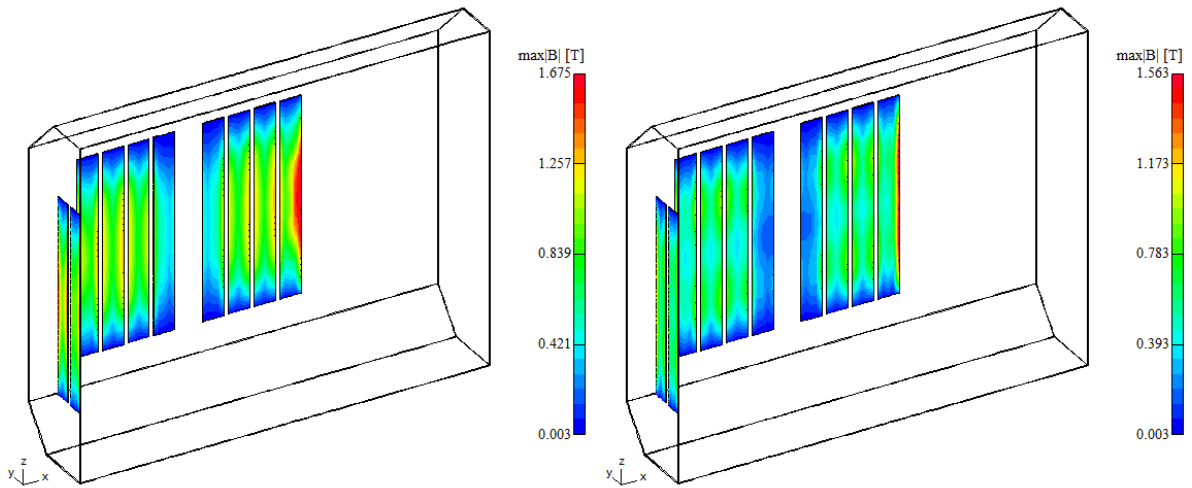


Fig. 66. "T2": Max. surface flux density in tank shielding, left: one axial winding block on HV-side; right: several axial winding blocks on HV-side

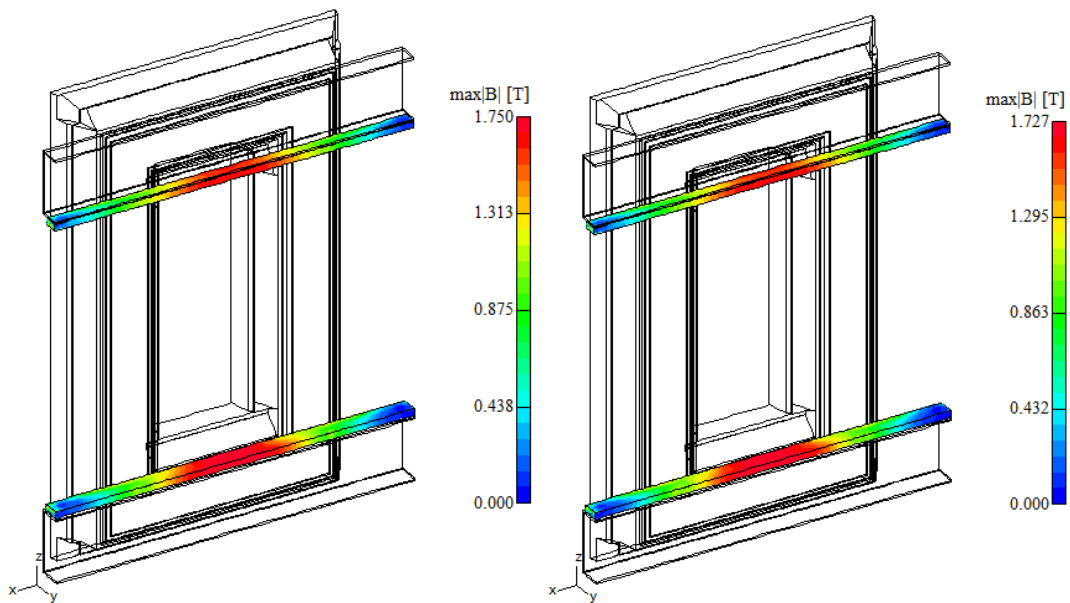


Fig. 67. "T2": Max. surface flux density in yoke shielding, left: one axial winding block on HV-side; right: several axial winding blocks on HV-side

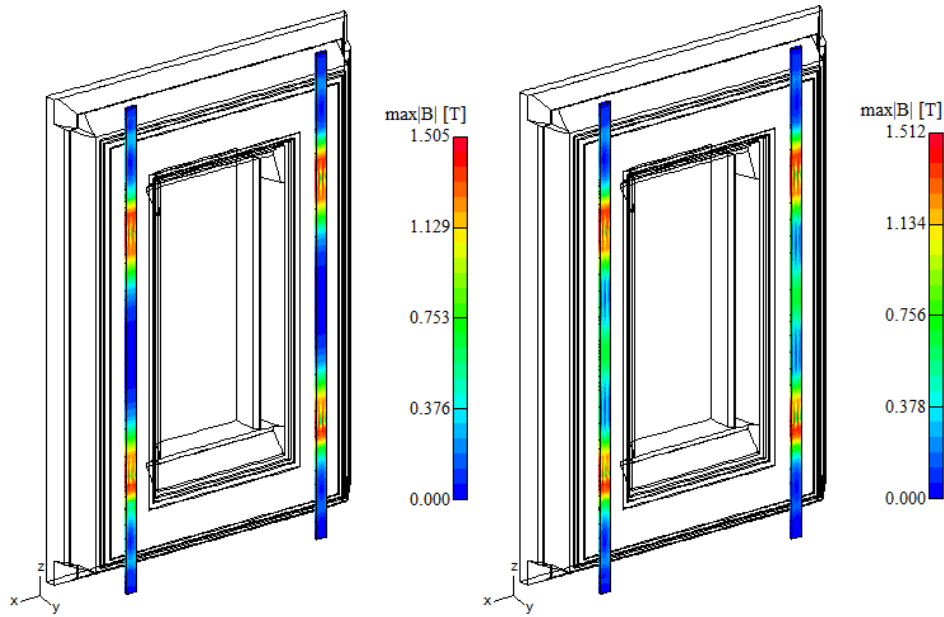


Fig. 68. “T2”: Max. surface flux density in tie bars, left: one axial winding block on HV-side; right: several axial winding blocks on HV-side

5.2.2 Loss comparison

Table 23 and Table 24 show the losses of the different models. While there are larger differences in tank- and tank shielding losses, the losses in clamping structure, tie bars and yoke shielding are nearly the same. The core losses increase in the second model.

Table 23: "T2", one axial winding block on HV-side, losses in non-active steel parts

Component Name	Eddy current	Specific	Hysteresis	Total
	Losses	Losses	Losses	Losses
	W	W	W	W
Tank 1/2	327	0	232	559
Tank Wall behind	215	0	150	365
Tank Wall left (1/2)	47	0	31	78
Tank Wall right (1/2)	35	0	27	62
Tank Cover (1/2)	16	0	13	30
Tank Bottom (1/2)	14	0	12	25
Core (1/2)	242	425	0	667
Clampings	184	0	123	307
Vertical Plate, bottom	55	0	36	91
Horizontal Plate, bottom	51	0	33	84
Horizontal Plate, top	42	0	28	71
Vertical Plate, top	36	0	25	61
Tie Bars	88	0	40	128
Tie Bar right	44	0	20	64
Tie Bar left	44	0	20	64
Tank Shielding, total	0	184	0	184
Tank Shielding vertical, behind	0	144	0	144
Tank Shielding, left (1/2)	0	39	0	39
Yoke Shieldings, behind	0	347	0	347
Yoke Shielding, bottom	0	208	0	208
Yoke Shielding, top	0	139	0	139
Total Losses	842	955	394	2191

Table 24: "T2", several axial winding blocks on HV-side, losses in non-active steel parts

Component Name	Eddy current	Specific	Hysteresis	Total
	Losses	Losses	Losses	Losses
	W	W	W	W
Tank 1/2	191	0	151	343
Tank Wall behind	124	0	97	221
Tank Wall left (1/2)	29	0	20	49
Tank Wall right (1/2)	18	0	16	34
Tank Cover (1/2)	12	0	10	22
Tank Bottom (1/2)	9	0	8	17
Core (1/2)	296	606	0	902
Clampings	155	0	104	260
Vertical Plate, bottom	43	0	29	73
Horizontal Plate, bottom	45	0	28	73
Horizontal Plate, top	37	0	25	62
Vertical Plate, top	30	0	22	52
Tie Bars	95	0	43	138
Tie Bar right	47	0	21	69
Tie Bar left	47	0	21	69
Tank Shielding, total	0	88	0	88
Tank Shielding vertical, behind	0	68	0	68
Tank Shielding, left (1/2)	0	20	0	20
Yoke Shieldings, behind	0	329	0	329
Yoke Shielding, bottom	0	198	0	198
Yoke Shielding, top	0	131	0	131
Total Losses	737	1023	299	2059

5.3 Three-limb core transformer “T3”

The three-phase transformer “T3” consists of a two-layer LV-winding combined with an HV-disk winding with voltage input at the upper and the lower end of the winding. This leads to the winding geometries in Fig. 71, where the LV-winding of the left model consists of one radial and axial winding block and the LV-winding of the right model is modelled from one radial coil with one axial block per layer.

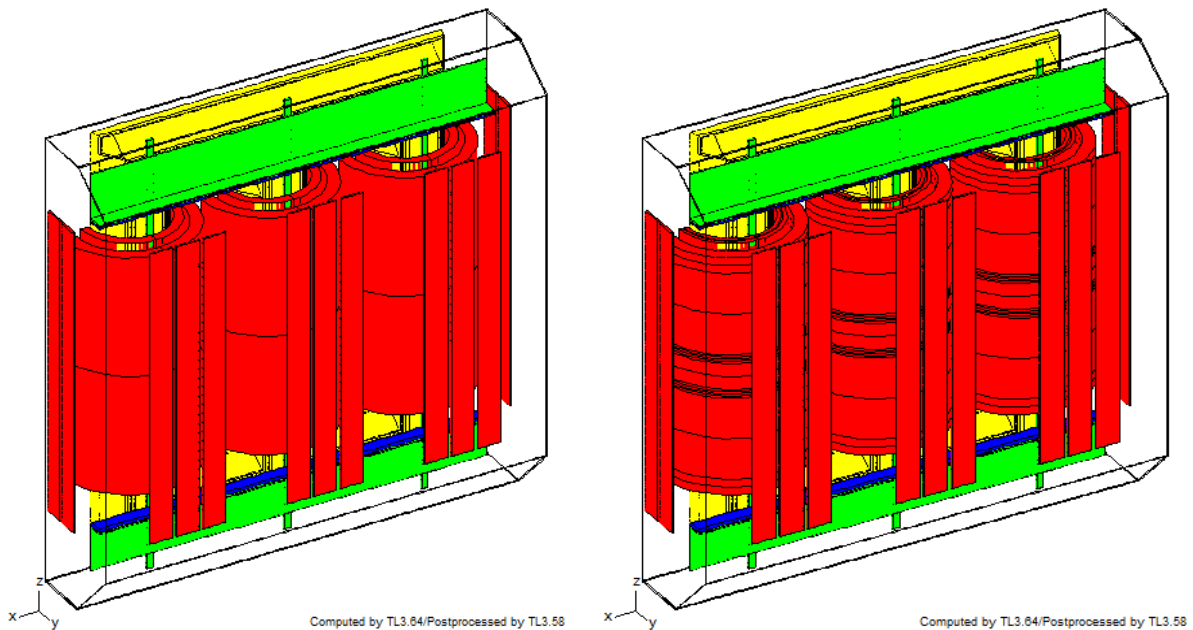


Fig. 69. “T3”: Geometry plots, left: one axial winding block on HV-side; right: several axial winding blocks on HV-side

Comparing the current densities of the two models in Table 25 shows large differences between the models in the LV-windings as well as in the HV-windings. The differences in the LV-windings are resulting from a small air gap between the two layers. The influences of this way of modelling layer windings with more than one layers is treated in subsection 5.3.2.1. The fact that the voltage input of this transformer is located at the winding ends leads to large differences between the mean current density and the current densities of the winding parts located at the winding ends.

Table 25: "T3": Current densities in winding segments

Winding parts	HV-winding with one axial block	HV-winding with several axial blocks
	J_{peak} in A/m ²	J_{peak} in A/m ²
HV	NV Coil 1	0.368*10 ⁷
	NV Coil 2	0.368*10 ⁷
	Winding part 1	0.189*10 ⁷
	Winding part 2	0.229*10 ⁷
	Winding part 3	0.233*10 ⁷
	Winding part 4	0.233*10 ⁷
	Winding part 5	0.224*10 ⁷
	Winding part 6	0.227*10 ⁷
	Winding part 7	0.233*10 ⁷
	Winding part 8	0.229*10 ⁷
	Winding part 9	0.189*10 ⁷

5.3.1 Field Plots

The differences in the current densities in the upper and lower winding blocks result in large differences in the field plots. Especially tank and tank shielding are concerned. Yoke shielding and tie bars stay nearly unaffected. The results of plotting the maximum modulus of surface flux density for every transformer part can be seen in Figs. 70 to 74.

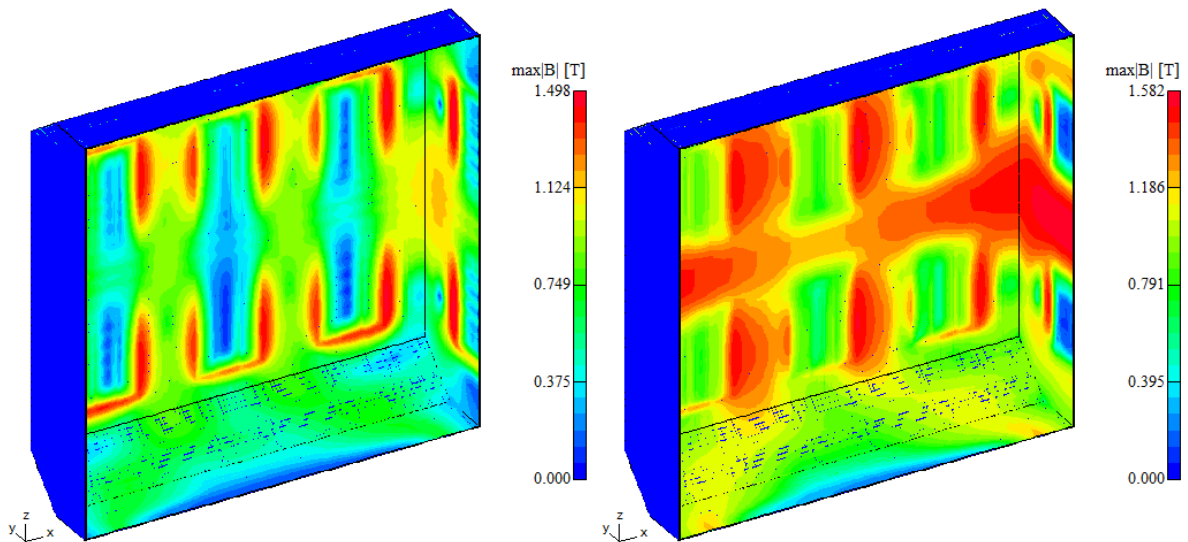


Fig. 70. "T3": Max. surface flux density in tank, left: one axial winding block on HV-side; right: several axial winding blocks on HV-side

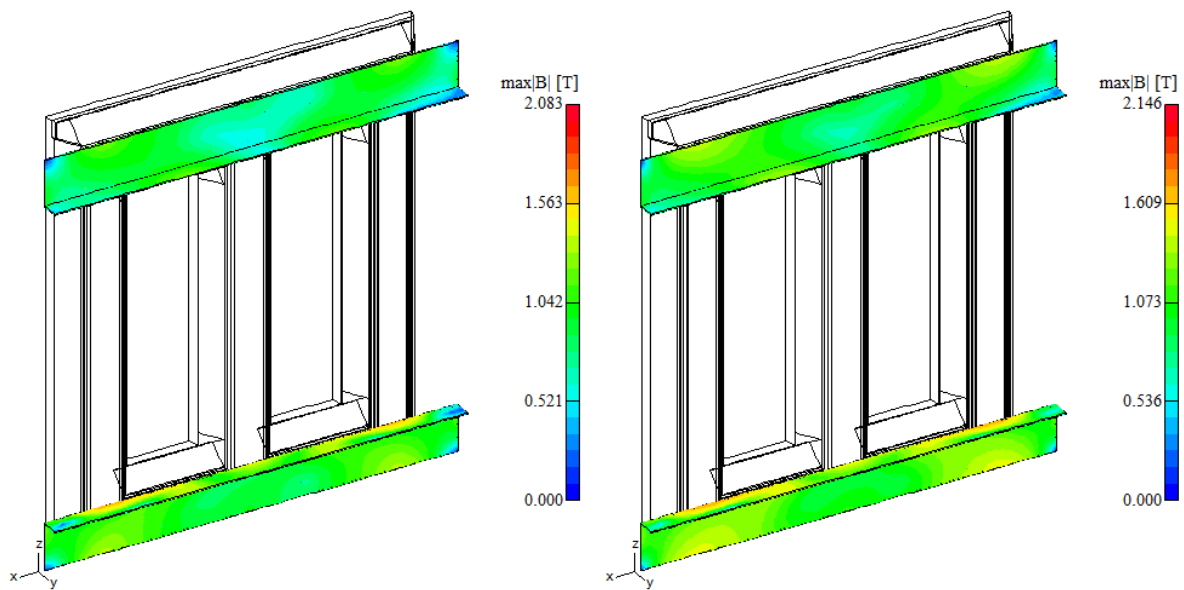


Fig. 71. "T3": Max. surface flux density in clamping structure, left: one axial winding block on HV-side; right: several axial winding blocks on HV-side

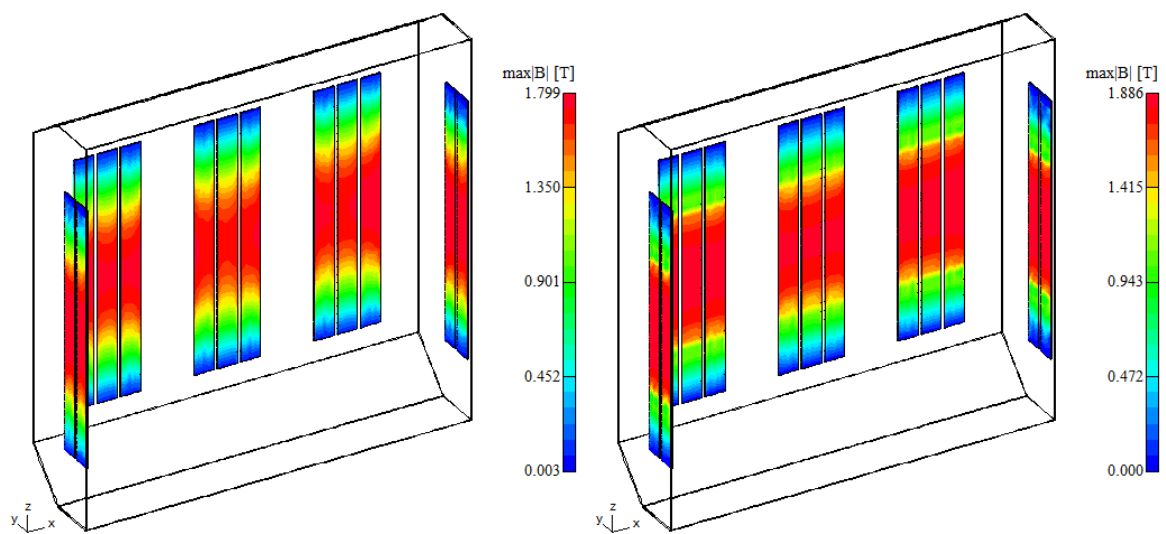


Fig. 72. "T3": Max. surface flux density in tank shielding, left: one axial winding block on HV-side; right: several axial winding blocks on HV-side

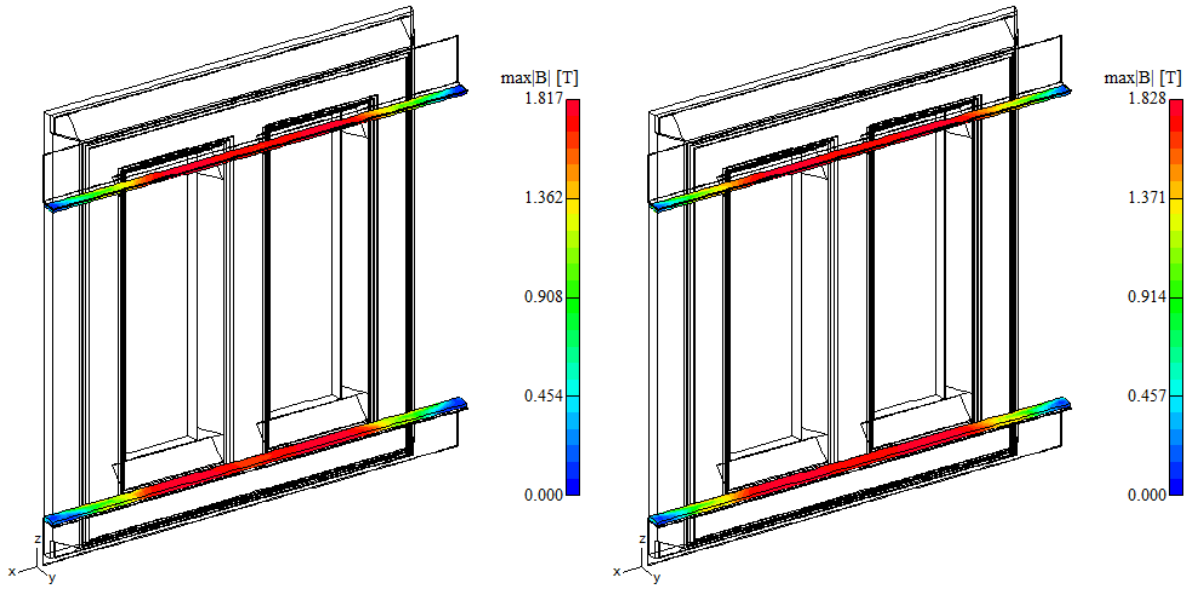


Fig. 73. "T3": Max. surface flux density in yoke shielding, left: one axial winding block on HV-side; right: several axial winding blocks on HV-side

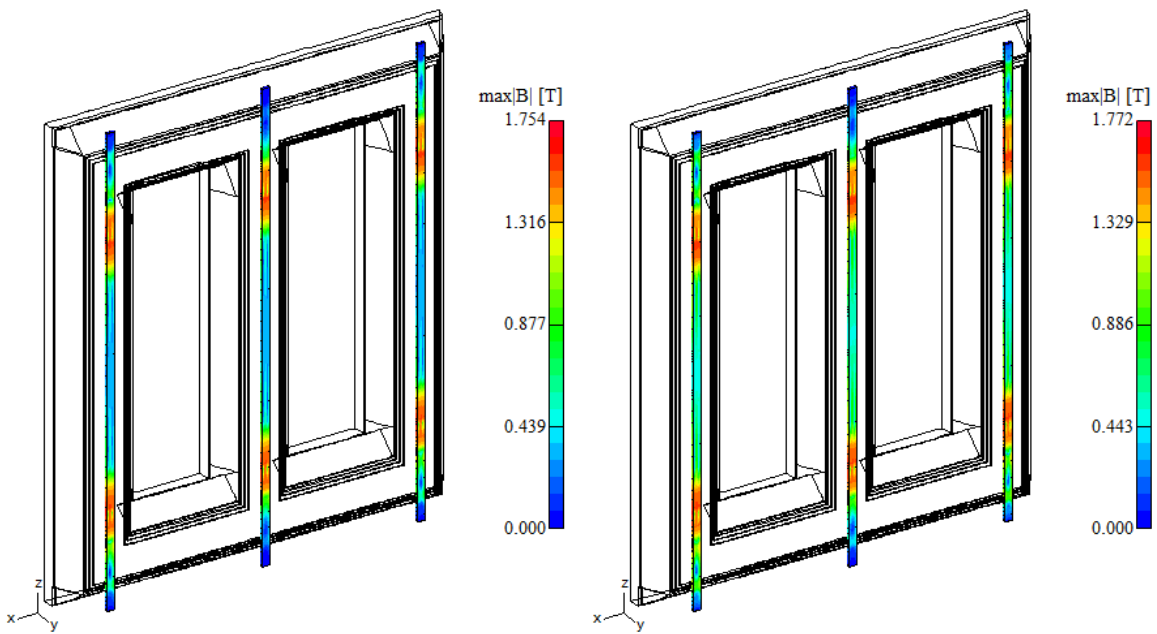


Fig. 74. "T3": Max. surface flux density in tie bars, left: one axial winding block on HV-side; right: several axial winding blocks on HV-side

5.3.2 Loss comparison

As already expected from the differences in the field plots, the losses are also different. Especially the tank losses are affected from a more detailed way of winding modelling. Comparing Table 26 and Table 27 shows an increase in tank losses by more than 300 %. Because of this and because of the maximum flux density in the tank shielding is bigger than 1,8 T, it can be assumed that the tank shielding is undersized.

Table 26: "T3", one axial winding block on HV-side, losses in non-active steel parts

Component Name	Eddy current	Specific	Hysteresi	Total
	Losses	Losses	s Losses	Losses
	W	W	W	W
Tank 1/2	1457	0	727	2185
Tank Wall behind	926	0	462	1389
Tank Wall left (1/2)	239	0	115	355
Tank Wall right (1/2)	237	0	114	351
Tank Cover (1/2)	30	0	19	49
Tank Bottom (1/2)	25	0	16	41
Core (1/2)	522	1547	0	2069
Clampings	721	0	351	1071
Vertical Plate, bottom	324	0	132	457
Vertical Plate, top	189	0	92	281
Horizontal Plate, bottom	141	0	72	213
Horizontal Plate, top	66	0	55	121
Tie Bars	300	0	90	390
Tie Bar right	102	0	31	132
Tie Bar left	100	0	30	130
Tie Bar centre	98	0	29	128
Tank Shielding, total	0	1066	0	1066
Tank Shielding vertical, behind	0	603	0	603
Tank Shielding, left (1/2)	0	234	0	234
Tank Shielding, right (1/2)	0	229	0	229
Yoke Shieldings, behind	0	288	0	288
Yoke Shielding, bottom	0	175	0	175
Yoke Shielding, top	0	113	0	113
Total Losses	3000	2901	1168	7069

Table 27: “T3”, several axial winding blocks on HV-side, losses in non-active steel parts

Component Name	Eddy current	Specific	Hysteresis	Total
	Losses	Losses	Losses	Losses
	W	W	W	W
Tank 1/2	4829	0	1776	6605
Tank Wall behind	2824	0	1094	3918
Tank Wall left (1/2)	946	0	297	1243
Tank Wall right (1/2)	855	0	279	1133
Tank Bottom (1/2)	104	0	53	157
Tank Cover (1/2)	100	0	53	153
Core (1/2)	618	1584	0	2202
Clampings	1391	0	530	1921
Vertical Plate, bottom	615	0	201	816
Vertical Plate, top	355	0	142	497
Horizontal Plate, bottom	280	0	105	385
Horizontal Plate, top	142	0	82	224
Tie Bars	362	0	108	471
Tie Bar right	124	0	37	161
Tie Bar left	122	0	36	158
Tie Bar centre	116	0	35	151
Tank Shielding, total	0	1356	0	1356
Tank Shielding vertical, behind	0	784	0	784
Tank Shielding, left (1/2)	0	288	0	288
Tank Shielding, right (1/2)	0	284	0	284
Yoke Shieldings, behind	0	321	0	321
Yoke Shielding, bottom	0	194	0	194
Yoke Shielding, top	0	127	0	127
Total Losses	7200	3261	2415	12876

5.3.2.1 Influence of radial distribution of cylindrical windings with more than one layer

To obviate an influence of modelling every layer of the LV-winding, Table 28 shows the results of a model with a detailed HV-winding and one radial coil for the LV-winding. Comparing this to the results in Table 27 shows only a small difference in core losses, while the other losses are nearly the same.

Table 28: "T3", several axial winding blocks on HV-side and only one radial coil on LV-side, losses in non-active steel parts

Component Name	Eddy current Losses W	Specific Losses W	Hysteresis Losses W	Total Losses W
Tank 1/2	4831	0	1776	6607
Tank Wall behind	2825	0	1095	3920
Tank Wall left (1/2)	947	0	297	1244
Tank Wall right (1/2)	855	0	279	1134
Tank Bottom (1/2)	104	0	53	157
Tank Cover (1/2)	101	0	53	153
Core (1/2)	600	2094	0	2694
Clampings	1388	0	530	1918
Vertical Plate, bottom	615	0	201	816
Vertical Plate, top	355	0	142	497
Horizontal Plate, bottom	278	0	105	383
Horizontal Plate, top	140	0	82	222
Tie Bars	356	0	108	464
Tie Bar right	122	0	37	159
Tie Bar left	120	0	36	156
Tie Bar centre	114	0	34	149
Tank Shielding, total	0	1354	0	1354
Tank Shielding vertical, behind	0	783	0	783
Tank Shielding, left (1/2)	0	287	0	287
Tank Shielding, right (1/2)	0	283	0	283
Yoke Shieldings, behind	0	320	0	320
Yoke Shielding, bottom	0	193	0	193
Yoke Shielding, top	0	126	0	126
Total Losses	7175	3767	2414	13356

5.4 Four-limb core transformer “T4”

The HV-winding of the four-limb core transformer “T4” is accomplished as a disk winding with partly interleaved and tapped disks. Therefore in the nominal position, some winding parts are currentless. The distribution of the upper winding parts (voltage input in the winding centre) can be seen in Table 29.

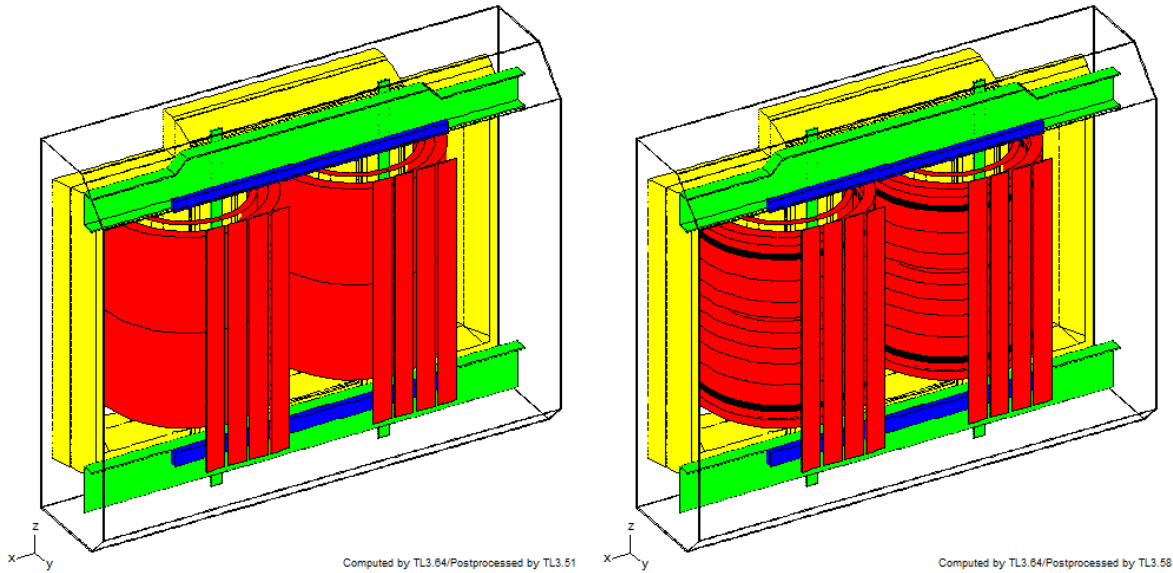


Fig. 75. “T4”: Geometry plots, left: one axial winding block on HV-side; right: several axial winding blocks on HV-side

Table 29: “T4”: Current densities in winding segments

Winding parts	HV-winding with one axial block	HV-winding with several axial blocks
	J_{peak} in A/m ²	J_{peak} in A/m ²
Winding part 1	0.174*10 ⁷	0.195*10 ⁷
Winding part 2		0.000*10 ⁷
Winding part 3		0.000*10 ⁷
Winding part 4		0.000*10 ⁷
Winding part 5		0.000*10 ⁷
Winding part 6		0.188*10 ⁷
Winding part 7		0.176*10 ⁷

5.4.1 Field Plots

Plots of the maximum flux density of every part of both models show a consistently increase of the maximum value of $\max|\mathbf{B}|$ of every plot and also a slightly worse field profile, excepting the tank. In this case the upper scale value for the magnetic flux density is lower in the model with detailed HV-windings but in the field profile of the second model are more points with the maximum scale value than in the model with one cylindrical coil representing the HV-winding.

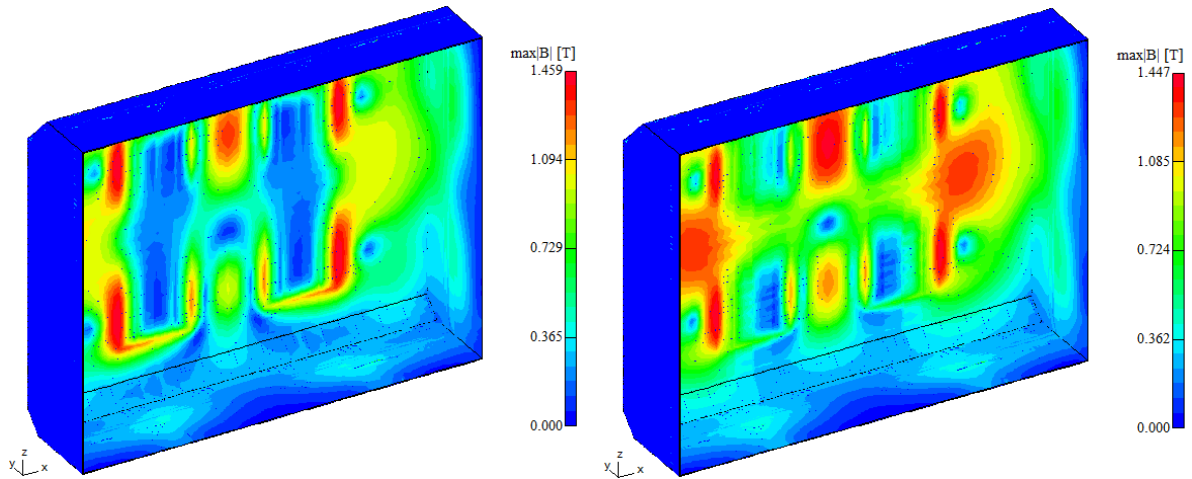


Fig. 76. “T4”: Max. surface flux density in tank, left: one axial winding block on HV-side; right: several axial winding blocks on HV-side

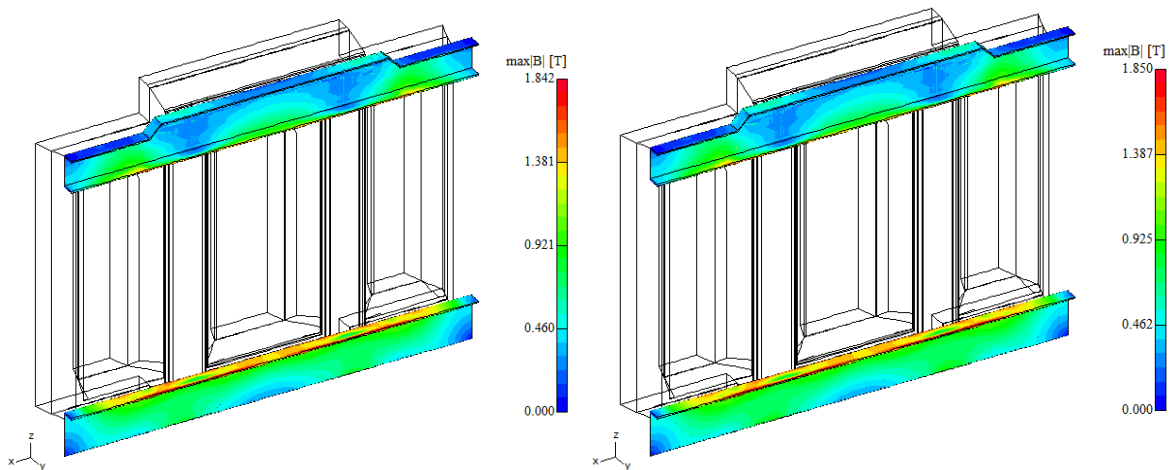


Fig. 77. “T4”: Max. surface flux density in clamping structure, left: one axial winding block on HV-side; right: several axial winding blocks on HV-side

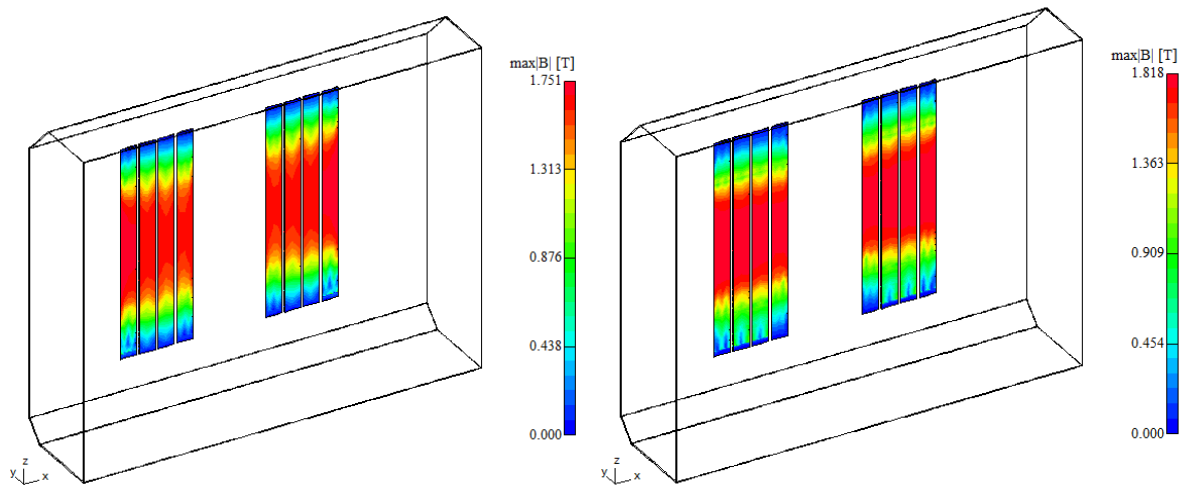


Fig. 78. "T4": Max. surface flux density in tank shielding, left: one axial winding block on HV-side; right: several axial winding blocks on HV-side

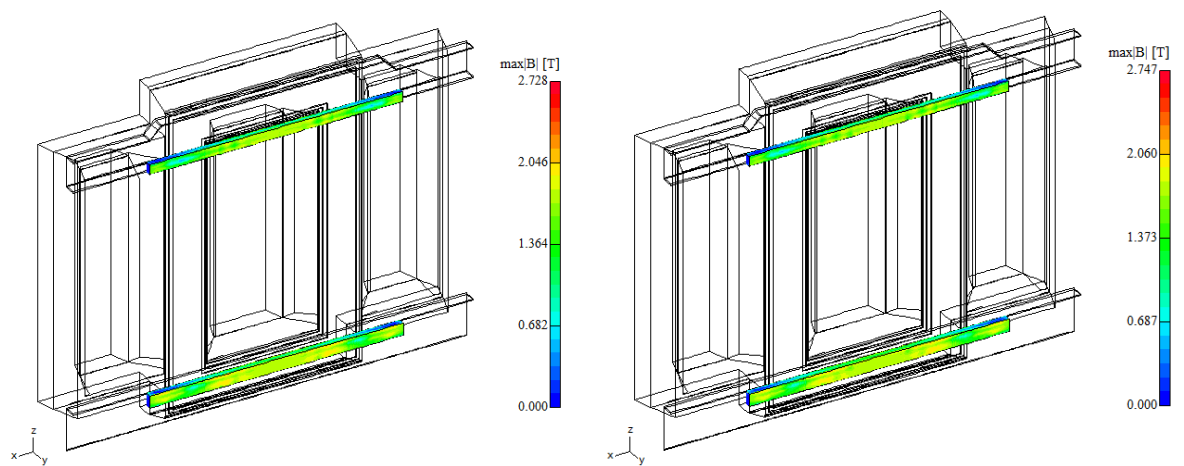


Fig. 79. "T4": Max. surface flux density in yoke shielding, left: one axial winding block on HV-side; right: several axial winding blocks on HV-side

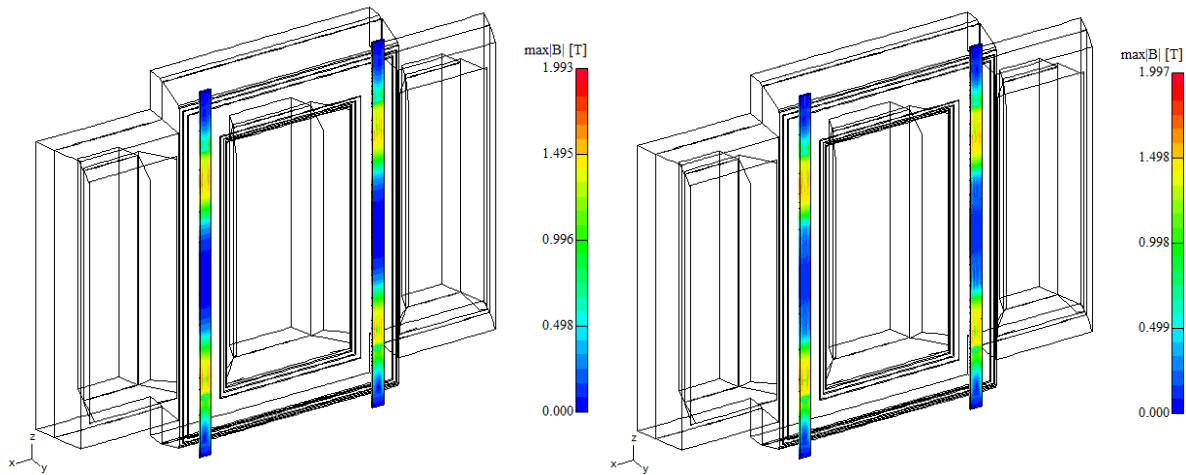


Fig. 80. “T4”: Max. surface flux density in tie bars, left: one axial winding block on HV-side; right: several axial winding blocks on HV-side

5.4.2 Loss comparison

A comparison of Table 29 and Table 30 shows, as expected after reviewing the field plots, an increase in total losses where the losses of every part are slightly bigger in the second (more detailed) model. The biggest increase could be found in the tank. Comparing the results to those of the other two single-phase transformers “T1” and “T2” results in the conclusion that the losses in this case are larger, but the absolute differences between the models are not very significant.

Table 30: "T4", one axial winding block on HV-side, losses in non-active steel parts

Component Name	Eddy current	Specific	Hysteresis	Total
	Losses	Losses	Losses	Losses
	W	W	W	W
Tank 1/2	814	0	478	1292
Tank Wall behind	702	0	390	1092
Tank Wall left (1/2)	41	0	31	72
Tank Wall right (1/2)	38	0	29	67
Tank Cover (1/2)	19	0	15	35
Tank Bottom (1/2)	13	0	13	26
Core (1/2)	621	3856	0	3856
Clampings	1267	0	413	1679
Vertical Plate, bottom	504	0	161	665
Horizontal Plate, bottom	478	0	118	595
Vertical Plate, top	151	0	74	224
Horizontal Plate, top	134	0	61	195
Tie Bars	390	0	116	505
Tie Bar left	195	0	58	253
Tie Bar right	195	0	58	253
Tank Shielding, total	0	423	0	423
Tank Shielding vertical, behind	0	423	0	423
Yoke Shieldings, behind	152	428	0	428
Yoke Shielding, bottom	110	287	0	287
Yoke Shielding, top	42	140	0	140
Total Losses	3244	3934	1007	8185

Table 31: "T4", several axial winding blocks on HV-side, losses in non-active steel parts

Component Name	Eddy current	Specific	Hysteresis	Total
	Losses	Losses	Losses	Losses
	W	W	W	W
Tank 1/2	1205	0	659	1864
Tank Wall behind	1064	0	559	1623
Tank Wall left (1/2)	50	0	36	85
Tank Wall right (1/2)	48	0	35	83
Tank Cover (1/2)	28	0	16	44
Tank Bottom (1/2)	15	0	14	28
Core (1/2)	616	4036	0	4036
Clampings	1316	0	425	1741
Vertical Plate, bottom	525	0	165	690
Horizontal Plate, bottom	496	0	120	616
Vertical Plate, top	156	0	76	233
Horizontal Plate, top	140	0	64	203
Tie Bars	434	0	126	561
Tie Bar left	217	0	63	280
Tie Bar right	217	0	63	280
Tank Shielding, total	0	499	0	499
Tank Shielding vertical, behind	0	499	0	499
Yoke Shieldings, behind	178	469	0	469
Yoke Shielding, bottom	131	320	0	320
Yoke Shielding, top	47	149	0	149
Total Losses	3749	4209	1211	9169

5.5 Five-limb core transformer “T5”

Beside the one layer LV-winding and the HV-disk winding with voltage input at the upper and lower winding ends, the five-limb core transformer “T5” also has two regulation windings. In the observed nominal position of the tap changer, only the inner regulation winding (GST) is current-carrying. Because the outer regulation winding (FST) is currentless, the winding can be modelled out of one block.

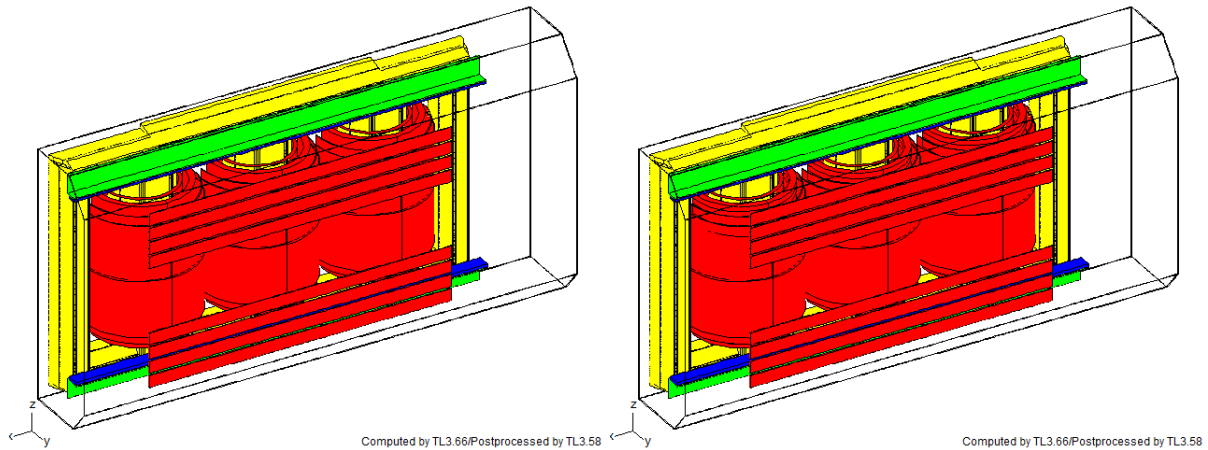


Fig. 81. “T5”: Geometry plots, left: one axial winding block on HV-side; right: several axial winding blocks on HV-side

A comparison of the current densities of the HV-winding shows, similar to the three-limb core transformer “T3”, large differences in the current densities of the upper and lower winding blocks compared to the mean current density in the left model in Fig. 81.

Table 32: “T5”: Current densities in winding segments

Winding parts	HV-winding with one axial block J_{peak} in A/m ²	HV-winding with several axial blocks J_{peak} in A/m ²
Winding part 1	$0.245 \cdot 10^7$	$0.197 \cdot 10^7$
Winding part 2		$0.237 \cdot 10^7$
Winding part 3		$0.249 \cdot 10^7$
Winding part 4		$0.253 \cdot 10^7$
Winding part 5		$0.266 \cdot 10^7$

5.5.1 Field plots

Also all field plots, especially those of the tank and the tank shielding, manifest increases in the maximum values of the scales and also in the field profile. The plots of tank, clamping structure, tank shielding and yoke shielding can be seen in Figs. 82 to 85.

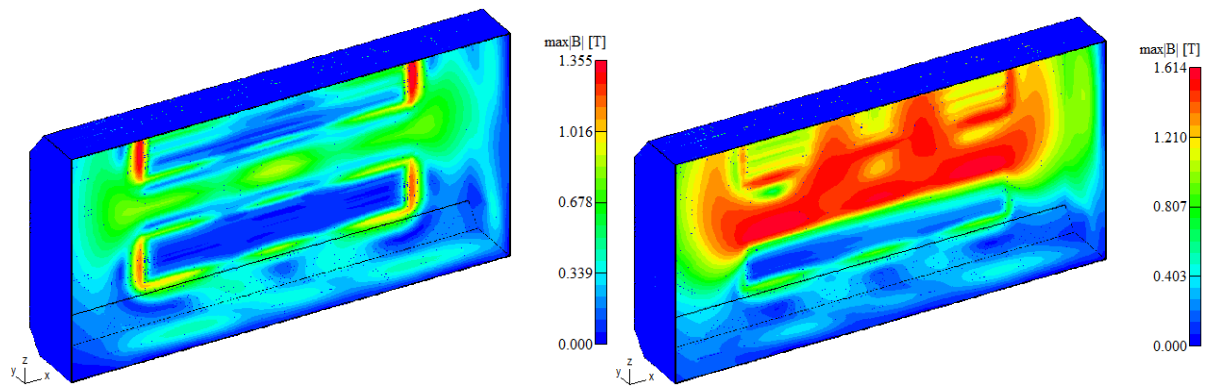


Fig. 82. “T5”: Max. surface flux density in tank, left: one axial winding block on HV-side; right: several axial winding blocks on HV-side

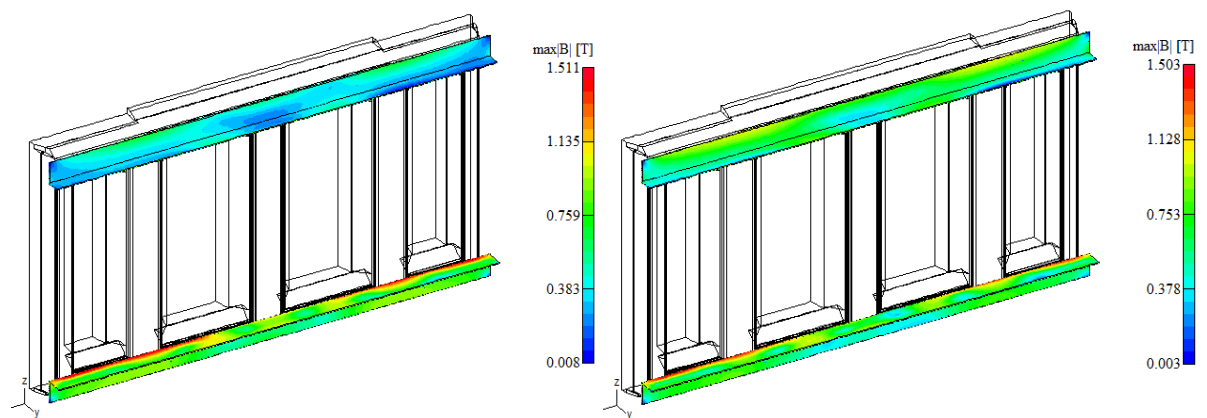


Fig. 83. “T5”: Max. surface flux density in clamping structure, left: one axial winding block on HV-side; right: several axial winding blocks on HV-side

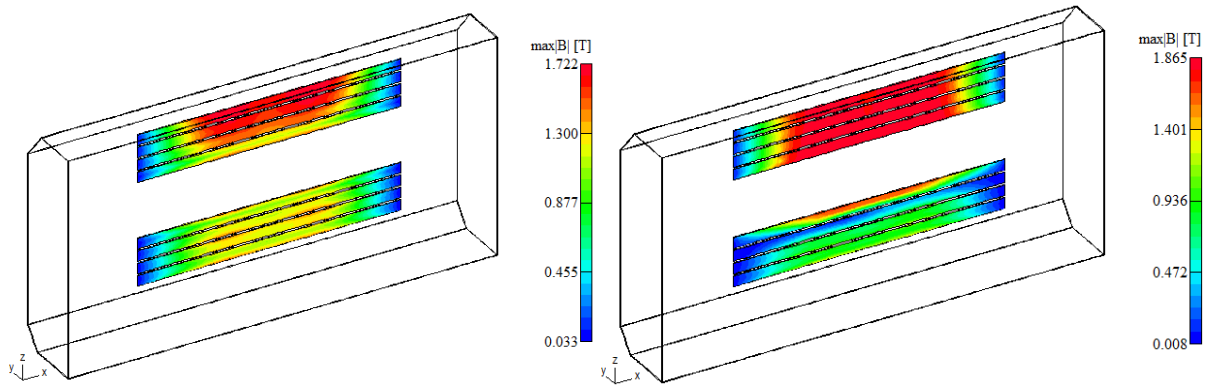


Fig. 84. “T5”: Max. surface flux density in tank shielding, left: one axial winding block on HV-side; right: several axial winding blocks on HV-side

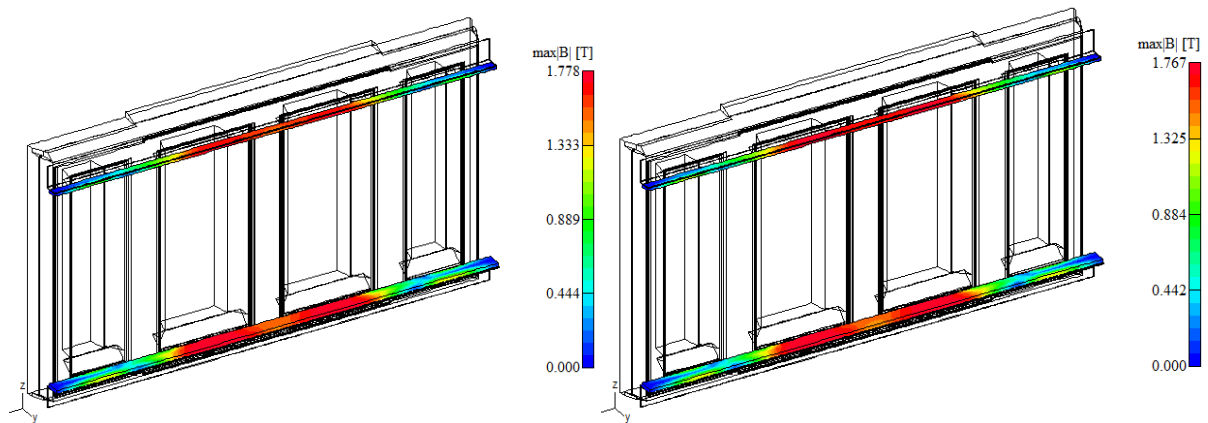


Fig. 85. “T5”: Max. surface flux density in yoke shielding, left: one axial winding block on HV-side; right: several axial winding blocks on HV-side

5.5.2 Loss comparison

Comparing the losses in Table 33 and Table 34, results in large differences in tank losses while the losses in the tank shielding are only slightly larger in the second model. This is because the horizontal tank shielding of this transformer is designed to handle the magnetic field generated by vertical wires and the observed stray field is generated by horizontal winding conductors. In order to reduce these losses, a vertical tank shielding can be recommended to be installed on the tank walls too.

Table 33: "T5", one axial winding block on HV-side, losses in non-active steel parts

Component Name	Eddy current	Specific	Hysteresis	Total
	Losses	Losses	Losses	Losses
	W	W	W	W
Tank 1/2	568	0	372	940
Tank Wall behind	463	0	289	752
Tank Cover (1/2)	59	0	41	99
Tank Bottom (1/2)	26	0	22	49
Tank Wall right (1/2)	18	0	16	34
Tank Wall left (1/2)	3	0	4	6
Core (1/2)	1204	5915	0	5915
Clampings	428	0	231	659
Vertical Plate, bottom	184	0	92	275
Horizontal Plate, bottom	171	0	89	260
Vertical Plate, top	37	0	27	64
Horizontal Plate, top	36	0	23	59
Tank Shielding, total	0	590	0	590
Tank Shielding horizontal, top	0	361	0	361
Tank Shielding horizontal, bottom	0	230	0	230
Yoke Shieldings, behind	0	687	0	687
Yoke Shielding, bottom	0	479	0	479
Yoke Shielding, top	0	208	0	208
Total Losses	2201	5988	602	8790

Table 34: "T5", several axial winding blocks on HV-side, losses in non-active steel parts

Component Name	Eddy current	Specific	Hysteresis	Total
	Losses	Losses	Losses	Losses
	W	W	W	W
Tank 1/2	5993	0	2033	8026
Tank Wall behind	5573	0	1788	7361
Tank Cover (1/2)	266	0	141	407
Tank Wall right (1/2)	123	0	75	198
Tank Bottom (1/2)	21	0	19	40
Tank Wall left (1/2)	10	0	10	20
Core (1/2)	1667	7492	0	7492
Clampings	463	0	260	723
Vertical Plate, top	128	0	73	202
Vertical Plate, bottom	119	0	66	185
Horizontal Plate, bottom	108	0	63	171
Horizontal Plate, top	108	0	57	165
Tank Shielding, total	0	880	0	880
Tank Shielding horizontal, top	0	725	0	725
Tank Shielding horizontal, bottom	0	154	0	154
Yoke Shieldings, behind	0	697	0	697
Yoke Shielding, bottom	0	460	0	460
Yoke Shielding, top	0	237	0	237
Total Losses	8122	7402	2293	17818

6 Results

6.1 Additional losses in windings

Comparing the results from the calculations of the additional winding losses of the already existing 2D models to the 3D FEM-models shows differences in the radial additional losses, whereas the axial additional losses are nearly the same. As explained in subsection 2.1.1, the change of transformer geometry in azimuthal direction in the 2D model is taken into account with an internal formula for the distance to the top of the transformer. This leads to larger radial additional losses in the inner winding and smaller radial additional losses in the outer winding(s) than in the more realistic 3D model. Additionally, for the three-limb core transformer “T3”, the radial additional losses in the middle winding are larger than the ones in the outer windings. Compared to the other three-phase transformer “T5”, where the radial additional losses are nearly the same on every limb, it seems that the difference between the limbs is due to the absence of back-closing limbs and because of the small distance to the tank shielding. The effects of the other two windings on the observed winding are also not taken into account in the 2D model.

Compared to the I^2R -losses, the radial additional losses are very small. So it is possible, that a small change in temperature during the measurement process results in larger absolute differences in I^2R -losses than the value of the radial losses. Because of this and due to the fact that the so called t-losses, which appear in interleaved and partly interleaved disk windings, are not considered in the 3D TrafoLoss-model, it is not necessary to calculate the additional winding losses with a 3D model at this juncture. Also the computation times of the 3D models, especially when taking eddy currents into account, are much higher than the negligible computation times of 2D transformer models.

However, a possible future application of the 3D model with modelled windings could be the calculation of the forces occurring in the transformer windings. Due to the differences in the field in azimuthal direction compared to the computed fields in the 2D model (described in section 3.3), it can be assumed that the forces may be different.

6.2 Additional losses in non-active steel parts

Summarizing the results to the investigations on how detailed disk windings have to be modelled in the 3D TrafoLoss-model for computing the eddy current and specific losses in non active steel parts leads to the conclusion that it is necessary to implement windings as detailed as possible. Reviewing the loss calculations in chapter 0 shows differences in calculated losses for each of the five benchmark transformers. One-phase transformers like the one-limb core transformer “T1”, the two-limb core transformer “T2” and the four-limb core transformer “T4” are realized with a voltage input in the HV-disk winding in the winding centre. Comparing the models with one axial winding block on HV-side with a mean current density and with several axial winding blocks shows that there are larger differences in current densities in the winding centre, whereas the differences at the winding ends are relatively small. This setup leads, compared to the model with a mean current density, to differences in losses in non-active steel parts, mainly in tank and in the tank shielding.

Compared to the differences for one-phase transformers, the three-phase transformers “T3” and “T5” are showing much larger differences in the calculated losses. The differences in the current densities are thereby located at the winding ends, because of this transformers are manufactured with voltage input on HV-side at the upper and lower winding ends (delta-connection). This leads to large differences in calculated losses in non-active steel parts. These differences are, similar to the one-phase transformers, mainly located in the tank. In order to reduce these losses, a better tank shielding (“T3”) has to be installed. Because of the five-limb core transformer “T5” has only a horizontal tank shielding for reducing the impacts of the LV-leads, the tank losses are more than eight times larger compared to those of the model with one axial winding block on HV-side.

Bibliography

- [1] D. Giselbrecht, *Dielektrische Modellierung von Öl-Papier-Isolationssystemem im Frequenzbereich zur Diagnose von Leistungstransformatoren*, 1st ed. Göttingen, Deutschland: Cuviller Verlag Göttingen, 2008.
- [2] R. Fischer, *Elektrische Maschinen*, 10th ed. München, Wien, Deutschland: Carl Hanser Verlag, 1999.
- [3] O. Biro [et al.], "Numerical Modeling of Transformer Losses," in *International Colloquium Transformer Research and Asset Management*, Cavtat, November 12 - 14, 2009.
- [4] M. J. Heathcote, *The J&P Transformer Book*, Twelfth ed. London: Reed Educational and Professional Publishing Ltd 1998, 1998.
- [5] R. KÜchler, *Die Transformatoren*, 2nd ed. Berlin: Springer- Verlag Berlin Heidelberg, 1966.
- [6] O. Biro, *Simulation of time-dependent fields*. 2017, Lecture notes of lecture 437.247.
- [7] G. Paoli, O. Biro, and G. Buchgraber, "Complex representation in nonlinear time harmonic eddy current problems," *IEEE Transactions on Magnetics*, vol. 34, pp. 2625-2528, Sep. 1998.
- [8] O. Biro [et al.], "Overview of Finite Element Techniques in the Design of Power Transformers," in *The Sixteenth Biennial IEEE Conference on Electromagnetic Field Computation*, Annecy, May 25 - 28, 2014.
- [9] O. Biro, G. Koczka, B. Wagner, U. Baumgartner, and G. Leber, "Finite Element Method for Nonlinear Eddy Current Problems in Power Transformers," in *International Colloquium Transformer Research and Asset Management*, Dubrovnik, May 16 - 18, 2012.
- [10] G. Buchgraber, O. Biro, P. Kalcher, and K. Preis, "Computation of Temperature Rise in Transformer Bushing Adapters," in *IEE-PES Transmission and Distribution Conference and Exposition*, Dallas, September 7 - 12, 2003.